Università degli Studi di Roma *"La Sapienza"*

Dipartimento di Meccanica e Aeronautica

Dottorato in Meccanica Teorica e Applicata, XX ciclo

Ph.D. Thesis

Modeling of Cooling Channel Flow in Liquid-Propellant Rocket Engines

Marco Pizzarelli

Supervisor: Prof. M. Onofri

2006/2007

Contents

Abstract **1**

1 Introduction **3**
1.1 Cooling techniques for rocket engines 3
1.2 Regenerative cooling 7
1.3 Coolant flow: critical aspects 10
1.4 Thermal analysis 11

2 Real fluid thermodynamics **13**
2.1 pvT behaviour 13
2.2 Equation Of State 17
2.2.1 Perfect gas EOS 17
2.2.2 Van Der Waals EOS 18
2.2.3 Benedict Webb Rubin EOS 20
2.3 Transport properties 21
2.4 Thermodynamic relations 22
2.5 Methane 24
2.5.1 Methane as a fuel for space propulsion 24
2.5.2 Methane diagrams 26

3 1D model **35**
3.1 Physical and mathematical modeling 36
3.2 Hot-gas expansion 36
3.3 Coolant flow 40
3.4 Coolant semi-empirical relations 41
3.4.1 Skin friction and heat transfer at constant properties 42
3.4.2 Non circular cross section 43
3.4.3 Roughness 44
3.4.4 Variable properties 46
3.5 Heat conduction through the wall 48
3.6 High Aspect Ratio Cooling Channels: 1D model 50

4 "Quasi 2D" stratification model **57**
4.1 Heat conduction through the wall . . . 58
4.2 Coolant flow . . . 59
4.3 Computational strategy . . . 62
4.4 Validation and results: hydrogen test case . . . 63
4.5 Results: methane test case . . . 67

5 Numerical method **71**
5.1 Governing equations . . . 71
5.2 Vectorial form of the conservation laws . . . 74
5.3 Finite volume numerical scheme . . . 76
5.3.1 1D Euler equation . . . 76
5.3.2 3D case . . . 81
5.3.3 Control of time accuracy . . . 81
5.3.4 Viscous fluxes . . . 83
5.4 Riemann problem . . . 83
5.4.1 1D Euler equation with a generic EOS . . . 84
5.4.2 Riemann problem for a generic EOS . . . 87
5.4.3 Approximate riemann solver for a generic EOS . . . 90
5.5 Boundary conditions . . . 94
5.5.1 Supersonic outflow . . . 95
5.5.2 Supersonic inflow . . . 95
5.5.3 Subsonic outflow . . . 97
5.5.4 Subsonic inflow . . . 98
5.6 Generic EOS . . . 99
5.7 Turbulence modeling . . . 102
5.7.1 Spalart-Allmaras model . . . 104

6 Validation **107**
6.1 Turbulent flat plate: perfect gas . . . 108
6.2 Effect of the EOS discretization . . . 113
6.3 Turbulent flat plate: supercritical fluid . . . 115
6.4 2D channel test case . . . 117

7 3D results **121**
7.1 Test cases description . . . 121
7.2 Flow description . . . 124
7.3 Parametric analysis: aspect ratio effect . . . 134
7.4 Parametric analysis: inlet temperature effect . . . 140
7.5 Parametric analysis: inlet pressure effect . . . 147

Conclusions **153**

A Thermodynamic relations **157**
A.1 Constant volume specific heat 157
A.2 Constant pressure specific heat 159
A.3 Entropy 160
A.4 Internal energy and enthalpy 163
A.5 Speed of sound 164
A.6 Isothermal compressibility 166

B Hydrogen thermodynamic properties **167**
B.1 Para-hydrogen equation of state 169
B.2 Para-hydrogen transport properties 172

C Methane thermodynamic properties **175**
C.1 Methane equation of state 175
C.2 Methane transport properties 178

Abstract

Ever since the development of liquid rocket engine, there has been a need to predict the peak heat flux that affects the engine material and thus to control the wall thermal behaviour of rocket engine. To prevent thermal failure, the engine is generally cooled by means of a coolant that flows in passages that line the hottest part of the engine (i.e., combustion chamber and nozzle wall). This is the fluid-cooling system. If the coolant is one of the propellants, once it passes through the cooling circuit, it can be injected into the combustion chamber or it can be dumped overboard. The former case is referred to as *Regenerative cooling* system while the latter as *dump cooling* system. In case of high performance cryogenic rocket engine (such as LO_2/hydrogen and LO_2/methane engines) the coolant working pressure is supercritical and thus it behaves far from a liquid or a perfect gas. The fluid-cooling system (often referred to regenerative cooling because of the limited application of the dump cooling) of cryogenic rocket engines, is the technological background of this Ph.D. thesis.

It is common and well confirmed practice in industry to analyze wall thermal behaviour of liquid rocket engine by means of simple and fast tools based on semi-empirical relationships. These relationships are generally calibrated by means of data collected in experimental tests of subscale engines. Industrial tools provide reasonable results but they are not able to accurately describe many phenomena that occur in the hot-wall/coolant environment, such as three-dimensional effects, asymmetric heat flux distribution in the material and supercritical behaviour of the coolant. For that reason, to circumvent the uncertainties of the design tools, regenerative systems are often over dimensioned. Moreover, these tools are deeply related to the engine for which they have been calibrated and thus they cannot be easily extended for a new generation of engines.

In last years new approaches have risen; in fact new geometry configuration (i.e., high aspect ratio cooling channels) and new coolants (such as methane) to be used in the next future, have imposed more accurate analysis tools, such as three-dimensional Navier Stokes solver to describe coolant flow and three-dimensional Fourier analysis to describe wall thermal transmission. Simplified approaches are always used since, due to the limited computer power, three-dimensional tools

are not suitable as design tools. However, accurate three-dimensional analysis can be integrated with simple and fast design tool in order to better describe and comprehend the phenomena that occur in the hot-wall/coolant environment.

The aim of this study is to present and provide suitable theoretical and numerical tools able to describe the thermal behaviour that occur in regenerative cooling system, with special regard to the subcritical/supercritical coolant flow inside cooling channels. This aim has been achieved in three steps:

- A suitable mathematical description of thermophysical properties of coolants has been adopted. According to this mathematical modeling, computer subroutines describing the thermophysics of typical coolants (such as hydrogen and methane) have been implemented (see Chap. 2)

- A suitable physical and mathematical model able to describe both the wall thermal behaviour and the coolant flow that occur in regeneratively cooled rocket engines has been developed and implemented in a numerical code. The model is an extension of the typical 1D-model (see Chap. 3) in the sense that it is able to describe the coolant and fin thermal stratification that occurs in high aspect ratio cooling channels (see Chap. 4). For that reason this model will be referred to as a "quasi 2D" model. The coolant thermophysical properties have been provided by means of the above mentioned hydrogen-methane subroutines. The code has been successfully validated with respect to the literature data.

- At last, a Navier Stokes solver able to describe the high Reynolds number turbulent flow of generic fluid in three-dimensional cooling channels has been developed (see Chap. 5). This numerical tool has been successfully validated by comparison with exact solutions and literature data (see Chap. 6). Furthermore three-dimensional flow fields for a cryogenic fluid (methane) have been computed to analyze the coolant behaviour inside straight channels with rectangular cross section and to discuss the channel aspect ratio effect on the cooling performances (see Chap. 7).

Chapter 1

Introduction

In this introductive chapter the problem of thrust-chamber cooling for space-engine is discussed. Once the different techniques currently employed in this aim are shown (see Sec. 1.1), the attention is focused on the regenerative cooling system (see Sec. 1.2). Then the critical aspects that characterize coolant flow inside cooling channels are discussed (see Sec. 1.3). For that reason thermal analysis of regenerative system is a challenging task and, up to now, a research field little deepened (see Sec. 1.4).

1.1 Cooling techniques for rocket engines

The adequacy of a rocket motor depends almost entirely upon its ability to perform without damage at high temperatures for the operating duration to which it is subjected.

Because of high combustion temperatures ($2500\ K$ to $3600\ K$) and high heat-transfer rates from the hot-gas to the chamber wall (1 MW/m^2 to over 160 MW/m^2), a "cooling system" must be employed [21]. The primary objective of a "cooling system" is to prevent the chamber and nozzle walls from reaching such temperature that they will no longer be able to withstand the imposed loads or stresses, thus causing the chamber or nozzle to fail. Most wall materials lose strength and become weaker as temperature is increased. With further heating, the walls would ultimately fail or even melt. Cooling thus reduces the wall temperatures to an acceptable value [47]. The meaning of "cooling system" is generalized to include any scheme designed to limit the wall temperature, even if no fluid coolant is employed [26].

Cooling also helps to reduce the oxidation of the wall material and the rate at which walls would be eaten away. The rates of oxidizing chemical reactions between the hot-gas and the wall material can increase dramatically with wall

temperature. This oxidation problem can be minimized not only by limiting the wall temperature, but also by burning the liquid propellants at a mixture ratio where the percentage of aggressive gases in the hot-gas (such as oxygen) is very small, and by coating certain wall materials with an oxidation-resistant coating [47].

The cooling of rocket engines can be accomplished in a variety of ways. In the following, the main cooling techniques are presented.

Heat sink cooling

The most direct way to limit the internal surface temperature is to provide a sufficiently thick chamber or nozzle wall with the necessary heat capacity to soak up the heat transferred during the prescribed firing duration. The thrust chamber does not reach a thermal equilibrium, and temperatures continue to increase with operating duration. The heat absorbing capacity of the hardware determines its maximum duration. The rocket combustion operation has to be stopped just before any of the exposed walls reaches a critical temperature at which it could fail. The most suitable materials for this type of cooling are those for which the product *specific heat* x *thermal conductivity* x *density* has high values. The best material from this standpoint is copper [57]. The foregoing criterion is not, however, a unique guide to motor construction, since considerations of strength and weight are frequently of greater importance. In any case, as the required operating duration for an uncooled motor is raised, the requisite motor weight becomes excessive for practical use. Consequently, even if heat-sink system has the advantages of simplicity and cheapness of manufacture, for durations greater than 10 to 20 seconds, it results in a weight penalty [26]. This method has mostly been used with low chamber pressures and low heat transfer rates since this type of motors weights more than rocket motors of equal thrust output that employ regenerative cooling.

Regenerative cooling and dump cooling

Regenerative cooling, the most widely applied method, utilizes one or possibly both of the propellants fed through passages in the thrust-chamber wall for cooling, before being injected into the combustion chamber. This cooling system enables lightweight, thin metal, combustion chambers and nozzles. A variation of this method is the “dump cooling”: a small percentage of the propellant, such as the hydrogen in a LO_2/LH_2 engine, is fed through passages in the thrust chamber wall for cooling and is subsequently dumped overboard through openings at the rear end of the nozzle skirt. Because of inherent problems, such as performance losses, this method has only limited application [21].

Film cooling and transpiration cooling

Film cooling and transpiration cooling are supplementary techniques that are used occasionally with regenerative cooling method to locally augment its cooling capability. With film cooling method wall surfaces are protected from excessive heat by a thin film of coolant or propellant introduced through orifices around the injector periphery or through manifolded orifices in the chamber wall near the injector and sometimes in several more planes toward the throat [47]. Transpiration cooling method is essentially a special type of film cooling: a coolant (either gaseous or liquid propellant) is introduced through porous chamber walls at a rate sufficient to maintain the desired temperature of the combustion-gas-side chamber wall [47].

Ablative cooling

In this process, combustion-gas-side wall material is sacrificed by melting, vaporization, and chemical changes to dissipate heat. As a result, relatively cool gases flow over the wall surface, thus lowering the boundary-layer temperature and assisting the cooling process. In addition, the ablative material is usually a good thermal insulator, keeping to a minimum the heat transmitted to the outer structure. Ablative cooling has been used in numerous designs, initially mainly for solid-propellant system, but later, equally successfully, for short-duration and/or low-p_c liquid systems [21].

Radiation cooling

With this method, heat is radiated away from the surface of the outer thrust-chamber wall. It has been successfully applied to very small, high-temperature-material combustion chambers and to low-heat-flux regions, such as nozzle extensions (i.e., diverging nozzle exhaust sections beyond an area ratio of about 6 to 10) [21].

Selection of the best cooling method for a given thrust chamber depends on many considerations. There are no simple and fast rules. However, the main factors that influence the selected design approaches will be the following [21]:

Propellants

The properties of the combustion products, such as temperature, specific heat, weight, viscosity, etc., have a direct influence on the heat-transfer rate and thus affect chamber cooling requirements and methods. The properties and flowrates of the propellants determine whether they are suitable for regenerative, transpiration,

dump, or film cooling. Consequently, the propellants involved will be a primary consideration in the design of a chamber cooling system.

Chamber pressure

The effect of chamber pressure on the heat flux in a nozzle is in general an increase in the heat flux with increasing pressure due to a progressive increase in higher heat-transfer rates with increasing combustion-gas density (i.e., higher combustion-gas mass flowrates per unit area of chamber cross section). Regenerative- and film-cooling methods are usually combined to meet the stringent requirements of high-chamber-pressure applications.

Propellant feed system

The type of propellant feed system used in an engine determines its pressure budget. In a turbopump-fed engine, a large pressure drop is usually available for chamber cooling. The availability of this pressure drop permits the use of regenerative cooling, which requires sufficient pressure to force the coolant through the cooling passages before entering the injector. A pressure-fed engine usually has more stringent pressure limitations and operates at relatively lower chamber pressures. This suggests the application of film, ablative, radiation cooling or combinations of these techniques.

Thrust-chamber construction material

The properties of the thrust-chamber materials will profoundly affect the cooling-system design. Strength at elevated temperature and thermal conductivity will determine the suitability of a given material for regenerative cooling. For film-cooled chambers, higher allowable material working-temperatures are desired, for lower film-coolant flowrates. The application of radiation cooling to a chamber largely depends on the availability of high-temperature ($2000\ K$ and up) materials. The success of ablative cooling entirely depends on the availability of suitable materials.

In practice, the design of the thrust-chamber cooling system is a major link in the complete engine design. It cannot be treated independently, without consideration of other engine system aspects. For instance, optimization of the chamber pressure of a high-performance engine may be largely limited by the capacity and efficiency of the chamber-cooling system. In turn, chamber pressure affects other design parameters, such as the nozzle expansion ratio, propellant feed pressure, and weight. Because of the complex interrelations between these factors,

the complete analysis of chamber-cooling systems is a specialized field, requiring thorough knowledge of heat transfer, fluid mechanics, thermodynamics, materials, and structures.

1.2 Regenerative cooling

To cool the walls of a regenerative rocket engine, the fuel (e.g., hydrogen, kerosene, methane) or the oxidizer (e.g., oxygen) is passed through cooling channels that are machined in the wall. Finally the heated coolant is injected into the thrust chamber (see Fig. 1.1) or goes to turbine. This cooling technique is used primarily with bi-propellant chambers pressure and high heat transfer rates [47].

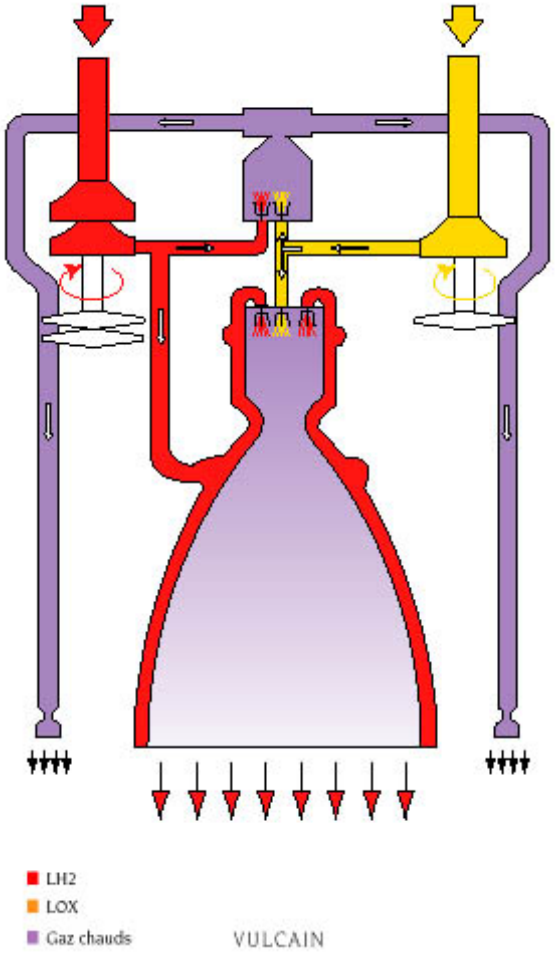

Figure 1.1: Vulcain flow schematic (from [1]).

The term regenerative cooling is intended to convey the fact that the heat absorbed by the coolant propellant is not wasted but augments the initial temperature and the energy level of the propellant prior to injection; this increase in the internal energy of the liquid propellant can be calculated as a correction to the enthalpy of the propellant. However, the overall effect on rocket performance is usually very slight. With some propellants the specific impulse can be 1% larger if the propellants are preheated through a temperature differential of 100 to $200\ K$ [47]. This method is called regenerative cooling because of the similarity to steam regenerators. A large number of successful motors of this type have been built.

Regenerative cooling, appears currently to be an efficient approach to the solution of the heat problem. It has the advantage that, once the cooling system has been developed correctly, the engine can be operated for long durations (several minutes at a time) without damage [57]. Furthermore, these motors can be made extremely light in weight, the thrust-weight ratio markedly increasing with the larger thrusts. However, it has to be kept in mind that regenerative system permits only limited throttling with most coolants, has reduced reliability with some coolants (e.g., hydrazine) and requires increased pump power because of the large pressure drop at high heat-flux levels. The trade-off among these aspects makes regenerative cooling interesting for large high-pressure, high heat-flux thrust chambers and for expander (and expander-bleed) cycle engines [47].

A typical value of the integrated heat flux over the entire surface is about 2% of the heat of combustion for a small engine (thrust $< 5000\ N$). This percentage is considerably smaller for larger thrust motors, because the combustor volume increases approximately in proportion to the mass flow, while the surface of combustor increases only as the two-thirds power for similar shapes. The practicability of running a rocket engine continuously with only regenerative cooling, using either one or both propellants, is directly the results of this low percentage of heat transfer. None of the common propellants can absorb more than few per cent of the heat of combustion without vaporizing or decomposing and thus becoming unsuitable as coolants [26].

Chemical changes in the liquid coolant can seriously influence the heat transfer from hot walls to coolant. Cracking of the coolant, with an attendant formation of insoluble gas, tends to reduce the maximum heat flux and thus promotes failure more readily. Hydrocarbon fuel coolants (methane, kerosene) can break down and form solid, sticky carbon deposits inside the cooling channel, impeding the heat transfer. Some propellants, such as hydrazine, can decompose spontaneously and explode in the cooling passages if they become too hot [47].

The choice of the material for the inner wall in the chamber and the throat region, which are the critical locations, is influenced by the hot-gas resulting from the propellant combination, the maximum wall temperature, the heat transfer, and the feed system. For high-performance and high heat transfer, regeneratively

cooled thrust chambers, a material with high thermal conductivity and a thin wall design will reduce the thermal stresses. Copper is an excellent conductor and it will not really oxidize in fuel-rich non corrosive gas mixture, such as are produced by oxygen and hydrogen below a mixture ratio of 6.0. The inner walls are therefore usually made of a copper alloy (with small additions of zirconium, silver, or silicon), which has a conductivity not quite as good as pure (oxygen-free) copper but has improved high temperature strength [47].

The wall temperature on the hot side of the cooling channels in a regeneratively cooled combustion chamber can be reduced increasing the coolant side surface area relative to the hot-gas side surface by the use of extended surfaces or "fins" (see Fig. 1.2). An increase in the number of passages, and therefore the surface area of the passages that circumferentially line the outer wall of a combustion chamber, necessarily increases their aspect ratio. In turn the material between them, known as rib, functionally becomes a fin. High aspect ratio cooling channels (HARCC) have shown a great potential of influencing positively both the temperature field and the pressure loss [10, 53]. Round tubes do not possess this interesting and convenient geometry.

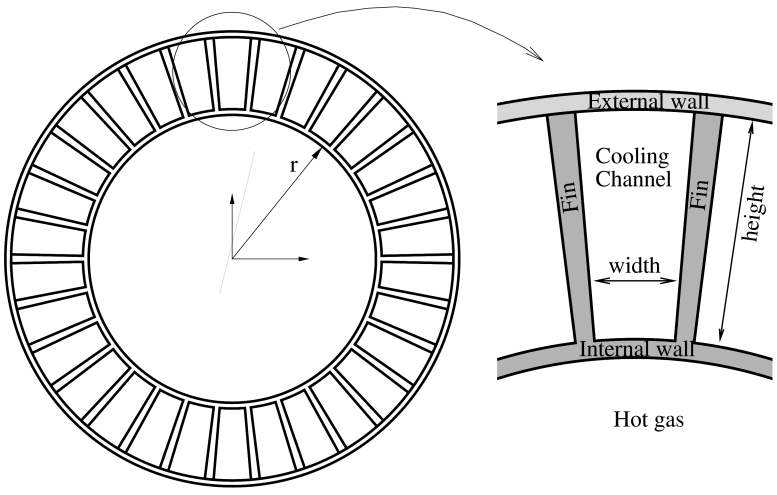

Figure 1.2: Schematic of cooling channels geometry.

1.3 Coolant flow: critical aspects

In this thesis we focus on the channel flow of cryogenic coolant, because it is the most challenging and (up to now) the less comprehended phenomenon that occurs in the regenerative cooling systems. Its main critical aspects are [54]:

- In cryogenic engines, the coolant is generally the liquid fuel, and the elevated pressures required in the combustion chamber are sufficient to ensure that the fluid remains pressure supercritical over the entire length of the cooling passage: this means that all fluid properties are strong functions of both the pressure and the temperature.

- If the fluid enters the cooling channel with a subcritical temperature (such as for methane) it must kept in mind that as it passes throughout critical temperature, the fluid parameters show large variations and exhibit maximum values. For instance specific heat and isothermal compressibility appears to approach infinity at critical point.

- For the temperature and pressure range of interest, the density of the cryogenic coolant varies by an order of magnitude, as it moves from a predominantly "liquid-like" regime (at the manifold inlet) to a predominantly "gas-like" regime (at the chamber injectors or turbine). Thus the coolant behaves neither as a liquid (i.e., incompressible fluid) nor as a perfect gas (high compressible fluid). This variable flow regime implies strong compressibility effects that have a dramatic effect on the fluid-dynamic flowfield, and hence, on the heat transfer.

- Due to the pressure condition of the coolant, its Reynolds number can be as high as $10^6 - 10^7$ [14]. This implies that the coolant flow is highly turbulent and thus it must be described by proper turbulence modeling.

- The geometry of the cooling passages is strongly three-dimensional, especially in the case of high aspect ratio cooling channel [49, 53, 28]. As a consequence the coolant flow shows many three-dimensional features, such as inefficient heat transfer at the channel corner.

- The passages are not heated uniformly around their periphery, but they are heated from one side only. This implies a strong thermal stratification in the coolant flow, along the radial direction.

- The highly conductive wall material of the combustor body provides a strong fin effect between adjacent coolant passages that makes them more effective. This effect in enhanced as the aspect ratio increases.

- The curvature introduced into the coolant passages by the converging-diverging shape of the thrust chamber generates vortices that enhance the heat transfer inside the passages. In fact, in the presence of temperature stratification, these vortices transport cool fluid from one side to the other side of the channel cross section, thereby increasing the heat transfer.

1.4 Thermal analysis

An essential part of the design and realization of liquid rocket engines is the thermal analysis, which is necessary to predict the peak heat flux from the combustion gases to the engine wall and to ensure the structural integrity of the combustion chamber. The need for thermal analysis is especially important in reusable engines, where an effective and efficient cooling system is crucial to extend the engine life, or in expander-cycle engines, where coolant warming provides the available power for turbo-machinery. In these cases, usually regenerative cooling is considered. Moreover, the analysis of the cooling channel flow is essential to predict not only the efficiency of the coolant, but also the coolant temperature and pressure at the channel exit. Those parameters are of great importance for the design of the injectors and of the coolant pump.

At the present time, a comprehensive thermal model aiming to estimate rocket wall temperature and heat-flux and coolant flow behaviour is rather complex, because it must account for different phenomena coupled with each other: convection from hot-gas to the wall, conduction within the wall, and convection from the wall to the cold fluid. The coupling of these processes is strongly non-linear because coolant and hot-gas heat transfer depend on the fluid pressure and temperature and on wall temperature. Further complications arise from the necessity of properly describing the coolant channel-flow (see Sec. 1.3).

Moreover, it has to be considered that the design of a regenerative system is based on optimization process that consists of many calculation loops which include the thermal and fluid mechanics analysis of the coolant flow in the cooling channels as well as the thermal analysis of the wall structure [44]. In case of optimization, approaches based on one-dimensional models heavily relying on empirical relationships are therefore the most suitable [14]. In fact, with these methods the complexity of the cooling system can be faced and the main parameters that affect the problem can be reasonably well described.

One of the main drawbacks of conventional one-dimensional calculation methods is that an ideal mixing of the thermal energy into the coolant channel cross section is assumed. This implies that when a significant radial thermal stratification takes place, like in the case of HARCC, a significant error arises [49]. To circumvent these limitations a “quasi 2D” modification of a typical one-dimensional

approach can be considered [53, 36]. This approach consists in a computational tool able to describe the coupled hot-gas/wall/coolant environment that occurs in most liquid rocket engines and to provide a quick and reliable prediction of thermal stratification phenomena in cooling channels. However it is still an approach widely relying on empirical relationships even if it allows to compute the radial stratification of both the wall and the coolant flow temperatures.

If a more detailed fluid dynamic and thermal analysis of the coolant flow is necessary, it has to be considered that the temperature stratification of the cooling channels is a major three-dimensional effect that occurs in this environment and it strongly influences the heat transfer efficiency of the coolant [49]. Another important three-dimensional effect that characterizes the HARCC channel flow is the presence of vortices in the channel cross section that influence the heat transfer (see Sec. 1.3). To describe and understand these three-dimensional peculiarities, since the early nineties, many researchers have studied three-dimensional flow of cryogenic fluids in cooling channels, using appropriate Navier Stokes solvers [55, 54, 28]. To simplify the problem and to avoid time-consuming computations, low-Re duct flows without the coupling between the coolant flow and the wall thermal conduction have been analyzed first. These studies have qualitatively shown the importance of such three-dimensional phenomena in cooling passages. More recently a new interest on thermal and coolant flow analysis has risen. This is due to the increased computer memory and power and to the practical interest in the design of high-performance combustion chambers, with particular regard to the cryogenic expander-cycle engines [25, 22, 34]. This interest has also led to the development of coupled three-dimensional coolant/wall analysis [50, 25]; however, in spite of the massive computer power used, the considered coolant flow conditions are still far from the actual industrial conditions (Re up to 10^7 and strong wall temperature gradient).

Chapter 2

Real fluid thermodynamics

In the cryogenic rocket engines (such as LO_2/hydrogen or LO_2/methane), the liquid coolant (hydrogen or methane) flowing in the cooling channels of the regenerative system always has to pass through the near-critical region. In the near-critical region, large changes in the fluid properties (such as specific heat and thermal conductivity) greatly influence the heat transfer characteristic. In most systems, particularly those fed from a turbopump, the coolant pressure is supercritical so that the fluid behaviour cannot be well described neither under the perfect gas hypothesis (that is, $p = \rho RT$) nor under the perfect liquid hypothesis (that is, $\rho = const$). Hence, specific equations for the equation of state and the transport properties must be introduced to better describe the real fluid thermodynamics.

In this chapter the thermophysical description of pure substances is presented, with special regard to the subcritical and supercritical state (Sec. 2.1). Then some equations of state to describe the pressure-volume-temperature behaviour and the thermodynamic properties of pure substances are discussed (Sec. 2.2). Finally proper equation of state to describe the hydrogen and methane subcritical/supercritical regime is chosen and some thermophysical properties diagrams for methane, one of the most promising propellants for future applications, are shown (Sec. 2.5). In particular, hydrogen has been used as working fluid in the "quasi 2D" computations presented in Chap. 4 and methane has been used as working fluid in the "3D" computations presented in Chap. 5.

2.1 pvT behaviour

A fluid is a system that can be identified by two independent thermodynamic variables. Some examples are: perfect gas, liquid, vapour, etc. A pure substance (such as H_2 and CH_4) is a fluid since the three variables pressure-volume-temperature (pvT) are related by an equation called equation of state in the general form:

$$f\left(p, v, T\right) = 0$$

This equation describes the behaviour of the pure substance at the thermodynamic equilibrium and reduces the three variables pvT into two independent variables.

Considering pressure and temperature as independent variables, a typical diagram that describes the behaviour of a pure substance is shown in Fig. 2.1.

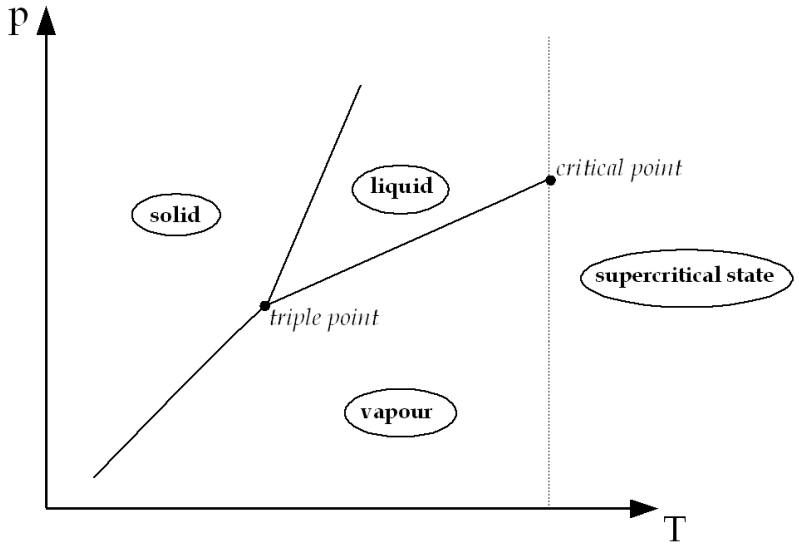

Figure 2.1: pT diagram of a pure substance.

In this diagram the solid, liquid and vapour states are clearly shown and the lines that bound these states represent the two-phase regions. Since the change of state is an isobaric/isotherm process with variable density and phase composition, in the pT-diagram the two-phase transition is simply represented by a line.

The triple point represents the thermodynamic state in which the three phases (solid, liquid and vapour) coexist. Below this point it is possible to transform a solid into a vapour (or vice versa) only by a temperature change. It is the case of carbon-dioxide (CO_2) which, having a triple-point temperature of $216.55\ K$ and a triple-point pressure of $5.17\ bar$, at room pressure ($\simeq 1\ bar$) carbon-dioxide it can be directly converted into a solid (i.e., condensation) by heat subtraction.

Regarding the solid-liquid transition, this phase boundary in the pT phase diagram of most substances, such as the one shown above, has a positive slope.

This is due to the solid phase having a higher density than the liquid, so that increasing the pressure increases the melting temperature, that is the temperature at which metal melts. However, in the phase diagram for water the solid-liquid phase boundary has a negative slope. This reflects the fact that ice has a lower density than water, which is an unusual property for a material.

In the pT-diagram, the phase boundary between liquid and vapour does not continue indefinitely. Instead, it terminates at a point on the phase diagram called the critical point. This reflects the fact that, at extremely high temperatures, the liquid and gaseous phases become indistinguishable, in what is known as a supercritical fluid. The critical point represents the thermodynamic point over which a difference between the gaseous and liquid state does not exists.

From a molecular point of view it is possible to say that for subcritical temperatures, as pressure increases (having constant temperature) the energy of the intermolecular force increases while the kinetic energy (related to the temperature) remains constant. When the interaction energy exceeds the kinetic energy a new bond between the molecules arises and the vapour transforms into a liquid. Over the critical temperature, however, the kinetic energy is so high that an intermolecular bond cannot be created and no change of state occurs, whatever is the pressure level. Hence, the weaker is the intermolecular bond, the lower is the critical temperature. This bond is weak in the case of helium ($T_c \simeq 5\ K$) while, due to the hydrogen bond, it is strong for water ($T_c \simeq 647\ K$).

For a subcritical temperature, a vapour can be transformed into a liquid by compression of the fluid and a two-phase transition occurs. For a supercritical temperature, on the contrary, a gas (i.e., low density fluid) can be transformed into a liquid (i.e., high density fluid) by compression without any abrupt density change (two-phase transition). Since, in this case, it is not easy to distinguish the gaseous state to the liquid state, the regime above the critical temperature is referred to as supercritical state. In this regime ($T > T_c$), however, a low pressure fluid ($p \ll p_c$) is a gas-like supercritical fluid while a high pressure fluid ($p \geq p_c$) is a liquid-like supercritical fluid. A gas-like fluid is characterized by low density, low viscosity and high thermal compressibility (i.e., attitude of a fluid in increasing density by an isothermal compression). A liquid-like fluid, on the contrary is characterized by high density, high viscosity and low thermal compressibility.

In the near-critical state, defined approximately by $1 < T/T_c < 1.5$ and $1 < p/p_c < 1.5$, the thermodynamic properties of the fluid show large variations. For instance specific heat at constant pressure and isothermal compressibility appears to approach infinity at the critical point (see Sec. A.6).

Considering pressure and volume as independent variables, a typical diagram that describes the behaviour of a pure substance is shown in Fig. 2.2.

In this diagram the two-phase transitions are clearly represented by surfaces

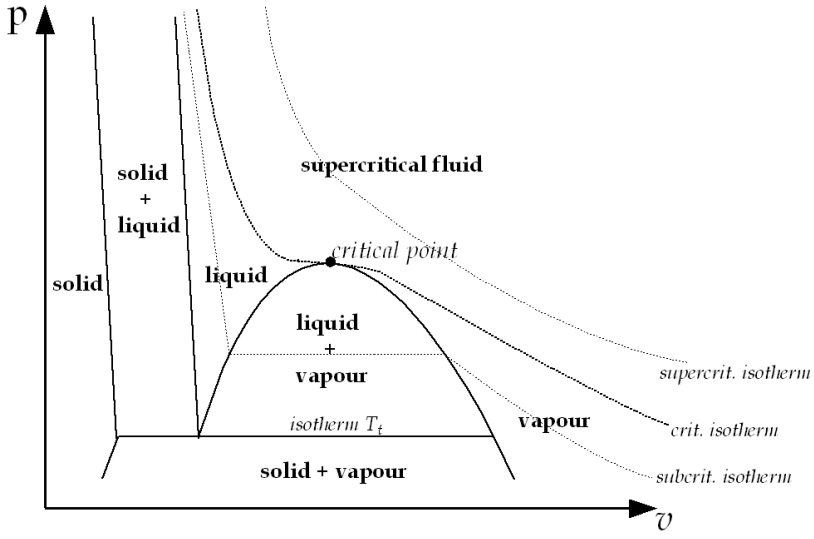

Figure 2.2: pv diagram of a pure substance.

and the triple point is, as a matter of fact, an isobaric/isotherm line in which solid, liquid and vapour states coexist. Moreover, the supercritical state is well bounded by the critical isotherm and the thermodynamic critical point (T_c and p_c) can be identified by the thermodynamic relations:

$$\begin{cases} \left(\dfrac{\partial p}{\partial v}\right)_T\Big|_{T_c,p_c} = 0 \\ \left(\dfrac{\partial^2 p}{\partial v^2}\right)_T\Big|_{T_c,p_c} = 0 \end{cases} \tag{2.1}$$

Note that the first relation affirms that the isothermal compressibility

$$\beta = -\frac{1}{v}\left(\frac{\partial v}{\partial p}\right)_T$$

is infinite at the thermodynamic critical point.

In Tab. 2.1 triple point, critical point and normal boiling temperature T_b (temperature of liquid/vapour transition at atmospheric pressure) of some pure substances are considered.

	$T_t\ [K]$	$p_t\ [mbar]$	$T_c\ [K]$	$p_c\ [bar]$	$\rho_c\ [kg/m^3]$	$T_b\ [K]$
H_20	273.16	6.1	647.10	220.64	322	373.12
N_2	63.18	125	126.19	33.96	313.3	77.35
H_2	13.84	70.4	33.19	13.15	30.12	20.39
O_2	54.36	1.52	154.58	50.43	436.1	90.19
F_2	53.56	22	144.41	51.72	592.86	85.04
CH_4	90.1	117	190.56	45.99	162.66	111.67
He	2.17	50.7	5.19	2.27	69.64	4.23
CO_2	216.55	5170	304.13	73.77	467.6	194.75
$C_{12}H_{26}$	263.5	0.0063	658.1	18.17	227	489.3

Table 2.1: Thermodynamic properties of some pure substances.

Note that a substance having a critical temperature over the room temperature ($288\ K$) is a liquid if the normal boiling temperature T_b is over the room temperature while it is a vapour if T_b is below the room temperature. The former case is the case of water or kerosene (which is a mixture of many hydrocarbon molecules, among which dodecane $C_{12}H_{26}$), while the latter one is the case of carbon dioxide which can be easily liquefied by compression. A substance having the critical temperature below room temperature is a supercritical fluid and thus it can be liquefied only by temperature subtraction. This is the case of cryogenic propellants (H_2, O_2, CH_4) that can be stored in liquid state only at low temperatures.

2.2 Equation Of State

2.2.1 Perfect gas EOS

The simplest equation of state for a pure substance is the perfect gas law:

$$p = \rho R T$$

where p is the pressure, ρ is the density, R is the gas constant (where $R = \Re/W$, $\Re$ is the universal gas constant and W is the molecular weight) and T is the temperature.

This law can be derived from the kinetic theory of gas and is based on the hypothesis that the molecules are rigid, pointwise particles that interact with each other only by means of collisions. This hypothesis is verified for a rarefied gas; in this state the molecules are so far that no attractive/repulsive force arises and they interact only by collisions. For a "real" fluid this molecular regime occurs at high

temperature (i.e., high kinetic energy) and low pressure (i.e., low intermolecular interaction energy):

$$\frac{p}{p_c} \ll 1 \quad \text{and} \quad \frac{T}{T_c} \gg 1$$

It is the case of hydrogen at room conditions ($T = 288\ K$ and $p = 1\ bar$) because its critical state is: $T_c = 33.19\ K$ and $p_c = 13.15\ bar$.

2.2.2 Van Der Waals EOS

The simplest modification of the perfect gas law in order to describe the fluid behaviour of supercritical fluids is the Van Der Waals equation of state:

$$p = \frac{\rho RT}{1 - b\rho} - a\rho^2 \tag{2.2}$$

The Van Der Waals equation of state is based on the idea that the pressure of a fluid results from the sum of repulsive and attractive forces:

$$p = p_{repulsive} + p_{attractive}$$

The repulsive part is represented by $\rho RT/(1 - b\rho)$ and the attractive part by $a\rho^2$. The Van Der Waals equation is based on the idea that pressure on a container wall, exerted by the impinging molecules, is decreased because of the attraction by the mass of molecules in the bulk gas; that attraction rises with density. Further, the available space in which the molecules move is less than the total volume by the excluded volume b due to the size of the molecules themselves. For that reason the coefficient a is called "intermolecular attractive force coefficient" and b is called "molecular size coefficient". These two coefficients can be determined from the critical state relations, Eq. (2.1):

$$\begin{cases} a = \dfrac{9}{8} RT_c v_c \\ \\ b = \dfrac{v_c}{3} \end{cases}$$

where v_c is the specific volume at the thermodynamic critical point: $v_c = 1/\rho_c$.

Eq. (2.2) is an example of the law of corresponding states. This principle expresses the generalization that equilibrium properties which depend on intermolecular forces are related to the critical properties in a universal way. In 1873, Van Der Waals showed it to be theoretically valid for all pure substances whose

pvT properties could be expressed by a two-constant equation of state. Corresponding states holds well for substances that can be characterized by the intermolecular force only, that is, substances containing spherically symmetric molecules (for example, CH_4). Moreover, upon semi-empirical extension, this principle holds for many other substances where molecular orientation is not important, i.e., for molecules that are not strongly polar or hydrogen-bounded [39].

The relation of pressure to volume at constant temperature is different for different substances; however, corresponding states theory asserts that if pressure, volume, and temperature are related to the corresponding critical properties, the function relating reduced pressure to reduced volume becomes the same for all substances. The reduced property is commonly expressed as a fraction of the critical property:

$$p_r = \frac{p}{p_c}, \quad v_r = \frac{v}{v_c}, \quad \text{and} \quad T_r = \frac{T}{T_c}$$

Thus, the universal equation of state can be written in the general form:

$$f\left(p_r, v_r, T_r\right) = 0$$

This equation can also be written with respect to the compressibility factor Z:

$$Z = Z\left(p_r, T_r\right) \quad \text{or} \quad Z = Z\left(v_r, T_r\right)$$

The compressibility factor is a non-dimensional parameter that expresses the deviation of the substance behaviour from the perfect gas one and it is defined as:

$$Z = \frac{p}{\rho R T}$$

For a perfect gas $Z = 1$. For real gases, Z is normally less than 1 except at high reduced temperatures and pressures. The above equation can also be used to define Z for a liquid; in this case Z is much less than unity. Its universal behaviour, according to the "corresponding states principle", is often presented by means of the so called "compressibility chart" (Fig. 2.3) in which the compressibility Z is a function of the reduced pressure p_r, having the reduced temperature T_r as a parameter.

Since the Van Der Waals law is a two coefficients equation of state, it can be written in the universal way via the compressibility factor:

$$Z\left(v_r, T_r\right) = \frac{1}{1 - 1/3v_r} - \frac{9}{8T_r v_r}$$

The Van Der Waals equation of state well describes the supercritical behaviour of substances with spherically symmetric molecules and it can be used, as first

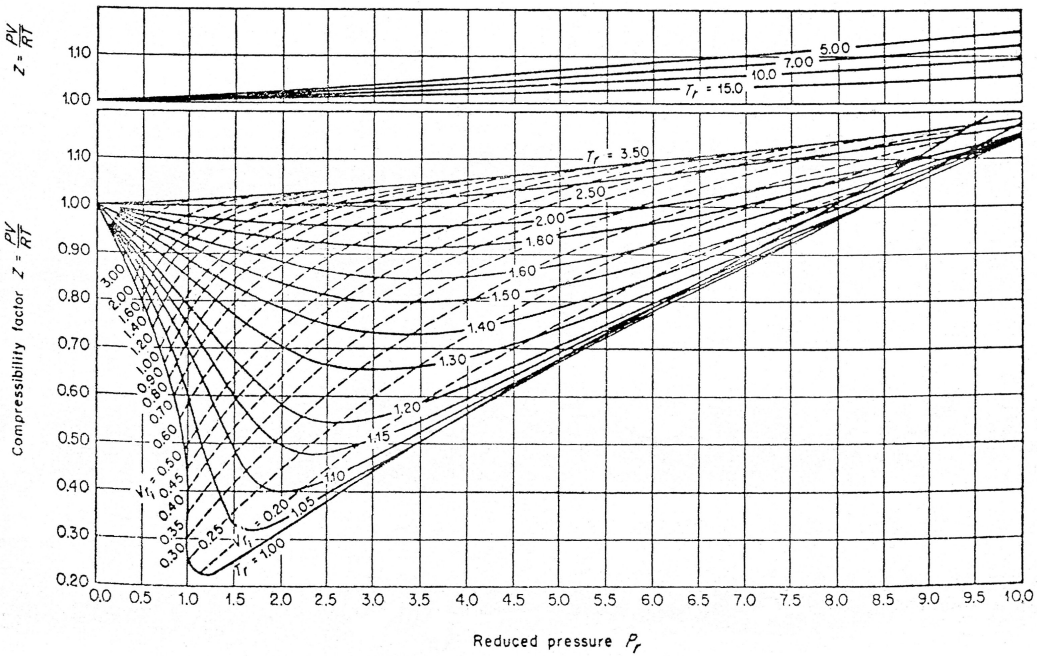

Figure 2.3: Generalized compressibility chart (from [39]).

approximation, to describe the supercritical behaviour of more complex molecules (such as polar, heavy, or hydrogen bounded molecules) even if equations of state with more coefficients are necessary for more accurate predictions. At last, Van Der Waals equation is not adequate to describe the near-critical or subcritical pvT behaviour.

2.2.3 Benedict Webb Rubin EOS

To better describe pure substance behaviour for both supercritical and subcritical (i.e., liquid and vapour) behaviour, a modified Benedict-Webb-Rubin equation of state is often used [8, 56]:

$$p(\rho, T) = \sum_{i=1}^{N_i} A_i(T) \cdot \rho^i + \sum_{j=1}^{N_j} B_j(T) \cdot \rho^{2j+1} \cdot e^{-\gamma\rho^2}$$

where $A_i(T)$ and $B_j(T)$ are polynomial functions in T and $1/T$, whose coefficients are determined by least-squares interpolation of empirical data. These family of equations depend on many coefficients (up to 32) depending on the accuracy required.

The main difficulty with these or any experimental-data curve-fit equations is determining other properties such as specific heat at constant pressure c_p, since this requires state equation derivatives which can be not very satisfactory near the critical point. In this case some correction is required for the c_p evaluation. Up to date, this family of equation of state represents the more accurate and efficient way to determine the pressure-volume-temperature behaviour of a fluid. For that reason this kind of equations has been used to describe hydrogen and methane pvT behaviour (see App. B and C)

2.3 Transport properties

The evaluation of the transport properties (viscosity and thermal conductivity) of a fluid is of great importance to describe its cooling properties. Since the coolant flow is often a high density subcritical/supercritical flow, the rarefied-gas model for transport properties is not accurate and thus transport properties are evaluated considering two contributions: rarefied-gas term and dense-fluid term. In the case of viscosity:

$$\mu = \mu_0 (T) + \mu_d (\rho, T)$$

where μ_0 represents the rarefied-gas term and, according to the molecular kinetic theory, is an increasing function of the temperature only, while the dense-fluid term μ_d is negligible for $\rho \to 0$ (rarefied gas) and is predominant in the case of dense-fluid.

In Fig. 2.4 the viscosity of carbon dioxide is shown: at low pressure the viscosity is essentially an increasing function of the temperature (gas-like behaviour), while at high pressure it is a decreasing function of the temperature (liquid-like behaviour). Viscosity is very sensitive to pressure in the near critical state (i.e., $1 < T/T_c < 2$).

The thermal conductivity behaviour is similar to that of viscosity, but an anomalous trend is present in the critical point vicinity: thermal conductivity seems to reach infinite value in the critical point (see Fig. 2.5).

This behaviour is not well understood and the thermal conductivity behaviour must take into account this anomalous spike. Thus thermal conductivity can be modeled in the following way:

$$k = k_0 (T) + k_d (\rho, T) + \Delta k_c (\rho, T)$$

where k_0 is the rarefied-gas contribution, k_d is the dense-fluid contribution and Δk_c is the critical enhancement. This latter term is zero outside the critical point region and can be neglected if we are not interested in the critical point

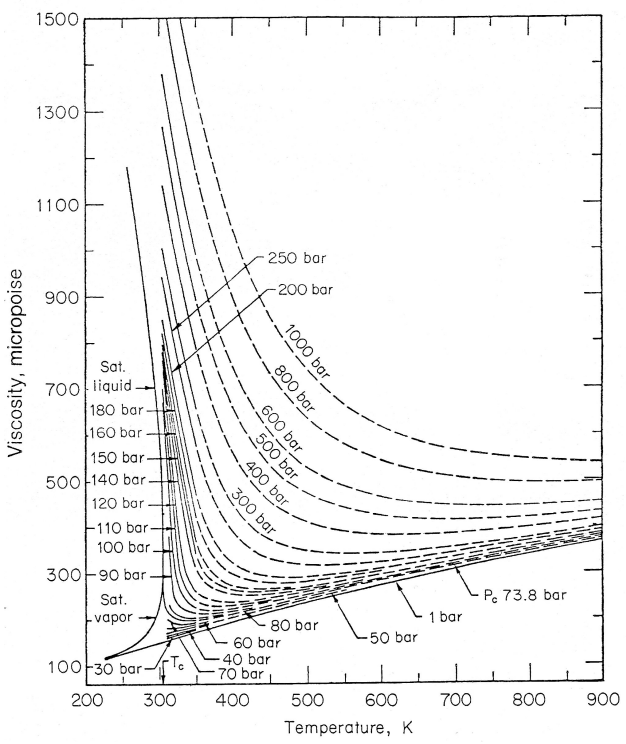

Figure 2.4: Viscosity diagram of carbon dioxide (from [39]).

behaviour. This is the case of the hydrogen and methane used in the regenerative cooling channels: since their working pressure is supercritical along the whole cooling circuit, they never pass through the critical point vicinity. Quite close to the thermodynamic critical point, viscosity also exhibits anomalous behaviour. Unlike thermal conductivity, where the anomalous behaviour is very strong, the anomalous behaviour of viscosity appears quite weak. For that reason it is always ignored.

2.4 Thermodynamic relations

In Sec. 2.2 the generic equation of state $p = p(\rho, T)$ has been discussed. Now we want to focus on the thermodynamic variables, such as enthalpy h, internal energy e, entropy s, specific heats c_p and c_v, and speed of sound a. These variables can be easily determined as functions of ρ and T using the equation of state in the general form $p = p(\rho, T)$ and its derivatives:

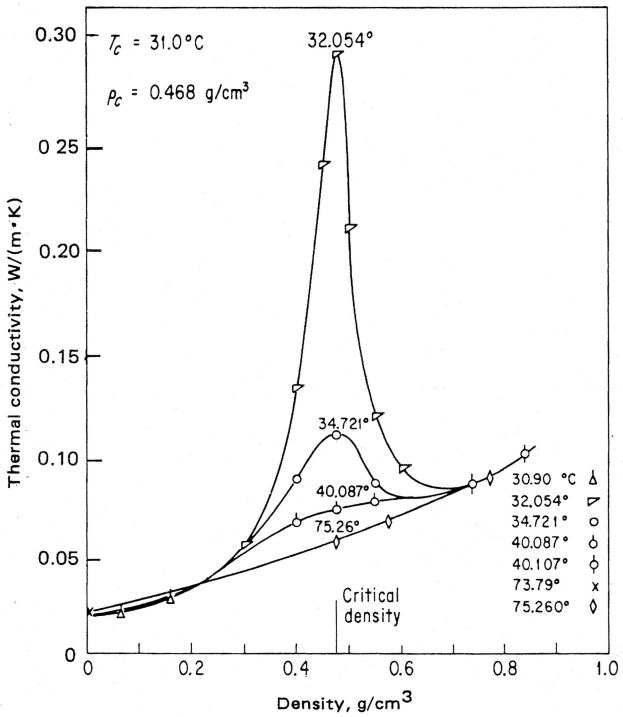

Figure 2.5: Thermal conductivity diagram of carbon dioxide near the critical point (from [39]).

- Entropy:

$$s\left(\rho,T\right)=s_0-R\ln\left(\frac{\rho RT}{p_0}\right)+\int_{T_0}^{T}\frac{c_{p0}(T)}{T}dT+\int_0^{\rho}\left[\frac{R}{\rho}-\frac{1}{\rho^2}\left(\frac{\partial p}{\partial T}\right)_{\rho}\right]_T d\rho$$

- Enthalpy

$$h\left(\rho,T\right)=h_0+\frac{p-\rho RT}{\rho}+\int_{T_0}^{T}c_{p0}(T)dT+\int_0^{\rho}\left[\frac{p}{\rho^2}-\frac{T}{\rho^2}\left(\frac{\partial p}{\partial T}\right)_{\rho}\right]_T d\rho$$

- Internal Energy

$$e(\rho,T)=h(\rho,T)-\frac{p}{\rho}$$

- Specific Heat at Constant Volume

$$c_v(\rho,T)=c_{p0}(T_0)-R-\int_0^{\rho}\left[\frac{T}{\rho^2}\left(\frac{\partial^2 p}{\partial T^2}\right)_{\rho}\right]_T d\rho$$

- Specific Heat at Constant Pressure

$$c_p(\rho, T) = c_v(\rho, T) + \frac{T}{\rho^2} \frac{\left(\frac{\partial p}{\partial T}\right)_\rho^2}{\left(\frac{\partial p}{\partial \rho}\right)_T}$$

- Speed of Sound

$$a(\rho, T) = \sqrt{\frac{c_p}{c_v} \left(\frac{\partial p}{\partial \rho}\right)_T}$$

where $c_{p0}(T)$ is the perfect gas specific heat and it is a function of the temperature only and T_0, p_0, $s_0 = s_0(p_0, T_0)$, and $h_0 = h_0(T_0)$ are the perfect gas reference variables (generally: $T_0 = 298.15$ K and $p_0 = 1.01325$ MPa).

The derivation of the above relations are presented in App. A while in App. B and App. C the equation of state used to evaluate hydrogen and methane behaviour are presented.

Note that the above relations can be computed analytically by differentiating the BWR polynomial equation of state with respect to temperature and density and by integrating the BWR equation of state and its derivatives

2.5 Methane

In this chapter the main features of methane as a space fuel will be described. Then some thermodynamic diagrams, obtained using the equation of state presented in App. C, will be shown.

2.5.1 Methane as a fuel for space propulsion

The advancements of space industry asking for high performance and low cost engines, drive researches towards new propellant combinations. Recent studies show LO_2/methane and LO_2/LNG (LNG: liquefied natural gas) propellant pair as a promising alternative to LO_2/kerosene, due to the high performance, good response to environmental constraints, high reusability potential and system flexibility they present. Reduced costs of supply (essentially valid for LNG), tanks, handle and safety systems make LO_2/methane and LO_2/LNG engines a potential competitor also to pure cryogenic engines (LO_2/hydrogen) [22]. Although no known LO_2/methane engines have been flown for aerospace applications, space agencies in the United States, Russia, Europe and Japan have been considering methane fueled propulsion system for various applications; these include: first

stage, second stage, booster, upper stage and in-space main propulsion system [44].

Methane is a low density hydrocarbon which has advantages similar to both kerosene and hydrogen and thus could be a convenient trade between them. Its critical temperature is $190.56\ K$ and its critical pressure is $51.72\ bar$. For that reason at room conditions ($T = 298\ K$, $p = 1\ bar$) methane is a low density supercritical gas ($\rho = 0.64\ kg/m^3$) and liquefies at temperatures below $111.51\ K$ (normal boiling point temperature) with a density of $423\ kg/m^3$.

The operational condition relative to the critical condition of the propellant used for cooling is an important parameter when assessing the thermodynamic state of the fluid: liquid, near critical or supercritical fluid. Hydrogen is typically operated in the supercritical gas regime, methane in a so called transcritical regime, and kerosene well below the critical temperature in the liquid regime. Since physical properties are known to considerably change in the vicinity of the critical state of a fluid, coolant flow parameters and characteristics are likely to vary stronger for methane than for kerosene. In practice, methane enters the engine's cooling circuit in a liquid state ($T_{cc,in}/T_c < 1$) and leaves it in a supercritical state ($T_{cc,exit}/T_c > 1$), whereas kerosene remains in a liquid state throughout the entire cooling circuit ($T_{cc,exit}/T_c = 0.6$) [38].

More precisely, according to [44], in a LO_2/methane expander cycle, liquid methane is stored in tank at pressure of $p = 1.7\ bar$ and at the subcritical temperature of $T = 111\ K$. Then methane is pumped in the cooling channel circuit at $130\ bar$ with a temperature of $130\ K$. Along the cooling channels methane is heated and thus becomes supercritical ($T_{cc,exit} = 530\ K$); finally, after the expansion in the turbine it is injected in the combustion chamber at $60\ bar$.

Methane, as a rocket fuel, has many performance and property characteristics that make it desirable for applications in aerospace propulsion. Out of common hydrocarbons, methane (in combination with liquid oxygen) has the highest vacuum specific impulse of about 370 seconds; in comparison, kerosene, the closest chemical hydrocarbon has a vacuum specific impulse of about 355 seconds [44]. Moreover, methane is a "soft" cryogenic that is not corrosive (very low percentage of sulfur compounds) and has a very low toxicity; thus it is easier to store, requires less insulation and fewer handling concerns than comparable hydrogen fuel systems. Liquid methane is about six times denser than liquid hydrogen; thus, methane tanks weigh much less and/or require less storage volume than comparable hydrogen tanks. Furthermore, methane has exceptional heat capacity properties that provides "superior cooling properties"; methane fuel has lower pressure drops in regenerative cooling channels as compared to kerosene fuel. Additionally, methane is a natural gas that is relatively easy to extract on Earth and is about 5 to 10 times cheaper to acquire and store than liquid hydrogen [44].

Methane, as most hydrocarbon molecules, is known to exhibit sooting and

coking. These two phenomena are well known in each combustion device using hydrocarbon as propellants. While soot is a combustion product due to heavy aggregates of carbon molecules, coke is formed due to thermal decomposition of hydrocarbons in the boundary layer of ducts and cooling channels. In existing LO_2/kerosene engines formation of carbon layer on the hot-gas side of combustion chamber has been observed with the global effect of: heat transfer insulation, increase of radiative heat due to black body radiation, and change in throat shape.

Soot has a dramatic effect on turbine blades erosion in engines using fuel rich gas generator, too. The presence of a broad set of aliphatic compounds in the inlet mixture reduces the time required for complex compound formation, while the presence of aromatic compounds works as agglomeration point around which more complex aromatic molecules might be created and evolve to soot [22].

Coking decomposition of the molecule exhibits when a hydrocarbon based propellant (such as kerosene and methane) gets in contact with metallic surfaces at elevated temperatures. For that reason coking problem is generally present in the ducts of regenerative cooling circuits. According to [22], wall temperature limit to generate coking is $970\ K$ for methane and $560\ K$ for kerosene. Moreover, the process of coke formation is quite insensitive to pressure, especially at higher temperatures. At last, methane coking and soot decomposition are of minimal concern as compared to kerosene and other complex hydrocarbon fuels; this allows for reusability, multiple-restarts and longer burn times.

2.5.2 Methane diagrams

Using the equation of state presented in App. C, pvT and transport properties behaviours of methane have been plotted. The accuracy of the used equation of state is in perfect agreement with the data published by the National Institute of Standards and Technology (NIST) [2].

In Fig. 2.6 the typical pressure-volume-temperature diagram is presented. The volume axis is in logarithmic scale to better value the two-phase region (empty zone in the lower part of the diagram). The critical isotherm ($190.53\ K$) bounds the subcritical (i.e., liquid and vapor) region from the supercritical region. It is clear that in the liquid regime (high density) the isothermal compressibility is very low since the subcritical isotherms are almost vertical ($\left(\frac{\partial p}{\partial v}\right)_T \rightarrow \infty$), while in the supercritical region the isotherms slope is less pronounced (higher isothermal compressibility). Finally, for temperature far over the critical temperature the isotherms almost shape as hyperbolas and the pvT behaviour can be described by the hyperbolic law of perfect gas: $T \propto pv$.

In Fig. 2.7 the compressibility chart (Z vs p) is presented. The compressibility is a non-dimensional parameter which is defined as the deviation from the perfect gas equation of state: $Z = p/\rho RT$. For subcritical fluid ($T < T_c$) Z is almost lin-

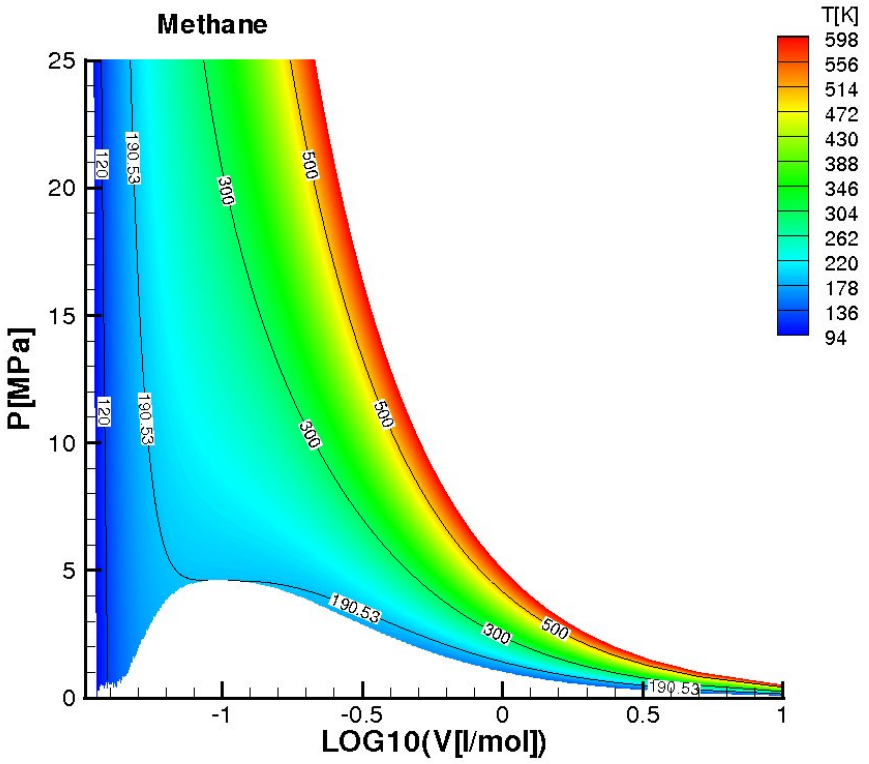

Figure 2.6: Methane PVT diagram.

ear with pressure, having very high compressibility (up to 3) for high pressurized liquid (beyond 20 MPa) and very low compressibility for low pressure region (vapor and liquid). For supercritical fluid ($T > T_c$) Z is a decreasing-increasing function of pressure. For high temperature the fluid is almost an ideal gas and compressibility is close to the ideal value ($Z = 1$).

In Fig. 2.8 the isothermal compressibility behaviour is shown on the two-dimensional diagram p-v. Note that the low compressibility in the high density region is clear, such as the high compressibility (theoretically infinite) at the critical point (see App. A for more details).

In Fig. 2.9 the molar specific heat at constant pressure is shown on the two-dimensional diagram p-v. As theory states (see App. A) c_p reaches an infinite value at the critical point. Differently from isothermal compressibility, this peculiar behaviour protrudes far over the critical pressure ($4.6\ MPa$); hence, along an isobar, the specific heat exhibits a peak at a temperature close to the critical one.

This behaviour is clearly shown in Fig. 2.10 (c_p vs T). In particular, as pres-

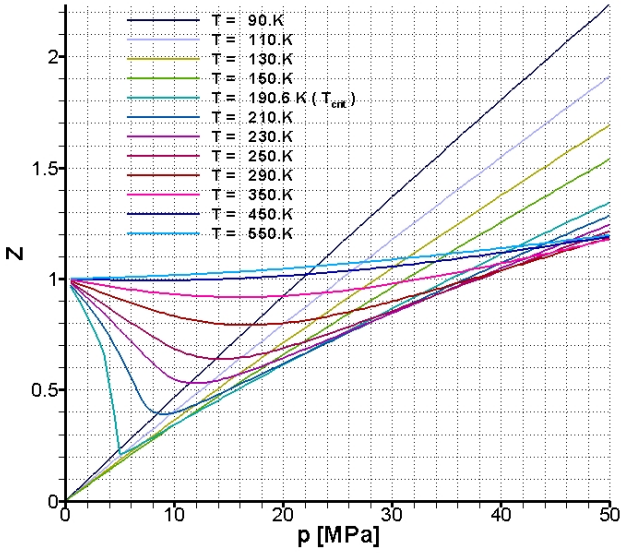

Figure 2.7: Methane compressibility chart.

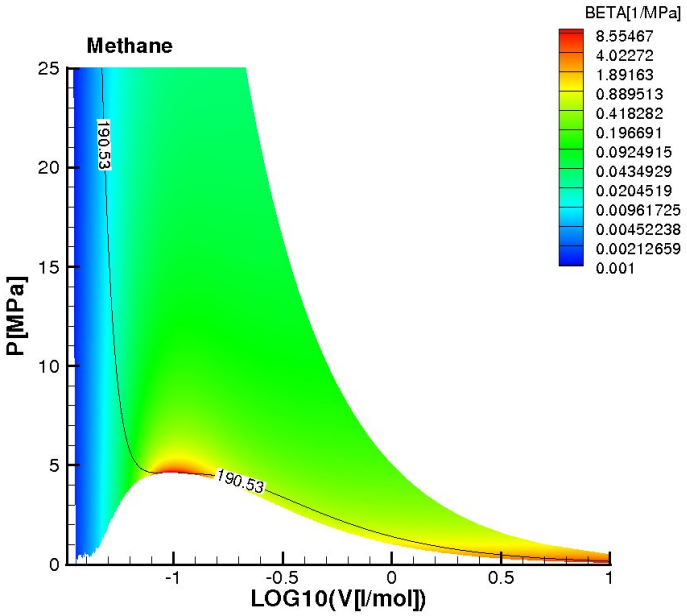

Figure 2.8: Methane isothermal compressibility diagram.

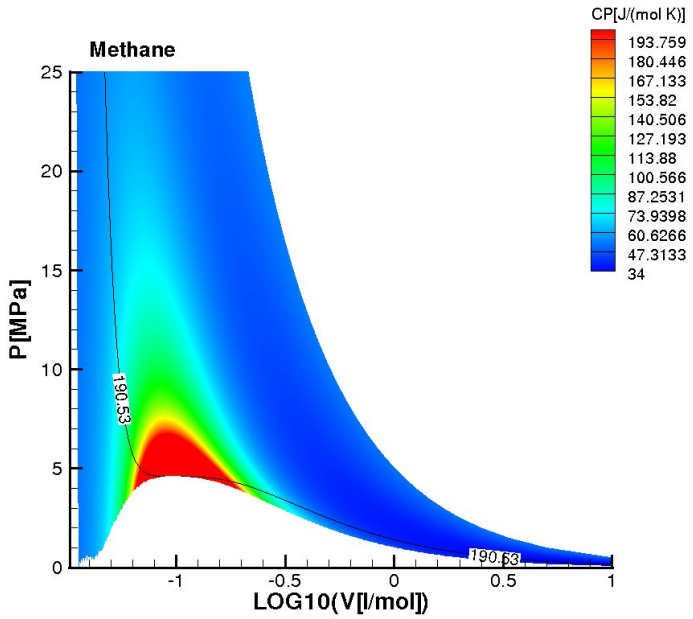

Figure 2.9: Methane molar heat at constant pressure diagram.

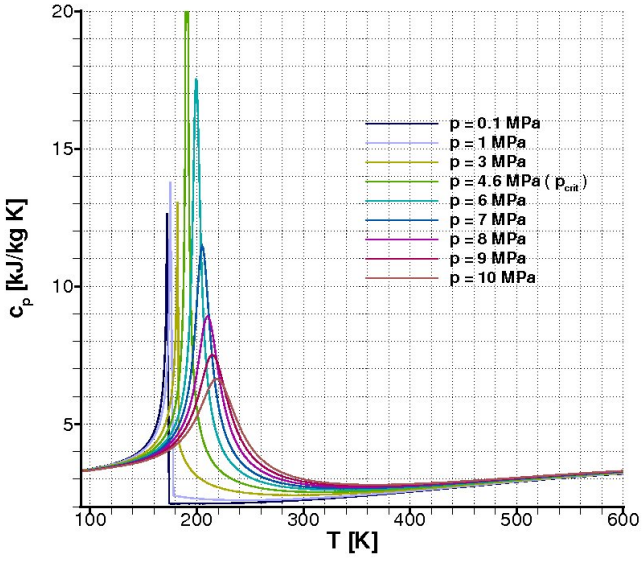

Figure 2.10: Methane specific heat at constant pressure behaviour.

sure increases, the specific-heat peak reduces while the temperature of maximum c_p increases. This temperature is called pseudo-critic since it can be considered as a boundary between the "liquid-like" behaviour and the "gas-like" behaviour of a supercritical fluid. For that reason, the locus of the pseudo-critic temperatures can be considered as an extension of the vapour/liquid phase boundary beyond the critical temperature (see Fig. 2.1). In case of thermally perfect gas (high temperature), specific heat is an increasing function of temperature and is not affected by pressure. This different behaviour between the high density fluid (strong dependency from pressure and temperature) and perfect gas (weak dependency from temperature only) well demonstrates that the fluid operating in high density regime must be described using proper theory and equation of state.

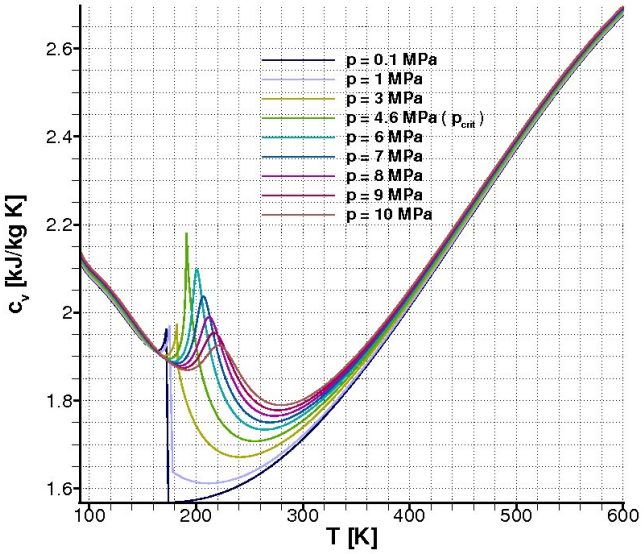

Figure 2.11: Methane specific heat at constant volume behaviour.

In Fig. 2.11 specific heat at constant volume vs temperature is presented. Note that, even if c_v does not reach infinite value at the critical point, its behaviour shows a peak value close to the critical temperature. However, this peak is less pronounced than for c_p.

In Fig. 2.12 the behaviour of the speed of sound is shown having temperature on the x-axis and pressure as parameter. Over $300\ K$ the speed of sound is almost insensitive to the pressure and its dependency to temperature is well predicted by perfect gas theory ($a \propto \sqrt{T}$). Since isothermal compressibility is very low in the high density region (low temperatures) the speed of sound in this region is far

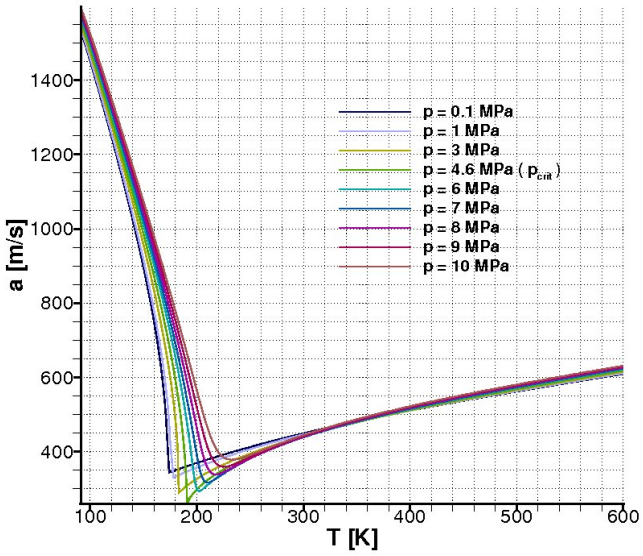

Figure 2.12: Methane speed of sound behaviour.

higher than for low density fluid ($a^2 \propto 1/\beta$). Moreover in this region speed of sound is a decreasing function of temperature and it reaches a minimum in the near critical region (since the isothermal compressibility is maximum).

Viscosity behaviour on the two-dimensional diagram p-v and versus temperature is shown on Fig. 2.13 and Fig. 2.14 respectively. Viscosity dependency on pressure is weak for both supercritical and subcritical region. Obviously this rule does not apply in the near critical region. In the supercritical region viscosity is a weak increasing function of temperature ($\mu \propto \sqrt{T}$ as kinetic theory states) while in the subcritical region viscosity is a decreasing function of temperature. In fact gas molecules are excited by temperature and then transport properties (i.e. molecules shock frequency) are magnified while liquid intermolecular bonds are destroyed by temperature excitement, hence reducing the transport capability of the liquid molecules. Moreover, due to the different liquid/gaseous molecule bond, liquid transport properties are much higher (up to 20 times) than gas transport properties.

Thermal conductivity behaviour on the two-dimensional diagram p-v and versus temperature is shown on Fig. 2.15 and Fig. 2.16 respectively. Since thermal conductivity is a transport property, its behaviour is similar to that of viscosity. The only difference relies on the critical point enhancement (see Sec. 2.3). In the equation used, this behaviour is modeled in a very simple and rough way (see

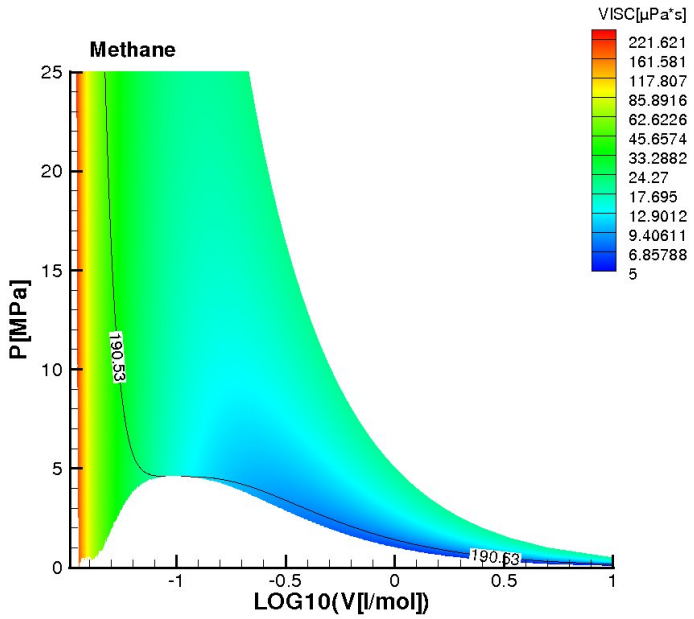

Figure 2.13: Methane viscosity diagram.

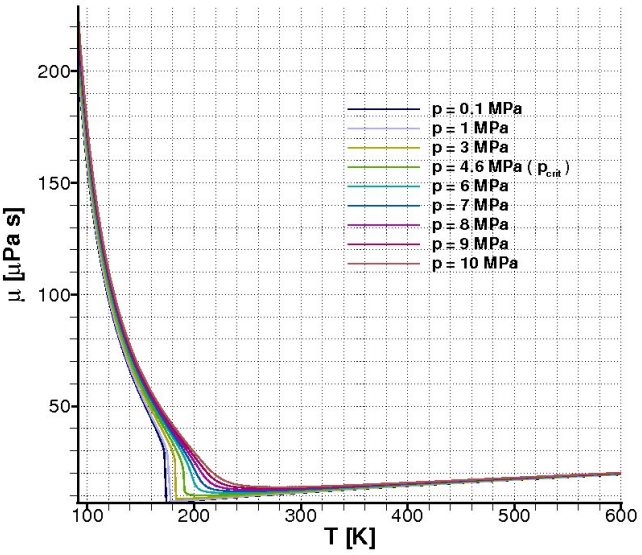

Figure 2.14: Methane viscosity behaviour.

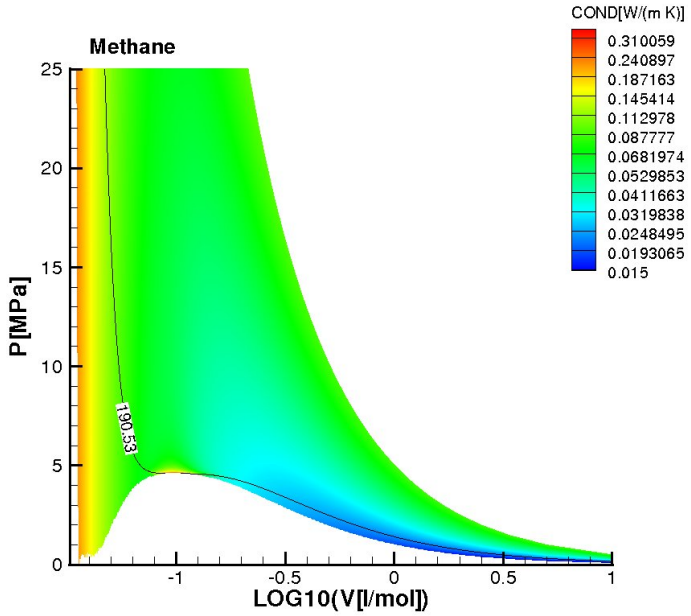

Figure 2.15: Methane thermal conductivity diagram.

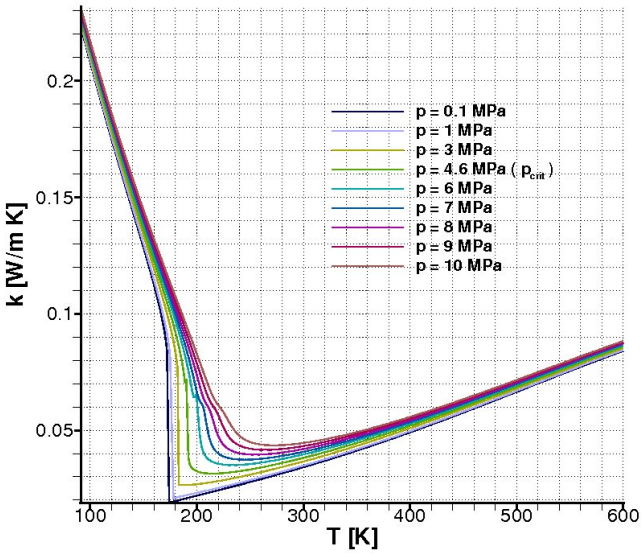

Figure 2.16: Methane thermal conductivity behaviour.

App. C for more details) since it does not affect the transcritical methane flow in cooling channels; in fact, in that environment, while temperature is transcritical, pressure is not: methane does not pass through critical point. Therefore, the irregular behaviour of thermal conductivity is slightly visible on Fig. 2.15.

Chapter 3

1D model

The objective of this chapter is to analyze the regenerative cooling system by means of a one-dimensional steady-state model. In fact hot-gas and coolant flow can be treated as one-dimensional flows coupled each other by means of radial heat transfer through the wall material. The hypothesis of one-dimensional model implies that the variables that describe the flow are functions of the streamwise direction only. For that reason, their value must be considered as the mean value in the cross section. In case of duct flow (such as the hot-gas and coolant flow), the considered mean value is the "bulk" value, defined as:

$$\phi_b = \frac{1}{\dot{m}} \int_A \rho u \phi \, dA$$

where ϕ is the generic flow variable, $\dot{m}$ is the mass flow rate through the duct of section A and ρ and u are the density and velocity of the flow. Note that ρ, u and ϕ varies across the section A while ϕ_b is the mean value. The one-dimensional approach is based on the "bulk" variables and thus in what follows the subscript b is omitted.

The "simple and fast" one-dimensional tools have been widely used in industrial practice and many cooling systems have been designed using this approach. The one-dimensional model is strongly based on semi-empirical relations to describe hot-gas and coolant convective heat transfer and coolant pressure loss. These relations are generally calibrated by means of data collected in subscale engine tests and thus they are strongly related to the operative working conditions of the considered engine.

In this chapter the one-dimensional approach is described since it is the basis of the "quasi 2D" model presented in Chap. 4. Moreover, the simple one-dimensional model can be used to show the effect of channel aspect ratio on cooling performances (see Sec. 3.6)

3.1 Physical and mathematical modeling

Heat transfer in a regeneratively cooled thrust chamber can be described as the heat flux between two moving fluids, separated by a solid wall. In its simplest form regenerative cooling can be modeled as a steady heat flux from a hot-gas through a solid wall to a cold fluid. This problem can be divided up into three sub-problems, which are defined as follows:

- The turbulent chemically reacting flow of a mixture of gases in a rocket engine, including combustion chamber and converging-diverging nozzle.
- The heat conduction through the wall of the rocket engine between the hot-gas and the liquid coolant.
- The turbulent flow of the coolant in the channels surrounding the rocket engine.

These subproblems are coupled by the two steady-state balances of three heat fluxes:

- heat flux from hot-gases to the wall (see Sec. 3.2)
- heat flux through the wall (see Sec. 3.5)
- heat flux from the wall to the coolant (see Sec. 3.3)

3.2 Hot-gas expansion

The hot-gas flow is formulated on the basis of a one-dimensional isentropic expansion (i.e., one-dimensional flow model with variable area of the cross section). Depending on the model refinement, the chemical reactions can be considered or not. In the numerical tool proposed in Chap. 4 the hot-gas flow is considered with chemical reactions and its thermodynamic and transport properties are evaluated using the software CEA [30, 31, 3]. Combustion conditions are obtained with the assumption of chemical equilibrium of the combustion products. The hot-gas expansion is then calculated assuming chemical equilibrium or frozen composition (freezing point at chamber or at throat conditions). The expansion of the hot-gas is considered independent of the wall temperature, because the heat transfer from the hot-gas to the wall causes very little change in the gas temperature (see Sec. 1.2).

The convective wall heat fluxes q_w is generally expressed as the product of a heat transfer coefficient h and a driving potential which represents the difference of the energy levels between free stream and wall. The object of this “separation of

variables" is to arrive at a coefficient h which is independent of both the difference and the absolute levels of the energy in the free stream and wall.

For a high-speed flow (such as the hot-gas case) the driving potential is based upon the *recovery temperature*:

$$q_w = h\left(T_{aw} - T_w\right) \tag{3.1}$$

where T_{aw} is the adiabatic wall temperature (or recovery temperature) and T_w is the wall temperature at the hot-gas side. Note that q_w is considered positive if the heat flux exits the hot-gas. The adiabatic wall temperature can be expressed as:

$$T_{aw} = T\left(1 + r\frac{\gamma - 1}{2}M^2\right) \tag{3.2}$$

where M is the free stream Mach number, T is the free stream temperature, γ is the specific heats ratio and r, the recovery factor, has been shown by both theory and experiment to be related to the Prandtl number; for turbulent boundary layers [7]: $r = Pr^{1/3}$.

Regarding heat transfer coefficient, experience gained from the turbulent boundary layer calculation methods in rocket nozzle (Bartz et al. [7]) has shown that the variation of the local mass flow rate per unit area at the edge of the boundary layer is the dominant variable affecting the heat transfer distribution. Variations in velocity and temperature across boundary layer exert only a secondary, although not negligible, effect.

Starting with the assumption that the local heat-transfer coefficient is principally dependent on local mass flow rate per unit area, one obtains:

$$h \sim (\rho u)^m \tag{3.3}$$

where ρ and u are the free stream density and velocity. Eq. (3.3) can account for mass flow rate variations by proper selection of m while it ignores the effect of boundary layer development. From [5] the proper value of the exponent m is 0.8.

Bartz suggested that by selecting some linear dimensional variable that varies in even a rough approximation to the variation of the boundary layer, a closed-form correlation-equation could be found that might approximate the results of a more complex analysis reasonably well. Such an equation was developed [6] by selecting the local diameter D at the station of the nozzle of interest as the linear dimension (only near the nozzle entrance for an initially thin boundary layer this selection appeared to be qualitatively inappropriate).

The equation proposed by Bartz is the familiar Nusselt-Reynolds type equation:

$$Nu = C\ Re^{0.8} Pr^{0.4}$$

where:

- $Nu = \dfrac{hD}{k}$ is the Nusselt number
- $Pr = \dfrac{\mu c_p}{k}$ is the Prandtl number
- $Re = \dfrac{\rho u D}{\mu}$ is the Reynolds number

The Nusselt and Reynolds numbers are based on the local diameter D, which was assumed to be the characterizing linear dimension. The value of 0.4 is arbitrarily selected as that frequently used for modifications of Reynolds analogy for Pr near unity.

Thus the closed-form approximation is complete except for an arbitrary constant C. The value of C might be selected so as to force agreement of the closed-form equation and results of a boundary-layer solution (or of an experiment) at one particular point in the nozzle. Bartz evaluated C to be 0.026 by forcing agreement at the throat with first-approximation results for a particular nozzle configuration (the value of C as determined from an iterative solution [6] of the same nozzle configuration was 0.0225). For other nozzle configurations and conditions this constant would vary, but fortunately it does not very drastically.

The simple closed-form equation proposed by Bartz for rapid estimation of rocket nozzle convective heat transfer coefficient is therefore:

$$Nu = 0.026\ Re^{0.8} Pr^{0.4} \tag{3.4}$$

The problem of where to evaluate the physical properties arises since in general large temperature differences are present across the boundary layer of rocket nozzles. If properties are evaluated at the film temperature (as proposed by Bartz et al.) Eq. (3.4) can be solved for h to give:

$$h = \frac{0.026}{D^{0.2}} \left(\frac{\mu^{0.2} c_p}{Pr^{0.6}} \right)_f (\rho_f u)^{0.8} \tag{3.5}$$

where the subscript f denotes properties evaluated at edge composition (i.e., the composition outside the boundary layer) and at the film temperature, that is the arithmetic mean between bulk temperature T (at the edge of the boundary layer) and wall temperature T_w:

$$T_{film} = \frac{1}{2} (T + T_w)$$

Based on Eq. (3.5) Bartz made some simplifying assumptions to make it even simpler to use:

- It is assumed that both c_p and Pr do not vary appreciably with temperature and they can be evaluated at stagnation conditions (denoted by 0). The properties whose variations must be accounted for are only μ and ρ.

- μ_f and ρ_f can be evaluated in terms of the stagnation and static temperature values, respectively. Introducing the factor σ (which contains the corrections for property variation across the boundary layer) the Eq. (3.5) becomes:

$$h = \frac{0.026}{D^{0.2}} \left(\frac{\mu^{0.2} c_p}{Pr^{0.6}} \right)_0 (\rho u)^{0.8} \sigma$$

  with:

$$\sigma = \left(\frac{\rho_f}{\rho} \right)^{0.8} \left(\frac{\mu_f}{\mu_0} \right)^{0.2}$$

- Assuming that $\rho \sim \frac{1}{T}$ and $\mu \sim T^{\omega}$ (with $\omega = 0.6$) the value of σ can be evaluated in terms of T_0, T_w and M (using the quasi one-dimensional relations):

$$\sigma = \frac{1}{\left[\frac{1}{2} \frac{T_w}{T_0} \left(1 + \frac{\gamma - 1}{2} M^2 \right) + \frac{1}{2} \right]^{0.8 - \omega/5} \left[1 + \frac{\gamma - 1}{2} M^2 \right]^{\omega/5}}$$

- Finally the equation for h can be put in a form suitable for rocket nozzle computations by evaluating ρu in terms of c^* (characteristic velocity) and $\frac{A_*}{A}$ (using the quasi one-dimensional relations) where A_* is the cross-sectional area at the nozzle throat:

$$h = \left[\frac{0.026}{D_*^{0.2}} \left(\frac{\mu^{0.2} c_p}{Pr^{0.6}} \right)_0 \left(\frac{p_c}{c^*} \right)^{0.8} \right] \left(\frac{A_*}{A} \right)^{0.9} \sigma \tag{3.6}$$

Eq. (3.6) is the final form proposed by Bartz [6] and it is one of the most used approaches to estimate the nozzle convective heat transfer. Note that the factor in brackets is a constant through the nozzle, leaving only $\frac{A_*}{A}$ and σ to be evaluated at each station.

It is important to remember that the constant $C = 0.026$ has been determined for a particular rocket nozzle and so it may be modified to obtain a better agreement with numerical or experimental data, when available.

Note that, as the hot-gases parameters are estimated via the one-dimensional isentropic expansion law, at each axial position the wall heat flux q_w (Eq. (3.1), (3.2), and (3.6)) is only a function of the unknown temperature T_w.

3.3 Coolant flow

The coolant flow is modeled by means of the steady-state laws of mass, momentum and energy, taking into account the effects of heat transfer and friction. A one-dimensional flow model along the axial direction is assumed for the coolant flow, that is, the velocity vector is composed by the axial component only and the flow variables are functions of the abscissa x only. The integral steady-state coolant governing equations are:

$$\begin{cases} \dfrac{d}{dx}\displaystyle\iint_A \rho u dA = 0 & \Longrightarrow \text{ mass eq.} \\ \dfrac{d}{dx}\left[\displaystyle\iint_A \left(\rho u^2 + p\right) dA\right] dx - p\dfrac{dA}{dx}dx = -\displaystyle\iint_{S_w} \tau_w dS_w & \Longrightarrow \text{ momentum eq.} \\ \dfrac{d}{dx}\left[\displaystyle\iint_A \left(\rho u h_0\right) dA\right] dx = \displaystyle\iint_{S_w} q_w dS_w & \Longrightarrow \text{ energy eq.} \end{cases}$$

where $\rho(x)$ is the density, $u(x)$ is the axial velocity, $p(x)$ is the pressure and $h_0(x)$ is the stagnation enthalpy ($h_0 = h + u^2/2$). The channel cross section has an area $A(x)$ and a perimetrical area $S_w(x) = P_w(x)dx$ (P_w is the perimeter) along which the shear stress τ_w originates and across which the heat flux q_w passes. The shear stress τ_w and the wall heat flux q_w can be related to the flow variables by the skin friction factor f and the heat transfer coefficient h, respectively:

$$\tau_w = \frac{1}{8}\rho u^2 f$$

and

$$q_w = h(T_w - T)$$

where $T_w(x)$ is the wall temperature and $T(x)$ is the coolant temperature. Note that the convective heat flux q_w is described by means of a transfer coefficient form (as already seen in Sec. 3.2 for the hot-gas convective heat transfer) and

the shear stress τ_w is expressed by means of the Darcy definition of the friction factor; both h and f can be estimated using proper semi-empirical relations (see Sec. 3.4). Finally, the coolant governing equation based on the one-dimensional steady-state model are:

$$\begin{cases} \dfrac{d}{dx}(\rho u A) = 0 & \Longrightarrow \text{ mass eq.} \\ \dfrac{dp}{dx} + \rho u \dfrac{du}{dx} + \dfrac{1}{2}\rho u^2 \dfrac{f}{D_i} = 0 & \Longrightarrow \text{ momentum eq.} \\ \rho u A \dfrac{dh_0}{dx} = h(T_w - T)P_w & \Longrightarrow \text{ energy eq.} \end{cases} \tag{3.7}$$

where $D_h = 4A/P_w$ is the hydraulic diameter. In case of circular cross section D_h is equal to the geometric diameter of the cross section; otherwise it represents a reasonable characteristic length of the cross section. In the coolant energy equation the hypothesis of constant wall heat flux around the channel perimeter is assumed, and thus the heat transfer rate entering in the coolant has been expressed as:

$$\iint_{S_w} q_w dS_w = q_w P_w dx$$

where q_w is the constant heat flux that enters the coolant. In case of non uniform heat flux distribution along the channel perimeter the above expression is simply expressed as:

$$\iint_{S_w} q_w dS_w = dQ_w$$

where dQ_w is the heat transfer rate entering the coolant.

3.4 Coolant semi-empirical relations

Semi-empirical relations must be used to describe the skin friction factor f and the heat transfer coefficient h for the coolant flow.

Literature offers many formulas obtained by fitting of experimental data which are correlated using the typical dimensional theory; in the case of flow inside duct, the main non-dimensional numbers are:

- Reynolds number $Re = \dfrac{GD}{\mu}$

- Nusselt number $Nu = \dfrac{h_w D}{k}$
- Prandtl number $Pr = \dfrac{\mu c_p}{k}$

where $G = \rho u$ is the mass flow rate per unit area, D, the diameter of the duct, is assumed as the characteristic linear dimension, and μ, k, and c_p are the viscosity, thermal conductivity and specific heat at constant pressure of the fluid. Experimental data are often referred to straight and smooth duct with circular cross section and constant properties (i.e., adiabatic and low velocity flow) and the fluid can be laminar or turbulent. Generally these formulas are modified by correction factors accounting for non-circular cross section, roughness, variable properties, entrance effects, asymmetric heat flux and duct curvature. Regarding flow regime, we are interested in turbulent flow only because it is the actual flow regime in regenerative cooling channels. In fact in this application Reynolds number is of the order of $10^6 - 10^7$ [14] while under "usual" conditions the critical Reynolds number above which the flow is turbulent and below which the flow is laminar, is:

$$Re_{critical} = 2300$$

In this framework we have neglected entrance effect and duct curvature effect since these effects are often modeled ambiguously and they seem to be too much sensitive to the experimental conditions. In the following subsections the other effects that deviate heat transfer and friction loss from the standard conditions will be briefly discussed.

3.4.1 Skin friction and heat transfer at constant properties

Consider the heat transfer solution for the case of fully developed flow with constant properties in a circular tube with constant heat flux at wall. This situation is not physical because it is possible to have constant properties flow only in the adiabatic case; anyway it is possible to solve the non-adiabatic governing equations considering constant properties. The results obtained in this way will be representative of real case with little wall heat flux, so that flow properties vary slightly along the tube cross section.

The analytical calculations made by Petukhov [35] over the range $10^4 < Re < 5 \cdot 10^5$ and $0.5 < Pr < 2000$ are described by the interpolation equation:

$$Nu = \frac{(f/8)\, RePr}{k_1\,(f) + k_2\,(Pr)\,(Pr^{2/3} - 1)\,\sqrt{f/8}} \tag{3.8}$$

where

$$f = (1.82 \log_{10} Re - 1.64)^{-2}$$

and

$$k_1(f) = 1 + 3.4f$$

$$k_2(Pr) = 11.7 + 1.8Pr^{-1/3}$$

The disagreement of the predicted analytical Nu with Eq. (3.8) is within 1%. If in Eq. (3.8) $k_1(f)$ and $k_2(Pr)$ are taken constant and equal to 1.07 and 12.7 respectively, the equation becomes simpler but the disagreement is within $5-6\%$. The divergence of the experimental data from predictions of Eq. (3.8) does not exceed $5-6\%$ (except for a few points).

Empirical equations of the following type are widely used in practice:

$$Nu = c\, Re^m Pr^n \tag{3.9}$$

Comparing this equation with Eq. (3.8), it is easy to see that using constant c, m and n it is impossible to describe with a reasonable accuracy the change of Nusselt number with Re and Pr over a wide range of these parameters. A direct comparison of Eq. (3.9) with experimental data leads to the same conclusion. An equation of the type Eq. (3.9) can be used only assuming that c, m and n are functions of Re and Pr. Parameters c, m and n can be considered constant only for small variations of Re and Pr. An example of empirical formula with constant parameters is the well known Dittus's and Boelter's equations [12]:

$$Nu = 0.023\, Re^{0.8} Pr^{0.4} \tag{3.10}$$

This equation is reasonably accurate for $0.7 < Pr < 120$, $10000 < Re < 120000$ and $\frac{x}{D} > 60$ (i.e., far from the duct inlet).

3.4.2 Non circular cross section

Channels in regenerative system have a cross sectional area far from the circular one, especially for high aspect ratio channel.

It has become customary to base the Reynolds and Nusselt number for such cross sections on a length which is called "hydraulic diameter" and which is defined by the equation:

$$D_h = \frac{4A}{P_w}$$

where A is the cross-sectional area and P_w is the wetted perimeter. The whole wetted perimeter must be used also in the case when only part is heated or cooled

[13]. With some caution, we may use D_h directly in place of the circular tube diameter when calculating turbulent heat transfer and skin friction coefficients. The results obtained by substituting D_h for D in turbulent circular tube formulas are generally accurate within $\pm 20\%$ and are often within $\pm 10\%$. Worse results are obtained for duct cross-sections having sharp corners, such as an acute triangle [29].

3.4.3 Roughness

Previous discussions have assumed the wall to be smooth. Manufacturing and operating conditions are often far from ideal, leading to the duct walls that are rough.

An inherent difficulty in investigations of the influence of surface roughness is caused by the fact that no satisfactory geometric description of a rough surface by a limited number of parameters has been found as yet. It is generally assumed that the most important parameter is the ratio of the average height of the roughness elements to the tube diameter: ε/D. In his extensive experiments on friction in tubes with rough surfaces, Nikuradse produced a defined roughness pattern by gluing sand of fairly uniform size to the tube surface to form a cover which was made as dense as possible. Friction factors determined in this way are plotted in Fig. 3.1 with Reynolds number on the abscissa and with ε/D as parameter.

It can be seen that in laminar flow and in turbulent flow with small Reynolds numbers, the roughness has no influence on friction. The tube wall in this range is said "hydraulically smooth". This fact can be visualized as being caused by a situation in which the roughness elements are completely embedded in the laminar sub-layer. Roughness on a pipe wall can disrupt the viscous and thermal sublayers only if it is sufficiently large. As the Reynolds number increases, the viscous sublayer becomes thinner and smaller levels of roughness influence f. The importance of a given level of roughness on friction and heat transfer can be determined by comparing ε to the sublayer thickness (for more details concerning the laminar sublayer in turbulent flow see [43, 29]). The thickness of the laminar sublayer for a constant properties flow is around 30 times $\frac{\mu}{\rho \cdot u^*}$ (where $u^* = \sqrt{\tau_w/\rho}$ is the friction velocity). The roughness Reynolds number is defined:

$$Re_\varepsilon = \frac{\rho u^* \varepsilon}{\mu} = \ldots = Re \frac{\varepsilon}{D} \sqrt{\frac{f}{8}}$$

Experimental data shows that the smooth region (i.e., f depends on Re alone), transitional region (i.e., f depends on both Re and ε/D), and fully rough region (i.e., f depends on ε/D alone) seen in Fig. 3.1 corresponds to the following ranges of Re_ε [29]:

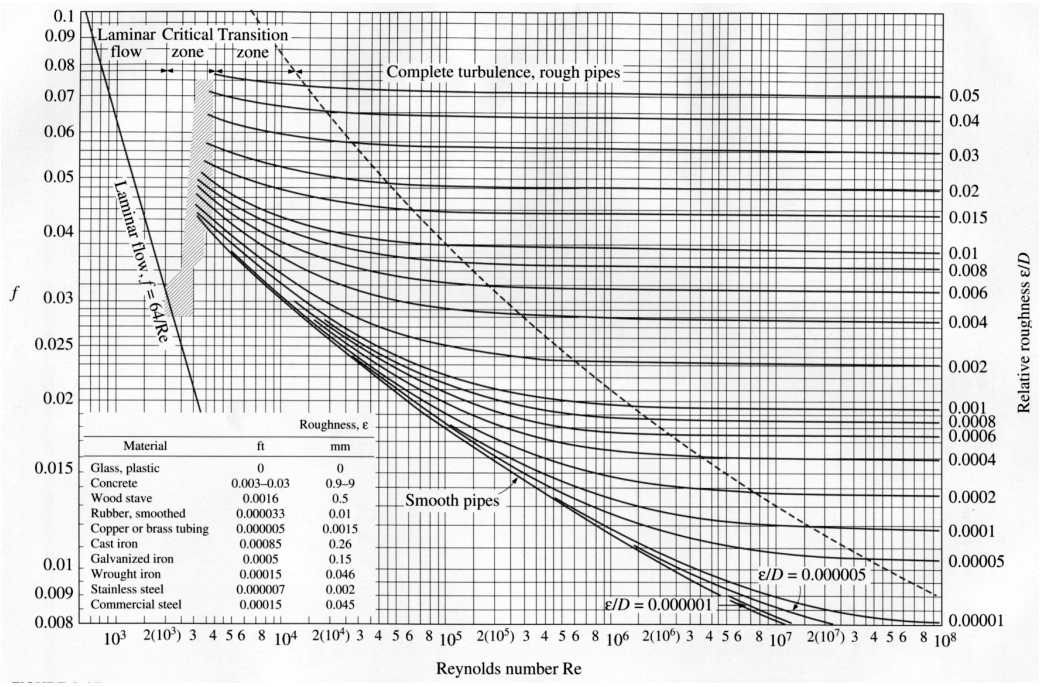

Figure 3.1: The Moody chart for the friction factor for fully developed flow in circular tubes.

$$\begin{cases} & Re_\varepsilon < 5 & \text{hydraulically smooth} \\ 5 \leq & Re_\varepsilon \leq 70 & \text{transitionally rough} \\ 70 < & Re_\varepsilon & \text{fully rough} \end{cases}$$

To evaluate the friction factor for commercially rough pipes the correlation of Colebrook [11] (it is an interpolation fit of the Moody's diagram)

$$\frac{1}{\sqrt{f}} = -2\log_{10}\left(0.27\frac{\varepsilon}{D} + \frac{2.51}{Re\sqrt{f}}\right)$$

can be used in the turbulent range.

In the fully rough regime, Bhatti and Shah [9] provide the following correlation for the local Nusselt number:

$$Nu = \frac{(f/8)\,RePr}{1 + \sqrt{f/8}\left(4.5Re_\varepsilon^{0.2}Pr^{0.5} - 8.48\right)}$$

which applies for the ranges $Re > 10^4$, $0.5 \leq Pr \leq 10$ and $0.002 \leq \frac{\varepsilon}{D} \leq 0.05$.

Since the roughness has the effect of augmenting heat transfer and skin friction, the heat transfer coefficient on a rough wall can be several times that for a

smooth wall at the same Reynolds and Prandtl number. The friction factor, and thus the pressure drop will also be higher. Nevertheless, designers sometimes deliberately roughen tube walls so as to raise h and reduce the surface area needed for heat transfer.

3.4.4 Variable properties

The heat transfer and flow friction solution considered in the previous sections have been based on the assumption that the fluid properties remain constant throughout the flow field. When applied to real heat transfer problems this is obviously an idealization, since the transport properties of most fluids vary with temperature, and thus will vary over the flow cross section of a tube. Constant properties flow is possible only in the case of adiabatic wall and low velocities.

Fluid properties depend mainly on temperature, except in the near-critical and supercritical state where pressure dependence becomes relevant.

The temperature-dependent-property problem is further complicated by the fact that the properties of different fluids behave differently with temperature. For gases, the specific heat varies only slightly with temperature, but the viscosity and thermal conductivity increase as about the 0.8 power of the absolute temperature. Furthermore, the density varies inversely with the first power of the absolute temperature. On the other hand, the Prandtl number does not vary significantly with temperature.

For most liquids the specific heat and thermal conductivity are relatively independent of temperature, but the viscosity decreases very markedly with temperature. This is especially true for oils, but even for water the viscosity is temperature-dependent. The density of liquids, on the other hand, varies little with temperature. The Prandtl number of liquids varies with temperature in much the same manner as viscosity.

For engineering applications it has been found convenient to use the constant-property analytic solutions, or experimental data obtained with small temperature differences, and then to apply some kind of correction to account for properties variation. Fortunately most of the variable-properties results indicate that fairly simple corrections will generally suffice.

In general, one-phase forced-convection heat transfer process for cryogenic coolants may be described by the same scaling parameters as one found useful for other substances

To describe the variable properties effect the correlations proposed by Petukhov [35] have been considered. The analytical heat transfer results that he carried out for air and hydrogen in a smooth-wall pipe with circular cross section can be correlated by the equation:

$$Nu_b = Nu_{b0} \cdot \theta^n \tag{3.11}$$

where

$$n = -\left(a \log_{10} \theta + 0.36\right)$$

and Nu_b and Nu_{b0} are the Nusselt numbers for variable and constant gas properties respectively, evaluated at bulk temperature T_b and $\theta = T_w/T_b$ is the temperature ratio parameter.

For cooling ($T_b/T_w > 1$) , $a = 0$. For heating ($T_b/T_w < 1$), $a = 0.3$. Eq. (3.11) describes the heat transfer with an accuracy of $\pm 4\%$. For simplicity we can take n to be constant for heating also. Then, when $n = -0.47$, Eq. (3.11) describes the analytical results within $\pm 6\%$.

The analytical skin friction results that Petukhov carried out for air and hydrogen in a smooth-wall pipe with circular cross section can be correlated by the equation:

$$f_b = f_{b0} \cdot \theta^m \tag{3.12}$$

where f_b and f_{b0} are the friction factors with variable and constant physical gas properties respectively. It should be noted that, contrary to the case of heat transfer,

$$Re_w^* = Re_w \frac{\rho_w}{\rho_b}$$

greatly affects the friction factor. In fact

$$m = -0.6 + 5.6 \left(Re_w^*\right)^{-0.38}$$

for heating and

$$m = -0.6 + 0.79 \left(Re_w^*\right)^{-0.11}$$

for cooling.

Eq. (3.12) describes the calculated results within $2 - 3\%$. If in Eq. (3.12) m is taking as -0.52 for heating and -0.38 for cooling, this equation describes the calculated data within 7% accuracy.

The analytical calculations by Petukhov for air and hydrogen were made over a range $0.37 - 3.7$ for θ and $10^4 - 10^6$ for Re_w^*.

Literature offers many empirical relations to describe the supercritical hydrogen heat transfer coefficient and friction factor inside regenerative cooling channels [33, 20], but it has been preferred to use Eq. (3.11) and (3.12) since they are based on analytical results and are not characterized by any specific working

conditions. Moreover, since Eq. (3.11) and (3.12) are valid for two strongly different fluids (air and supercritical hydrogen), they could be used for many other substances, such as methane.

3.5 Heat conduction through the wall

Heat is transferred from the hot-gas (subscript *hg*) to the coolant (subscript *co*) via the solid wall, made of internal wall, fins and external wall (Fig. 3.2).

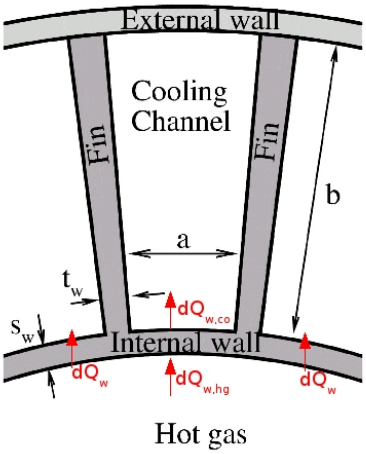

Figure 3.2: Schematic of cooling channels geometry.

The one-dimensional model relies on the heat transfer balance between hot-gas, wall and coolant for steady-state condition. In fact the hot-gas heat transfer rate by convection affects the wall ($dQ_{w,hg}$), is transmitted by conduction through the wall (dQ_w) and is transported by convection to the coolant ($dQ_{w,co}$). For steady-state condition these heat transfer rates must be equal:

$$dQ = dQ_{w,hg} = dQ_w = dQ_{w,co} \tag{3.13}$$

where dQ is the heat transfer rate along the axial distance dx. Neglecting the presence of fins, the terms in the above heat balance equation are:

$$\begin{aligned} dQ_{w,hg} &= q_{w,hg} \cdot 2\pi r \cdot dx \\ dQ_w &= q_w \cdot 2\pi r \cdot dx \\ dQ_{w,co} &= q_{w,co} \cdot 2\pi r \cdot dx \end{aligned} \tag{3.14}$$

where $q_{w,hg}$ is the heat flux by convection from the hot-gas to the wall (see Sec. 3.2), q_w is the heat flux by conduction through the internal wall , $q_{w,co}$ is the heat flux by convection from the wall to the coolant (see Sec. 3.3), and r is the internal radius of the thrust chamber. Note that in the above expression (Eq. (3.14)), the case of no-fins has been considered, since the heat transfer to the coolant flows through the internal wall only. This case is often referred to as "cooling jacket" case.

The heat flux by conduction can be expressed as:

$$q_w = \frac{k_w}{s_w} \left(T_{w,hg} - T_{w,co}\right)$$

where $T_{w,hg}$ and $T_{w,co}$ are the wall temperature at the hot-gas side and coolant side respectively, k_w is the wall thermal conductivity and s_w is the internal wall thickness. This equation represents the analytical solution of the one-dimensional heat conduction in a radial direction and without the effect of the radius, that is, the heat conduction is considered to occur in a one-dimensional manner along a plane wall. The effect of curvature is neglected since the wall thickness s_w is considered small if compared to the nozzle radius r.

The heat transfer balance Eq. (3.14) gives:

$$q_{w,hg} = q_w = q_{w,co}$$

This expression is similar to Eq. (3.13) but with heat fluxes instead of heat transfer rates. This heat flux balance is not realistic because it does not take into account for the enhanced heat transfer due to the presence of the fins.

Using the classic fin analysis [23], the fin effectiveness (ε) is defined as the ratio of the heat flux transferred through the fin to the heat flux that would exist without the fin:

$$\varepsilon = \frac{q_{w\ fin}}{q_{w/o\ fin}}$$

Considering the fin effect, the heat transfer rate from the wall to the coolant becomes:

$$dQ_{w,co} = q_{w,co}\ N\ a\ dx + q_{w,co}\ \epsilon\ N\ t\ dx \tag{3.15}$$

where $q_{w,co}$ is the heat flux at the base of the channel and thus the first part of the above expression represents the heat transfer rate through the channels and the second represents the heat transfer rate through the fins. In particular, N is the number of the channels and t is the thickness of the fin. The trivial relation $2\pi r = N(a + t)$ gives:

$$dQ_{w,co} = q_{w,co}\, 2\pi r\, dx + q_{w,co}\,(\varepsilon - 1)\, N\, t\, dx$$

If the fin is not considered ("cooling jacket" design), $\varepsilon = 1$, and the above expression reduces to Eq. (3.14). The effectiveness ε for a one-dimensional fin with adiabatic tip is:

$$\varepsilon = \sqrt{\frac{2k_w}{h_{co}t}}\, \tanh(mb), \quad \text{where} \quad m = \sqrt{\frac{2h_{co}}{k_w t}}$$

If mb is greater than 2 the fin is considered "tall" and:

$$\varepsilon \simeq \sqrt{\frac{2k_w}{h_{co}t}}$$

Note that due to the fin presence (i.e., due to the non-uniform heat flux distribution along the channel periphery), the coolant energy equation (3.7) must be written as:

$$\rho_{co} u_{co} A\, \frac{dh_{0,co}}{dx} = \frac{dQ_{w,co}}{dx}$$

where $dQ_{w,co}$ is the heat transfer rate that enters the cooling channel.

3.6 High Aspect Ratio Cooling Channels: 1D model

In this section the effect of cooling channel aspect ratio on cooling efficiency will be discussed using the simple one-dimensional model described in the previous sections. The aspect ratio is defined as height to width ratio of a rectangular passages:

$$AR = \frac{b}{a}$$

Past researchers have all found a significant increase in cooling efficiency with high aspect ratio channels (normally defined as such when $AR > 4$ [49]). Today the use of rectangular channels is common practice in the design of regenerative cooling systems.

In particular, increasing the cooling channel aspect ratio, the wall temperature on the hot side of the cooling channels can be reduced by substantially increasing the coolant side surface area relative to the hot-gas side surface through the use of extended surfaces or "fins". Channel aspect ratio can be increased by increasing the number of passages. In turn, the material between them, known as the rib, functionally becomes a fin.

Considering the steady-state heat transfer rates balance Eq. (3.13) in the presence of fin, assuming a generic section where temperatures $T_{aw,hg}$ and T_{co} are known, the wall temperature at the coolant side can be evaluated as:

$$T_{w,co} = \frac{T_{aw,hg} + T_{co}\,\phi}{1+\phi}$$

where

$$\phi = \frac{h_{co}}{h'_{hg}}\,\frac{a+\varepsilon t}{a+t}, \quad \text{and} \quad h'_{hg} = \frac{h_{hg}}{1+\dfrac{h_{hg}}{k_w/s_w}}$$

The hot-gas heat flux $q_{w,hg}$ can be related to the coolant heat flux using Eq. (3.15):

$$q_{w,hg} = q_{w,co}\,\frac{a+\varepsilon t}{a+t}$$

The wall temperatures $T_{w,hg}$ and $T_{w,co}$, such as the heat fluxes $q_{w,hg}$ and $q_{w,co}$ are strongly affected by channel section geometry. Since the effect of the channel aspect ratio on these parameters is not clearly visible on the above expressions, a practical example has been considered. The throat section of the European rocket engine (Vulcain) has been taken as a guideline for an engine dimensioning. The Vulcain engine is a LO_2/LH_2 cryogenic engine propelling $1100\ kN$ and having a regenerative system for the thrust chamber cooling. The main parameters of the selected throat section are:

r	$0.130\ m$
b	$0.010\ m$
s_w	$0.001\ m$

The total cross sectional area of cooling channels and fins is $A_{tot} = 2\pi r\ b = 0.0082\ m^2$. This cross sectional area is divided into the cooling channels area ($A_{co} = N\ a\ b = 0.0058\ m^2$) and the fins area ($A_{fin} = N\ t_w\ b = 0.0024\ m^2$). Increasing the number N of cooling channels (considering A_{co} and A_{fin} as constants), the channel aspect ratio necessarily increases while the quantity of wall material remains constant (i.e., the weight of the engine is fixed). The hydrogen thermodynamic conditions in the cooling channel are $p_{co} = 130\ bar$ and $T_{co} = 70\ K$ and its mass flow rate per unit area is $\rho_{co}u_{co} = 8500\ kg/m^2\ s$. The coolant heat transfer coefficient has been evaluated using the semi-empirical relation $Nu_{co} = 0.011\ Re_{co}^{0.8} Pr_{co}^{0.4}$ where the Nusselt number Nu_{co} and the Reynolds number Re_{co} are based on the hydraulic diameter (see Sec. 3.4 for more details):

$$D_h = \frac{4A}{P_w}$$

where $A = a\ b$ is the cross sectional area of a rectangular cooling channel and $P_w = 2(a + b)$ is its perimeter. Note that the above semi-empirical equation is the classical Dittus-Boelter [12] correlation $Nu = 0.023\ Re^{0.8} Pr^{0.4}$ in which the coefficient 0.023 has been reduced to 0.011 in order to take into account the variable property effect (see Eq. 3.11) with the sample value $T_w/T \sim 5$.

The hot-gas heat transfer rate $h_{hg} = 26000\ W/m^2\ K$ has been considered for the throat section. This value has been chosen via Eq. (3.1), considering a heat flux $q_{w,hg} = 70\ MW/m^2$, a wall temperature $T_{w,hg} = 750\ K$ and an adiabatic wall temperature $T_{aw,hg} = 3450\ K$. These values represent the typical operating conditions of the Vulcain engine at the throat section [14]. Finally, the wall thermal conductivity of copper alloy ($k_w = 390\ W/m\ K$) has been selected.

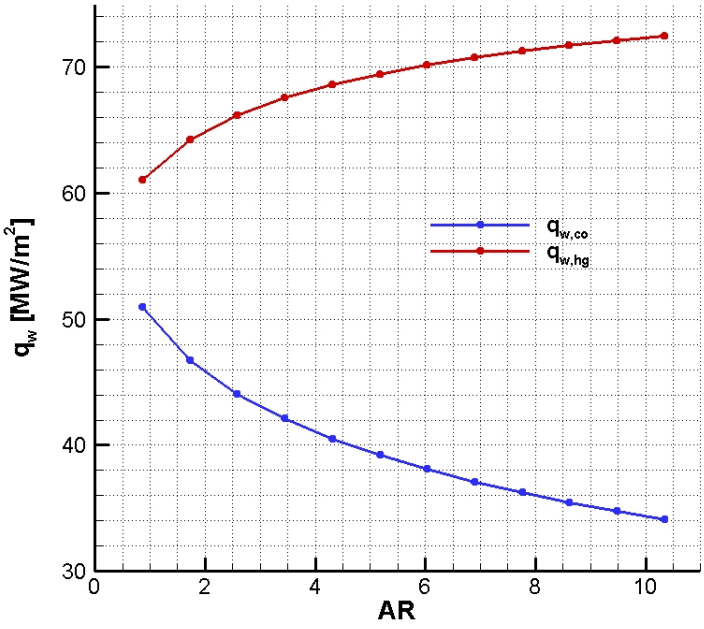

Figure 3.3: Wall heat transfer vs channel AR.

In Fig. 3.3 and Fig. 3.4 the effect of the aspect ratio on the wall heat flux and wall temperature is clearly visible: the hot-gas side wall heat flux q_{hg} increases as the aspect ratio increases while the heat flux at the base of the channel q_{co} strongly

decreases. This opposite behaviour is not erroneous: since the wall heat transfer is transmitted to the coolant through the channel base and fin, increasing the number of fins the heat flux distribution between the channel base and the fin changes and thus the channel base is less affected by heat flux. As a consequence the coolant is heated in a more efficient way because the wall heat flux is better distributed along the coolant perimeter. This implies that the entire mass flow rate of the coolant flow is heated, increasing the cooling efficiency. On the contrary, in the case of low aspect ratio, cooling efficiency is poor because only a part of the coolant mass flow rate (close to the channel base) is affected by heat transfer while the rest is not.

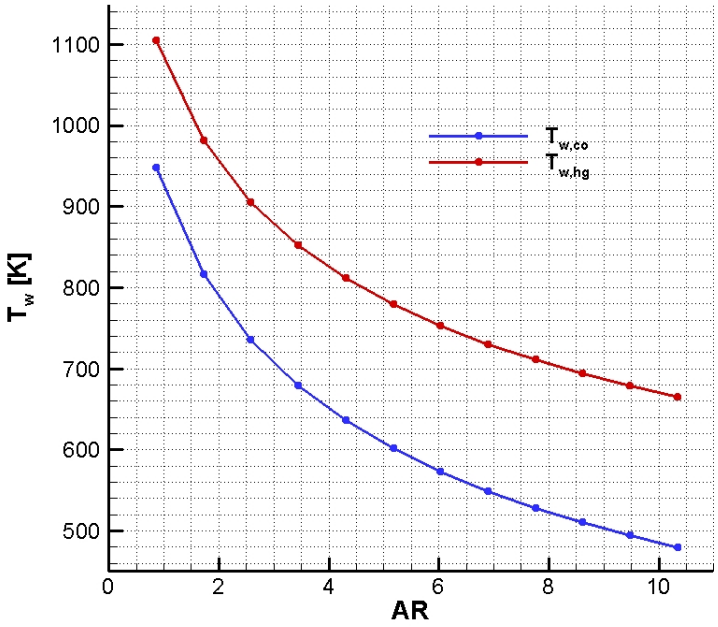

Figure 3.4: Wall temperature vs channel AR.

Regarding wall temperature, Fig. 3.4 shows that, as wall heat flux $q_{w,hg}$ increases with aspect ratio, the wall temperature decreases. This effect on wall temperature is very sensitive: wall temperature can be reduced of $300\ K$ as the aspect ratio changes from 2 to 8.

Having in mind Fig. 3.3 and Fig. 3.4 it seems that the increase of channel aspect ratio has no drawbacks and the greater is the channel aspect ratio the better is the cooling efficiency in terms of wall temperature and coolant warming.

As a matter of fact there is an optimum aspect ratio since coolant pressure loss is strongly affected by channel aspect ratio. Using the simple one-dimensional model for the coolant flow in channel, the pressure loss can be expressed as (see Eq. 3.7):

$$dp_{co} = \frac{1}{2}\rho_{co}u_{co}^2 \frac{f_{co}}{D_h}dx$$

where f_{co} is the wall friction factor and it is a weak decreasing function of the Reynolds number (see Sec. 3.4 for more details). The effect of the aspect ratio on pressure loss is clearly visible on Fig. 3.5.

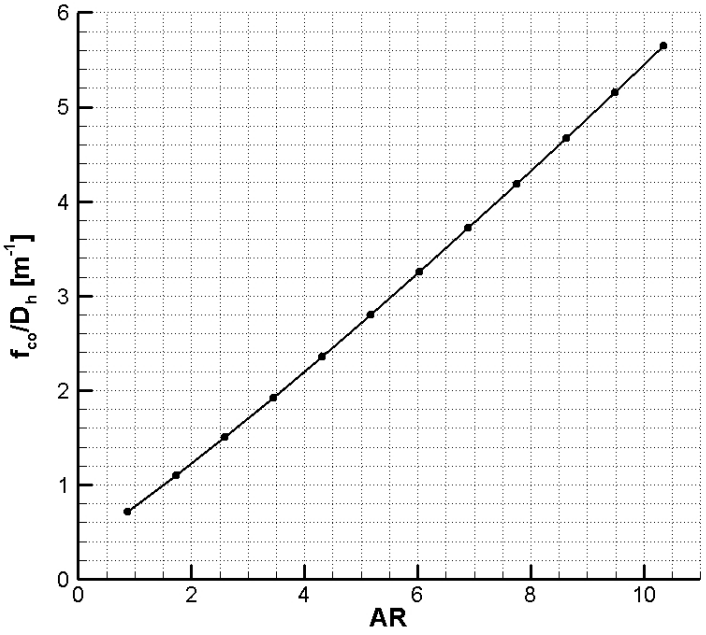

Figure 3.5: Pressure loss vs channel AR.

The pressure loss behaviour of Fig. 3.5 is due to the different area to perimeter distribution of the cooling channel as the aspect ratio changes. In fact, as the number of channels increases (i.e., increase of the channel aspect ratio), the total cross sectional area of the coolant flow remains unchanged while the total channel perimeter increases thus generating greater pressure loss. Pressure loss can augment as much as five times as aspect ratio changes from 2 to 8. Since a good design of an engine must take into account both wall thermal behaviour and re-

quested pump power (i.e., coolant pressure drop), an optimum aspect ratio must be found. This optimum aspect ratio depends on the engine cycle type (expander cycle, gas generator cycle, preburner cycle, etc.) and on the operating conditions of the engine (combustion chamber and coolant manifold conditions). In particular, it is a crucial design parameter for an expander cycle engines since the coolant warming (high AR demand) provides the available power for turbopump (low AR demand).

Chapter 4

“Quasi 2D” stratification model

The objective of this chapter is to propose and provide a computational tool for the description of the wall and coolant behaviour that occurs in regeneratively-cooled rocket engines in the case of high aspect ratio cooling channel (HARCC). As already seen in Chap. 3, numerical tools able to describe the thermal behaviour of regenerative cooling system are generally based on one-dimensional models relying on semi-empirical relationships. One of the main drawbacks of conventional one-dimensional calculation methods is that an ideal mixing of the thermal energy into the coolant channel cross section is assumed. This implies that when a significant radial thermal stratification takes place, like in the case of HARCC, a significant error arises [49]. The objective of this chapter is to overcome the above limitation of simplified approaches by developing a computational tool able to describe the coupled hot-gas/wall/coolant environment that occurs in most liquid rocket engines and to provide a quick and reliable prediction of thermal stratification phenomena in cooling channels. This approach, which is an extension of that presented by Woschnak and Oschwald [53], is still widely relying on empirical relationships. Nevertheless, it allows to compute the radial stratification of both the wall and the coolant flow temperatures. This result is obtained by considering the one-dimensional steady-state evolution of the hot-gas flow as already seen in Sec. 3.2, and a “quasi 2-D” flow evolution through the cooling channels. The basic idea of the “quasi 2D” model is to consider the one-dimensional approach for the coolant mass and momentum equation (as already seen in Sec. 3.3 while coolant and wall energy equations depend on the radial direction too. This permits to describe the strong temperature stratification that occurs in case of HARCC. As in the case of one-dimensional model, steady-state condition is assumed and thus hot-gas, wall, and coolant behaviours are coupled by heat balance from hot-gas to wall and from wall to coolant. The approach is developed for any fluid evolving through cooling channels, by considering any equation of state, and thus compressible gas, supercritical fluid and liquid can be considered as coolants.

4.1 Heat conduction through the wall

Heat is transferred from the hot-gas to the coolant via the solid wall, made of internal wall, fins and external wall (Fig. 4.1). If steady-state operation is assumed, the heat flux entering the internal wall $q_{w,hg}$ (see Sec. 3.2) must be equal to that leaving it, and a simple steady-state wall heat transfer balance can be written:

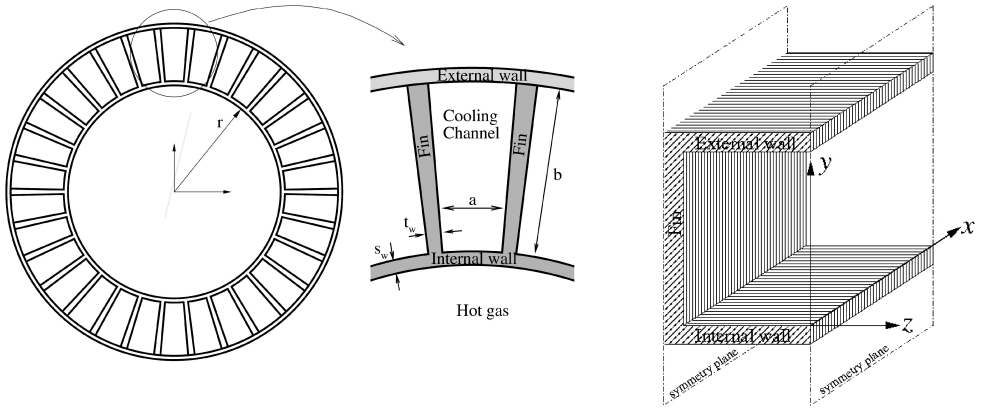

Figure 4.1: Schematic of cooling channels geometry.

$$q_{w,hg} = \frac{k_w}{s_w} \ (T_{w,hg} - T_{w,co}) \tag{4.1}$$

where k_w and s_w are the wall thermal conductivity and thickness, respectively, and $T_{w,co}$ is the coolant-side wall temperature. Note that a one-dimensional radial heat transfer through the internal wall of thickness s_w has been considered. Then, the heat transfer balance through the fins is computed by assuming again steady-state operation:

$$\frac{\partial}{\partial y}\left(k_w t_w \frac{\partial T_w}{\partial y}\right) = 2q_w \tag{4.2}$$

where y is the radial direction, t_w is the fin thickness, T_w is the wall temperature and q_w is the heat flux from the fin to the coolant. This equation assumes one-dimensional heat transfer in the radial direction, a non uniform fluid temperature, a fin thickness that is much smaller than its axial length, and infinitely tall fin. For an actual "fin" in this type of cooling channel the infinite height assumption is approximately valid because the tip is nearly adiabatic in most cases. The boundary conditions at the bottom ($y = 0$) of the fin is, according to (4.1):

$$q_{w,hg} = -k_w \left. \frac{\partial T_w}{\partial y} \right|_{y=0} \tag{4.3}$$

which means that the radial heat flux entering the fin balances with that entering the wall from the hot-gas side ($q_{w,hg}$). At the top ($y = b$) of the fin the boundary condition is:

$$0 = -k_w \left. \frac{\partial T_w}{\partial y} \right|_{y=b} \tag{4.4}$$

which is the adiabatic condition, that is, the external wall is assumed adiabatic.

Note that in the wall balance equation (4.1) the heat flux from the hot-gas $q_{w,hg}$ is, as a matter of fact, a function of the unknown variable $T_{w,hg}$, since the hot-gas flow properties are completely evaluated by the one-dimensional isentropic expansion law (see Sec. 3.2).

4.2 Coolant flow

The cooling channel flow model is developed by using the steady-state conservation laws of mass, momentum, and energy, taking into accounts the effects of heat transfer and friction. As mentioned above a "quasi 2-D" flow model is assumed for the coolant flow. This model considers a one-dimensional evolution for the velocity $u = u(x)$ (the only component of velocity considered is the axial one) and the pressure $p = p(x)$, whereas temperature is left to vary also in radial direction: $T = T(x, y)$. The other thermodynamic variables are obtained by suitable equations of state (EOS), which are written in the general form:

$$p = F_p(\rho, T) \quad \text{and} \quad h = F_h(\rho, T) \tag{4.5}$$

The coolant flow governing equations are thus written on the basis of the above model.

Coolant mass equation

The steady-state integral mass conservation equation through the channel cross sections is:

$$\frac{d}{dx} \iint_A \rho u dA = 0$$

where ρ is the coolant density, A is the cross section area and x is the axial direction. Considering the "quasi 2-D" flow model the mass conservation becomes:

$$\overline{\rho}\, u\, A = \dot{m} \tag{4.6}$$

where

$$\overline{\rho} = \frac{1}{A}\iint_A \rho dA \tag{4.7}$$

is the average coolant density through the channel cross section and $\dot{m}$ is the mass flow rate.

Coolant momentum equation

The steady-state integral momentum equation through the channel cross sections is:

$$\frac{d}{dx}\left[\iint_A \left(\rho u^2 + p\right) dA\right] dx - p\frac{dA}{dx}dx = -\iint_{S_w} \tau_w dS_w$$

where the left part of the equation represents the momentum flux and the axial component of the pressure force acting on the surface of the channel, while the right part is the integral skin friction force acting on the channel surface (S_w). Considering the mass equation (4.6-4.7) and the "quasi 2-D" flow model (p and u are uniform through the channel cross section), the momentum equation becomes:

$$\left(\dot{m}\frac{du}{dx} + A\frac{dp}{dx}\right) dx = -\iint_{S_w} \tau_w dS \tag{4.8}$$

where the shear stress τ_w can be related to flow variables by the skin friction factor f:

$$\tau_w = \frac{1}{8}\overline{\rho}u^2 f$$

The skin factor f is estimated using a proper empirical correlation (see Sec. 3.4).

Coolant energy equation

The steady-state integral energy equation through the channel cross sections is:

$$\frac{d}{dx}\left[\iint_A \left(\rho u h_0\right) dA\right] dx = \iint_{S_w} q_w dS_w \tag{4.9}$$

where h_0 is the stagnation enthalpy ($h_0 = h + u^2/2$), and q_w is the heat flux entering in the coolant through the wall S_w. This is the equation used in the one-dimensional approach. In the present approach, as the temperature is left to

vary in the radial direction, some equation suitable to the evaluation of T must be found. As thermal stratification depends on the heat flux through the fluid in radial direction and on the heat flux exchanged with the channel walls, the hypothesis is made of splitting the height of the channel in tiny slices of height dy, all having, at the same abscissa x, the same values of u and p. To solve for $T(y)$, the balance equation (4.9) has to be written for a slice of height dy rather than for the whole channel height (see Fig. 4.2):

$$\frac{d}{dx}\Big[\rho u h_0 a(y) dy\Big] dx = 2q_w(y)dydx + q_c(y)a(y)dx - q_c(y+dy)a(y)dx \quad (4.10)$$

where only the dependency of variables on y has been emphasized, because all variables depend on x.

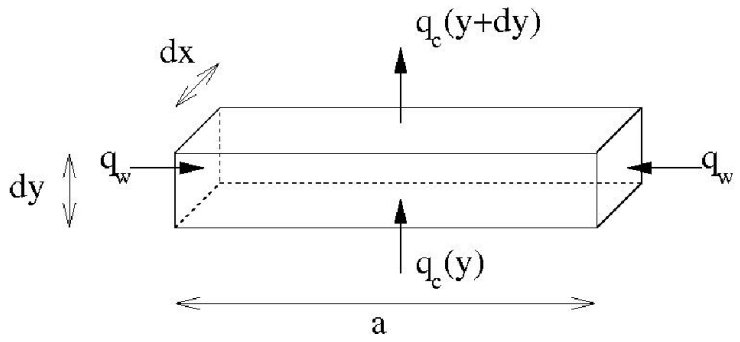

Figure 4.2: Heat fluxes in a slice of cooling channel of width a and height dy.

The equation (4.10) becomes a differential equation for T if it is possible to express $q_w(y)$ and $q_c(y)$ as a function of $T(y)$. As regards to $q_c(y)$, this can be made according to Kacynski [24]. If it is assumed that $q_c(y)$ is due to the turbulent mixing:

$$q_c(y) = -k_t \frac{\partial T}{\partial y}$$

where k_t is the average turbulent conductivity in the radial direction, which can be obtained as a function of the Reynolds number Re and of the fluid thermal conductivity k. For instance in case of hydrogen k_t can be expressed as:

$$\frac{k_t}{k} = 0.008\ Re^{0.9}$$

With this hypothesis (4.10) becomes:

$$\frac{\partial}{\partial x}\left(\rho h_0 u a\right) = \frac{\partial}{\partial y}\left(k_t a \frac{\partial T}{\partial y}\right) + 2q_w \quad (4.11)$$

Finally the wall heat flux can be related to the coolant and wall temperature using a transfer coefficient form (see Sec. 3.6):

$$q_w = h\,(T_w - T)$$

where h is the heat transfer coefficient and T_w is the wall temperature. The coefficient h is estimated using a proper empirical correlation (see Sec. 3.4). Note that, since we are considering thermal stratification in the radial direction, h is a function of the abscissa y and thus its value is estimated for each radial abscissa by means of a proper semi-empirical correlation of the form (see Sec. 3.4):

$$Nu = Nu\left(Re, Pr, \frac{\varepsilon}{D_h}, \frac{T_w}{T}\right)$$

In particular, $\frac{T_w}{T}$ is the local value at the abscissa y while Nu, Re, and Pr are evaluated using their average value in the channel cross section and the hydraulic diameter D_h of the channel cross section is considered as the reference length.

The boundary conditions at the bottom and at the top of the cooling channel are:

$$q_{w,hg} = -k_t \left.\frac{\partial T}{\partial y}\right|_{y=0} \qquad \text{and} \qquad 0 = -k_t \left.\frac{\partial T}{\partial y}\right|_{y=b} \tag{4.12}$$

which are the same as those (4.3-4.4) used for the fin and are therefore consistent with the hypothesis of axisymmetric temperature distribution on the internal and external walls. The conditions (4.12) state that the heat flux $q_{w,hg}$ enters at the channel bottom and that the channel top is adiabatic.

4.3 Computational strategy

The governing equations can be discretized considering a 2D grid: M nodes ($i = 1, ..., M$) for the axial discretization and N nodes ($j = 1, ..., N$) for the radial discretization. The computations proceed starting from the entrance of the coolant at the manifold and moving along the axial direction. The solution at each axial position is computed iteratively from that at the previous one.

To simplify the calculations, the empirical coefficients f_{co} and h_{co} (the subscript *co* means coolant) are evaluated at the previous axial position. This is a minor hypothesis since the variation of the empirical coefficients between contiguous axial positions is negligible.

Moreover, the EOS equation has been linearized around the actual value of the density ρ_{co} and temperature T_{co}.

Using this hypothesis the governing equations are written for each value of i, assuming known the solution at the previous axial position ($i-1$, or the channel inlet condition). The overall system of equations can be divided into two groups:

- 3N linear equations: coolant energy (4.11), fin (4.2), EOS (4.5) with respect to the variables T_{co}^j, T_w^j and ρ_{co}^j ($j = 1, ..., N$);
- 3 non-linear equations: coolant mass (4.6) and momentum (4.8), wall balance (4.1), with respect to the variables u_{co}, p_{co}, and $T_{w,hg}$.

To solve the system of equations, the following computation strategy is used at each axial station:

1. A first tentative value for $u_{co}, p_{co}, T_{w,hg}$ is chosen: these values are taken from the previous axial station;
2. The 3N linear equations system, considering having $u_{co}, p_{co}, T_{w,hg}$ as parameters, is solved for $T_{co}^j, T_w^j, \rho_{co}^j$;
3. The 3 non-linear equations system is solved for a new value of $u_{co}, p_{co}, T_{w,hg}$, considering $T_{co}^j, T_w^j, \rho_{co}^j$ as parameter;
4. The new value of $u_{co}, p_{co}, T_{w,hg}$ is used for step 2 and the procedure is repeated until these values remain unchanged.

Note that the equations of state have been considered linear equations because at each iteration step they are linearized around the sought solution.

4.4 Validation and results: hydrogen test case

The validation of the described numerical tool is made with respect to the test cases presented by Le Bail and Popp [28], where the coolant flow in the regenerative channels is computed using a numerical solver for the parabolized Navier Stokes equations; turbulence has been modeled by an algebraic model which accounts for wall roughness effects too. This is one of the few papers in the literature in which some data of a regeneratively cooled engine have been published. The test cases address the regenerative cooling of the thrust chamber of Vulcain engine, with two different channel geometries. The main properties of the flow and the main features of the nozzle and cooling channels are reported in Table 4.1, whereas more details can be found in the reference paper [28].

propellants	LO_2-LH_2
chamber pressure	100 bar
chamber mixture ratio	$O/F = 5.9$
coolant	H_2
inlet coolant temperature	48.7 K
inlet coolant pressure	137.9 bar
maximum channel aspect ratio for case A	AR_{max} =8.5
maximum channel aspect ratio for case B	AR_{max} =7
wall roughness	ϵ =5μm

Table 4.1: Data for the test case of Le Bail and Popp [28].

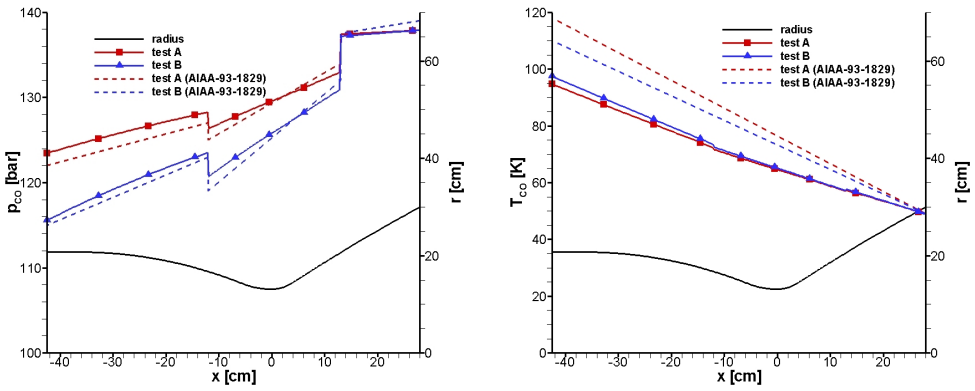

Figure 4.3: Coolant pressure (left) and coolant temperature (right) for test cases A and B.

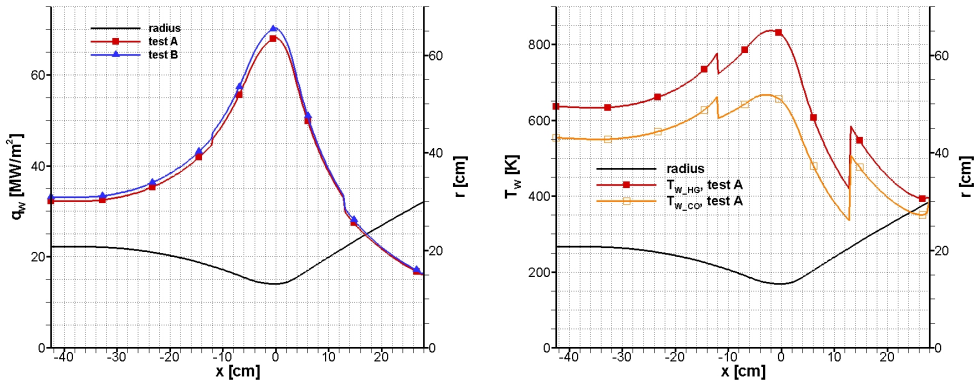

Figure 4.4: Wall heat flux (left) and wall temperatures (right) for test cases A and B.

The coolant flows in the opposite direction with respect to hot-gas and cooling channels are divided into three sections of constant height (width varies according to the nozzle radius). Test case B is different from test case A only because channels have 15% lower height.

The computations of test cases A and B carried out with the present model have been obtained by including classical correlations for the skin friction factor (f_{co}) and heat transfer coefficient (h_{co}). In particular, Petukhov's correction of Colebrook equation is used for the skin friction factor [35] and Bhatti-Shah expression, again with Petukhov's correction accounting for the variable temperature across the channel section, is used for the heat transfer coefficient [35, 9] (see Sec. 3.4).

The results obtained with the present model for test cases A and B are displayed in Fig. 4.3 and 4.4. Fig. 4.3 shows coolant pressure (left) and coolant average temperature (right), compared with the data published in [28] while Fig. 4.4 shows wall heat flux (left) and wall temperature (right) at the hot-gas side and coolant side for test case A only. The behaviour of coolant pressure shows a good agreement with the reference results in both test cases. Note that the pressure loss is 14 bar for test A and 22 bar for test B. The behaviour of coolant average temperature shows a larger discrepancy. This is due to the different input data: LeBail and Popp [28] used the wall heat flux as an input while in the present computations wall heat flux is an output obtained via the wall energy balance. The wall heat transfer imposed in the reference 3D-computations has a peak of $60\ \mathrm{MW/m^2}$ at the throat while a value of $70\ \mathrm{MW/m^2}$ has been obtained here. This heat flux mismatch leads to a difference of 20% in coolant exit temperature between present

and published data [28]. Regarding wall temperature, its value has a maximum at the nozzle throat due to the peak value of heat transfer coefficient in that location (see Eq. (3.3). Moreover, due to the high heat flux value, the temperature difference in the internal wall can be as high as $170\ K$; as a consequence the maximum wall temperature at the coolan-side is $660\ K$. Internal wall made of high-conductivity material (such as copper alloy) and with low thickness ($1\ mm$ in this test case) is due to the necessity of reducing wall temperature differences. In fact, in case of strong differences, material is prone to high thermal stresses which could result in a structural failure.

Besides to the average evolution of variables along the cooling channels the present models provides the prediction of thermal stratification of coolant and fin. The results obtained for test case A are shown in Fig. 4.5-4.6. In particular, Fig. 4.5 shows the evolution, along the channel of thermal stratification. It can be noticed that a significant stratification takes place in the present test case, especially at the channel exit. An example of cooling channel and fin width and thermal stratification is shown in Fig. 4.6. The solutions are referred to channel throat and exit.

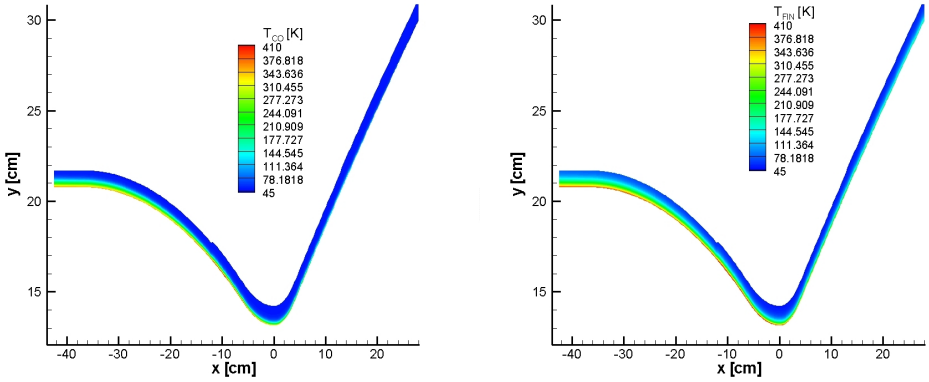

Figure 4.5: Coolant (left) and fin (right) temperature stratification for test case A.

The results show reasonable agreement with data published in the literature. In fact, it has to be considered that input data are slightly different and that the model relies on empirical relationships for skin friction factor, heat transfer coefficient, and turbulent thermal conductivity. The accuracy of the predictions is strongly dependent on the accuracy of these relationships.

A possible way to improve the knowledge of this relation and to use correctly the model presented in this chapter is to validate empirical models on simple channel flows by fully 3D Navier-Stokes simulations and then use the model for the

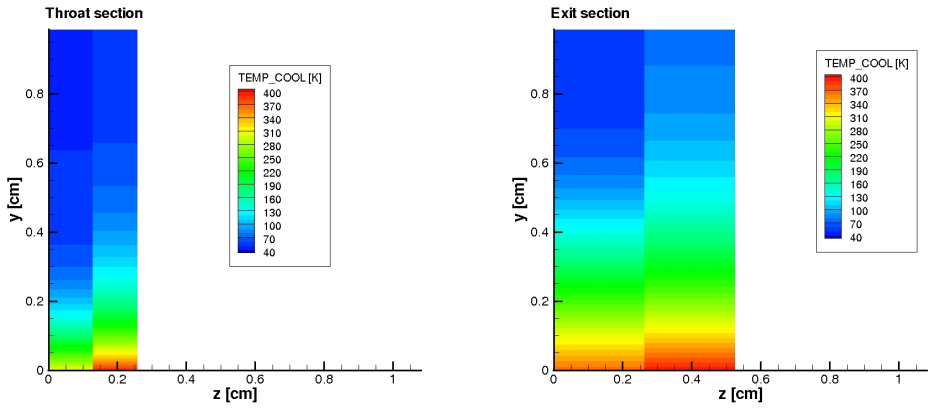

Figure 4.6: Coolant and fin temperature stratification at throat (left) and exit (right) section for test case A.

full length of cooling channels and/or in optimization programs.

4.5 Results: methane test case

The present tool has been used to evaluate the heat transfer in a LO_2/methane rocket engine. Since methane engines are a new trend for aerospace applications (see Sec. 2.5.1), no experimental data have been published yet. For that reason, an example test has been carried out on the Vulcain engine with the only goal of comparing, on a quality level, the cooling efficiency of methane with respect to hydrogen.

The cooling channels geometry is the same presented in [28] with AR_{max} =8.5 and the main properties of the flow and the main features of the nozzle and cooling circuit are reported in Table 4.2.

Note that, while pressure conditions (chamber and cooling channels inlet), geometry and wall roughness are the same of the hydrogen test case, chamber mixture ratio and cooling chamber inlet temperature differ from the hydrogen case to better reproduce methane operative conditions. Moreover, for both test cases, the entire fuel mass flow rate has been used in the cooling circuit: 33 kg/s in the hydrogen case and 70 kg/s in the methane case.

In Fig. 4.7 wall heat transfer and wall temperature (on hot-gas side and on coolant side) along the axis are shown. As expected, using the same Vulcain chamber and channel geometry, methane is a less efficient coolant with respect to hydrogen. In fact, in case of methane, the wall heat flux is lower (q_{max} =

propellants	LO_2-LCH_4
chamber pressure	100 bar
chamber mixture ratio	$O/F = 3$
coolant	CH_4
inlet coolant temperature	190.6 K
inlet coolant pressure	137.9 bar
maximum channel aspect ratio	AR_{max} =8.5
wall roughness	ϵ =5μm

Table 4.2: Data for the methane test case.

70 MW/m^2 in the case of hydrogen and $q_{max} = 47\ MW/m^2$ in the case of methane) and hence the wall temperature is higher.

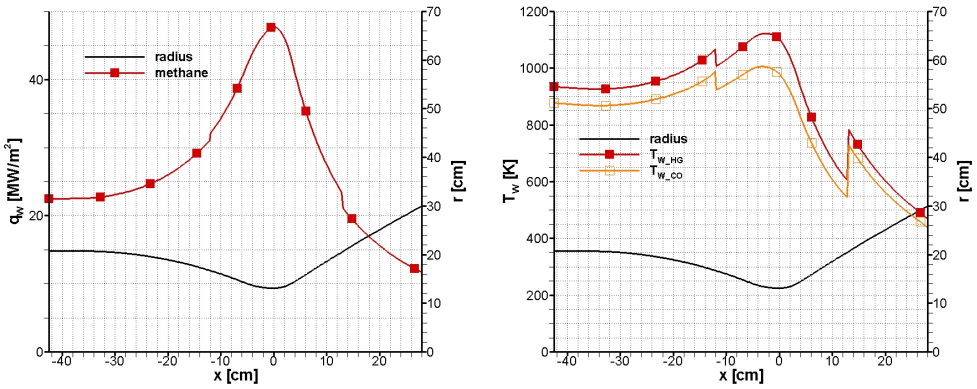

Figure 4.7: Wall heat flux (left) and wall temperatures (right) for methane test case.

Coolant and fin temperature stratification at the inlet, throat, and exit sections are shown in Fig. 4.8, Fig. 4.9, and Fig. 4.10 respectively. As expected, the high aspect-ratio cooling channel geometry induces an evident thermal stratification even in the case of methane. Temperature stratification becomes more relevant as the coolant moves from the inlet section to the exit section. However, in the last section the upper part of methane is not yet heated; this means that only a part of the fluid has been effectively used as a coolant. A good design should minimize this inefficiency by proper selection of channel and fin dimensions.

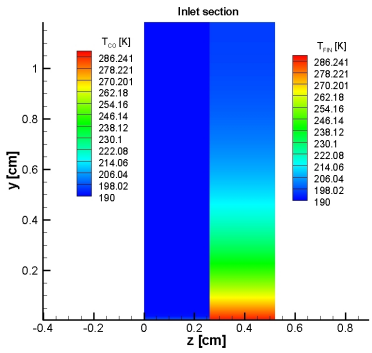

Figure 4.8: Coolant and fin temperature stratification at inlet section for methane test case.

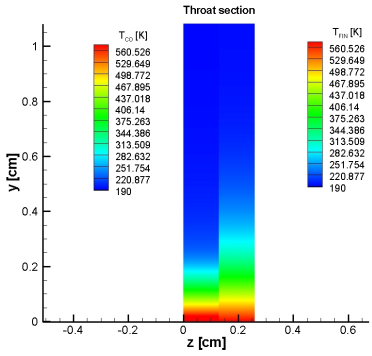

Figure 4.9: Coolant and fin temperature stratification at throat section for methane test case.

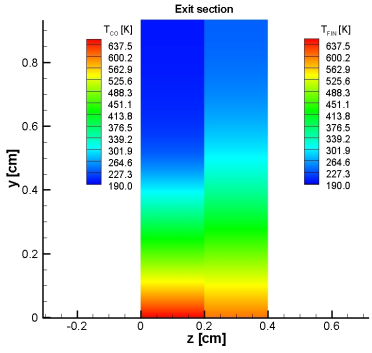

Figure 4.10: Coolant and fin temperature stratification at exit section for methane test case.

Chapter 5

Numerical method

In this chapter we want to introduce a CFD tool to simulate the three-dimensional coolant flow inside cooling channels. In particular, this tool must be able to describe the turbulent flow of a generic fluid, since the coolant thermodynamic characterization is not straightforward. In fact coolant thermodynamics must be modeled by proper equation of state (see Chap. 2) far from the equations of state implemented in standard CFD tool (that is, perfect gas or perfect liquid equation of state). However, the flow of a generic fluid is described by classical governing equations, that are, mass, momentum and energy equations (Sec. 5.1 and 5.2). The fluid characterization does not affect the general treatment of the governing equations since these principles describe the mechanical and thermal behaviour of a generic moving fluid; for that reason an home-made finite volume numerical tool (Sec. 5.3 and Ref. [16]) able to describe perfect gas flow has been acquired and modified in order to simulate a generic fluid flow (i.e., the prefect gas assumption has been removed). Many modifications have been carried out, mainly the Riemann Problem solver (Sec. 5.4) and the boundary conditions treatment (Sec. 5.5). In the present code the generic fluid thermodynamic characterization is performed by means of a database (Sec. 5.6) so that the evaluation of fluid properties is independent from the complexity of the selected equation of state. Finally (Sec. 5.7) the Spalart-Allmaras turbulence model is presented. This one-equation eddy-viscosity model has been easily integrated in the CFD tool since, as a matter of fact, it is an extra governing equation that can be discretized using the finite volume approach.

5.1 Governing equations

A finite volume numerical scheme solves the governing equations written in a general integral form. Using the integral formulation, the governing equations are

often referred to as "conservation laws". This form of the governing equations derives directly from the physical principles that describe the behaviour of a moving fluid:

- conservation of mass
- momentum balance
- conservation of energy

The conservation laws are applied to a fluid element which is a small "blob" of fluid that contains the same material at all times as the fluid moves. This fluid element, often called material element, defines a control volume $\mathcal{V}$ and a control surface $\mathcal{S}$. Since the fluid element deforms as it moves, its volume and surface change shape and position and thus they are functions of time: $\mathcal{V} = \mathcal{V}(t)$, $\mathcal{S} = \mathcal{S}(t)$. In what follows the conservation laws for a one-phase inert flow will be presented and discussed.

Conservation of mass

The conservation of mass principle states that the total amount of mass of a fluid element does not change in time t, that is:

$$\frac{d}{dt}\int_{\mathcal{V}(t)} \rho \, d\mathcal{V} = 0$$

where ρ is the density of the fluid.

Momentum balance

The momentum balance principle states that the momentum variation in time of a fluid element is equal to the total force acting on the volume $\mathcal{V}$ and on the surface $\mathcal{S}$, that is:

$$\frac{d}{dt}\int_{\mathcal{V}(t)} \rho \, \boldsymbol{u} \, d\mathcal{V} = \int_{\mathcal{V}(t)} \rho \, \boldsymbol{f} \, d\mathcal{V} + \oint_{\mathcal{S}(t)} \boldsymbol{t} \, d\mathcal{S} \tag{5.1}$$

where $\boldsymbol{u}$ is the velocity vector and $\rho\boldsymbol{u}$ is the fluid momentum per unit volume. The first term on the right side represents the sum of the forces acting on the volume $\mathcal{V}$ ($\boldsymbol{f}$ is the volumetric force per unit mass) while the second term is the sum of the forces acting on the external surface $\mathcal{S}$ ($\boldsymbol{t}$ is the surface force per unit area).

The i-th component of vector $\boldsymbol{t}$ can be expressed as a function of the stress tensor σ_{ij}:

$$t_i = \sigma_{ij}\, n_j$$

where n_j is the j-th component of the vector $\boldsymbol{n}$, that is the unit vector orthogonal to the surface $\mathcal{S}$ and it is considered positive as it is outward-facing the volume $\mathcal{V}$. The stress tensor can be decomposed into two parts: the spherical tensor (based on the pressure p) and the viscous stress tensor τ_{ij}:

$$\sigma_{ij} = -p\, \delta_{ij} + \tau_{ij} \tag{5.2}$$

where $\delta_{ij} = 0$ if $i \neq j$ and $\delta_{ij} = 1$ if $i = j$. In case of Newtonian fluid, the viscous stress tensor can be expressed by:

$$\tau_{ij} = \mu \left(\frac{\partial u_i}{\partial x_j} + \frac{\partial u_j}{\partial x_i} \right) + \lambda \frac{\partial u_k}{\partial x_k} \delta_{ij} \tag{5.3}$$

where u_i is the i-th component of the velocity $\boldsymbol{u}$, x_i is the i-th orthogonal axis, μ is the dynamic viscosity and λ is the second viscosity coefficient. Assuming the Stokes hypothesis, the two viscosity coefficients can be related by:

$$3\lambda + 2\mu = 0$$

Finally Eq. (5.1) becomes:

$$\frac{d}{dt} \int_{\mathcal{V}(t)} \rho\, u_i\, d\mathcal{V} + \oint_{\mathcal{S}(t)} p\, n_j\, \delta_{ij}\, d\mathcal{S} = \int_{\mathcal{V}(t)} \rho\, f_i\, d\mathcal{V} + \oint_{\mathcal{S}(t)} \tau_{ij}\, n_j\, d\mathcal{S}$$

Note that in this thesis the Newtonian fluid hypothesis is always considered valid.

Conservation of energy

The conservation of energy principle states that the total energy variation in time of a fluid element is equal to the heat transfer rate entering through the surface $\mathcal{S}$ and the total work made by the forces acting on the volume $\mathcal{V}$ and on the surface $\mathcal{S}$, that is:

$$\frac{d}{dt} \int_{\mathcal{V}(t)} \left(e + \frac{1}{2} u_j\, u_j \right) \rho\, d\mathcal{V} = \int_{\mathcal{V}(t)} \rho\, f_j\, u_j\, d\mathcal{V} + \oint_{\mathcal{S}(t)} t_i\, u_i\, d\mathcal{S} - \oint_{\mathcal{S}(t)} q_j\, n_j\, d\mathcal{S} \tag{5.4}$$

where the total energy per unit volume is: $E = \rho \left(e + \frac{1}{2} u_j\, u_j \right)$; e is the specific internal energy and $\boldsymbol{q}$ is the vector of heat flux, considered positive as it is outward-facing the volume $\mathcal{V}$. Note that the total energy is composed by internal energy

and kinetic energy only, since no other types of energy affect the flow that we intend to investigate.

The heat flux, using the Fourier's law, can be related to the temperature gradient by:

$$q_j = -k\frac{\partial T}{\partial x_j} \tag{5.5}$$

where k is the thermal conductivity of the fluid. Finally, using the stress tensor definition (Eq. (5.2)), Eq. (5.4) can be written as:

$$\frac{d}{dt}\int_{\mathcal{V}(t)} E\, d\mathcal{V} + \oint_{\mathcal{S}(t)} p\, u_j\, n_j\, d\mathcal{S} = \int_{\mathcal{V}(t)} \rho\, f_j\, u_j\, d\mathcal{V} + \oint_{\mathcal{S}(t)} (\tau_{ij}\, u_i - q_j)\; n_j\, d\mathcal{S}$$

5.2 Vectorial form of the conservation laws

Mass, momentum and energy equations can be written in a compact, vectorial form:

$$\frac{d}{dt}\int_{\mathcal{V}(t)} \boldsymbol{U}\, d\mathcal{V} + \oint_{\mathcal{S}(t)} \boldsymbol{P_j}\, n_j\, d\mathcal{S} = \int_{\mathcal{V}(t)} \boldsymbol{Q}\, d\mathcal{V} + \oint_{\mathcal{S}(t)} \boldsymbol{G_j}\, n_j\, d\mathcal{S}$$

with:

$$\boldsymbol{U} = \begin{pmatrix} \rho \\ \rho u_i \\ E \end{pmatrix}, \quad \boldsymbol{P_j} = \begin{pmatrix} 0 \\ p\delta_{ij} \\ pu_j \end{pmatrix},$$

$$\boldsymbol{Q} = \begin{pmatrix} 0 \\ \rho f_i \\ \rho f_j u_j \end{pmatrix} \quad \text{and} \quad \boldsymbol{G_j} = \begin{pmatrix} 0 \\ \tau_{ij} \\ \tau_{ij}u_i + k\frac{\partial T}{\partial x_j} \end{pmatrix}$$

The above formulation is based on a fluid element which occupies the volume $\mathcal{V}$ and that moves as the flow-field evolves. The integral conservation principles can be written for a fixed volume $\overline{\mathcal{V}}$ (bounded by a surface $\overline{\mathcal{S}}$), if the Reynolds transport theorem is applied:

$$\frac{d}{dt}\int_{\overline{\mathcal{V}}} \boldsymbol{U}\, d\mathcal{V} + \oint_{\overline{\mathcal{S}}} \boldsymbol{F_j}\, n_j\, d\mathcal{S} = \int_{\overline{\mathcal{V}}} \boldsymbol{Q}\, d\mathcal{V} + \oint_{\overline{\mathcal{S}}} \boldsymbol{G_j}\, n_j\, d\mathcal{S} \tag{5.6}$$

where the vector $\boldsymbol{F_j}$ is defined by:

$$\boldsymbol{F_j} = \boldsymbol{U}u_j + \boldsymbol{P_j}$$

The Reynolds transport theorem for a generic variable ϕ is:

$$\frac{d}{dt}\int_{\mathcal{V}(t)} \phi \, d\mathcal{V} = \frac{d}{dt}\int_{\overline{\mathcal{V}}} \phi \, d\mathcal{V} + \oint_{\overline{\mathcal{S}}} \phi \, \boldsymbol{u}\cdot\boldsymbol{n} \, d\mathcal{S}$$

Eq. (5.6) is the vectorial form of the conservation laws, where $\boldsymbol{U}$ is the vector of conserved variables, $\boldsymbol{F_j}$ is the vector of the Eulerian fluxes, $\boldsymbol{G_j}$ is the vector of viscous fluxes and $\boldsymbol{Q}$ is the vector of external forces. Since in the application we have in mind the volumetric external forces (such as gravity) can be neglected, from now on the vector $\boldsymbol{Q}$ is zero. The variables ρ, ρu_i, and E are called conserved variables because they originate from the conservation laws (i.e., integral governing equation).

Note that, up to now, no hypotheses upon the nature of the fluid have been made. In fact, the above conservation laws are valid for a generic fluid and they can describe a liquid, such as a perfect gas or a supercritical fluid.

The vectorial equation Eq. (5.6) is composed by two scalar equations (mass and energy) and one vectorial equation (momentum) while it depends on six scalar variables (ρ, p, T, e, μ, k) and one vectorial variable ($\boldsymbol{u}$). Thus four fluid property relations must be added to close the system of equations:

- equation of state: EOS
- energy equation of state: e-EOS
- viscosity equation of state: μ-EOS
- thermal conductivity equation of state: k-EOS

The characterization of the fluid arises from these relations; in case of perfect gas the following equations of state are considered:

- EOS: $p = \rho RT$
- e-EOS: $e = c_v T$
- μ-EOS: $\mu = cost$
- k-EOS: $k = cost$

where R is the gas constant and c_v is the (constant) specific heat at constant volume. In case of non perfect gas, more complicated equations of state must be considered. For example, the equations proposed in App. B and C must be used in case of cryogenic fluid.

The introduction of EOS permits to relate the fluid properties. As a consequence, the conserved variables $\boldsymbol{U}$ can be assumed as the independent variables and the fluxes $\boldsymbol{F_j}$ and $\boldsymbol{G_j}$ can be expressed as functions of $\boldsymbol{U}$: $\boldsymbol{F_j} = \boldsymbol{F_j}(\boldsymbol{U})$ and $\boldsymbol{G_j} = \boldsymbol{G_j}(\boldsymbol{U})$.

5.3 Finite volume numerical scheme

A finite volume numerical scheme is based on the discretization of the governing equations written in the integral form (i.e., "conservation law" form).

The physical domain is divided into cells (finite volumes) that are characterized by the average value of the flow variables. The average value is advanced in time by the evaluation of the fluxes at the boundaries of the cell.

5.3.1 1D Euler equation

The finite volume numerical scheme is here illustrated for the one-dimensional non-stationary Eulerian flow:

$$\frac{d}{dt}\int_{x_{i-\frac{1}{2}}}^{x_{i+\frac{1}{2}}} \boldsymbol{U} d\xi + \boldsymbol{F}_{i+\frac{1}{2}} - \boldsymbol{F}_{i-\frac{1}{2}} = 0 \tag{5.7}$$

that is Eq. (5.6) in case of one-dimensional physical domain and of absence of viscous fluxes ($\boldsymbol{G_j} = 0$). In Eq. (5.7), $\boldsymbol{U}$ is the vector of conserved variables and $\boldsymbol{F}$ is the vector of Eulerian fluxes; $\boldsymbol{F}_{i-\frac{1}{2}}$ and $\boldsymbol{F}_{i+\frac{1}{2}}$ represent the fluxes evaluated at the cell interfaces $x_{i-\frac{1}{2}}$ and $x_{i+\frac{1}{2}}$ respectively.

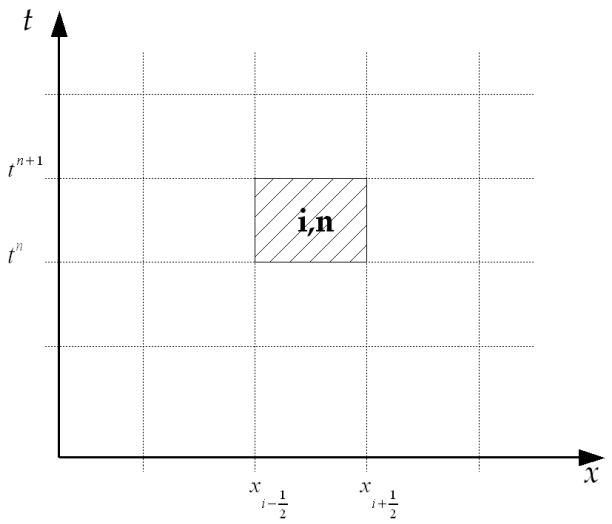

Figure 5.1: Generic finite volume in the one-dimensional time/space domain.

Fig. 5.1 represents a one-dimensional time/space domain characterized by the generic finite volume i, n which is bounded in space by interface $x_{i-\frac{1}{2}}$ between

cells $i-1$ and i and by interface $x_{i+\frac{1}{2}}$ between cells i and $i+1$.

The conserved variables average value in a cell is defined as:

$$\widetilde{\boldsymbol{U}}_i = \frac{1}{\Delta x}\int_{x_{i-\frac{1}{2}}}^{x_{i+\frac{1}{2}}} \boldsymbol{U} d\xi$$

and thus Eq. 5.7 becomes:

$$\frac{d\widetilde{\boldsymbol{U}}_i}{dt} = -\frac{1}{\Delta x}\left(\boldsymbol{F}_{i+\frac{1}{2}} - \boldsymbol{F}_{i-\frac{1}{2}}\right) \tag{5.8}$$

Integration of the above equation across time step $\Delta t = t^{n+1} - t^n$, gives:

$$\widetilde{\boldsymbol{U}}_i^{n+1} = \widetilde{\boldsymbol{U}}_i^{n} - \frac{1}{\Delta x}\int_{t^n}^{t^{n+1}} \left(\boldsymbol{F}_{i+\frac{1}{2}} - \boldsymbol{F}_{i-\frac{1}{2}}\right) d\tau \tag{5.9}$$

where $\widetilde{\boldsymbol{U}}_i^{n+1}$ represents the conserved variables average value in the cell i at the new time step $n+1$ which it can be easily evaluated if a proper estimation of the fluxes $\boldsymbol{F}_{i+\frac{1}{2}}$ and $\boldsymbol{F}_{i-\frac{1}{2}}$ is given. In the finite volume scheme a three step strategy is applied:

- reconstruction of the variables value at the cell interfaces
- local evolution of the solution at the cell interfaces
- evolution of the cell average variables (by Eq. (5.9))

Reconstruction

In the reconstruction step a certain distribution of the variables in the cell must be provided. In the finite volume scheme proposed by Godunov [17] the cell variables are considered as piecewise constant (Fig. 5.2) and thus in Eq. (5.9) the average value $\widetilde{\boldsymbol{U}}$ is equal to the local value $\boldsymbol{U}$.

Using this type of reconstruction the method is first-order accurate in space. If a linear piecewise reconstruction is used for the variables, a second-order accuracy in space is reached (Fig. 5.3).

The slope of the linear cell reconstruction is selected with respect to the average values of the cell $\widetilde{U}_i$ and of the contiguous cell $\widetilde{U}_{i-1}$ and $\widetilde{U}_{i+1}$. Since the linear cell reconstruction can originate non-physical oscillations and thus unstable solution, a slope limiter must be employed to ensure the stability of the numerical scheme (TVD condition). In the present code, a *minmod* slope limiter has been considered. If r is the ratio between the slope at the previous cell and the slope at the actual cell, the *minmod* limiter is:

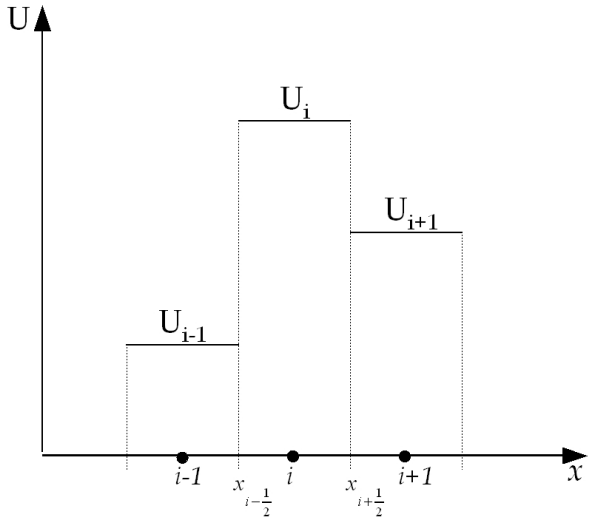

Figure 5.2: Piecewise constant value of the conserved variables.

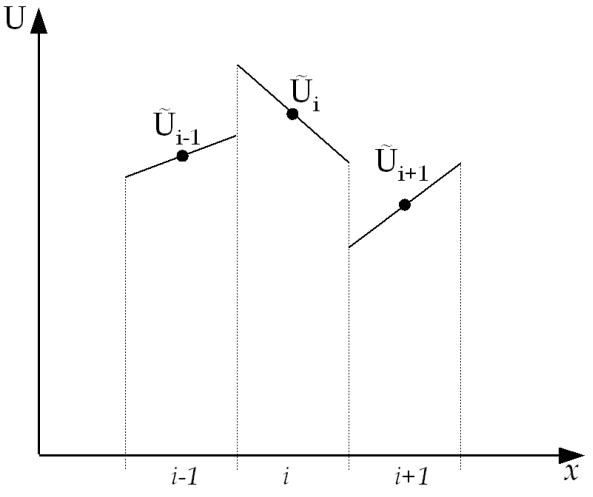

Figure 5.3: Piecewise linear distribution of the conserved variables.

$$\Psi = \max\left(0, \min\left(r, 1\right)\right)$$

That is: if the slope sign of the local cell is the same of the previous cell, the minimum slope is considered for the local cell; otherwise a flat slope is considered for the local cell (Fig. 5.4).

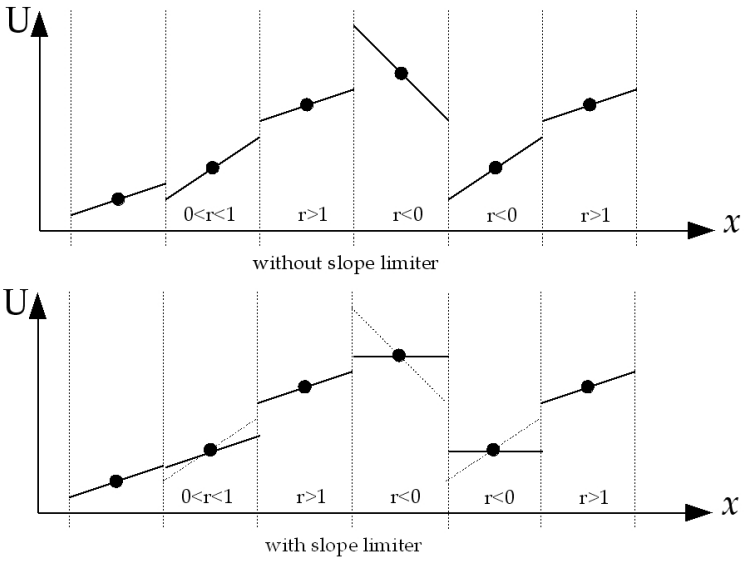

Figure 5.4: Minmod slope limiter effect on linear piecewise distribution.

Local evolution

In the local evolution step the vector of fluxes at the interfaces must be evaluated. The Eulerian flux vector $\boldsymbol{F}_{i+\frac{1}{2}}$ is evaluated by a Riemann problem (see Sec. 5.4) between the right state $\boldsymbol{U}^R_{i+\frac{1}{2}}$ and the left state $\boldsymbol{U}^L_{i+\frac{1}{2}}$ where $\boldsymbol{U}^R_{i+\frac{1}{2}}$ is the value of the solution reconstruction in the cell $i+1$ at the space abscissa $x_{i+\frac{1}{2}}$ and $\boldsymbol{U}^L_{i+\frac{1}{2}}$ is the value of the solution reconstruction in the cell i at the space abscissa $x_{i+\frac{1}{2}}$. The solution of the Riemann problem provides the interface solution $\boldsymbol{U}^{RP}_{i+\frac{1}{2}}$ and thus the interface flux $\boldsymbol{F}_{i+\frac{1}{2}} = \boldsymbol{F}(\boldsymbol{U}^{RP}_{i+\frac{1}{2}})$.

Global evolution

The solution of the Riemann problem is constant between time t^n (initial time of the Riemann problem) and time $t^n + \Delta t$. After that time the waves originated from the contiguous Riemann problems interact, and thus the interface solution is not constant any more (Fig. 5.5).

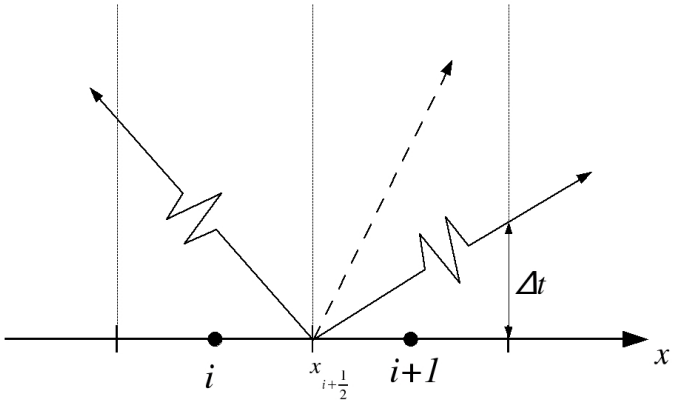

Figure 5.5: Waves originated by Riemann problem at the interface $x_{i+\frac{1}{2}}$.

If λ_{max} is the fastest wave velocity originated by the Riemann problem, the time step Δt must satisfy the condition (called CFL condition):

$$\Delta t \leq \frac{\Delta x}{\lambda_{max}} \tag{5.10}$$

where Δx is the cell spacing. Condition Eq. (5.10) ensures that the solution at the new time step $t^{n+1} = t^n + \Delta t$ is consistent with the previous time step solution. If the interface fluxes are constant through time Δt (that is, Eq. (5.10) is satisfied), Eq. (5.9) can be written as:

$$\widetilde{\boldsymbol{U}}_i^{n+1} = \widetilde{\boldsymbol{U}}_i^n - \frac{\Delta t}{\Delta x}\left(\boldsymbol{F}_{i+\frac{1}{2}} - \boldsymbol{F}_{i-\frac{1}{2}}\right) \tag{5.11}$$

The above equation represents the third step of the finite volume scheme: the evolution of the cell average variables. In fact, once the previous time step solution $\widetilde{\boldsymbol{U}}_i^n$ is known, the new solution $\widetilde{\boldsymbol{U}}_i^{n+1}$ is evaluated by means of the interface flux difference $\boldsymbol{F}_{i+\frac{1}{2}} - \boldsymbol{F}_{i-\frac{1}{2}}$.

5.3.2 3D case

Eq. (5.11) is valid for the one-dimensional case. In the three-dimensional case the generic finite volume is represented by a hexahedral cell (Fig. 5.6) which is characterized by its volume, the unit vectors orthogonal to the cell surfaces and the area of the six lateral surfaces.

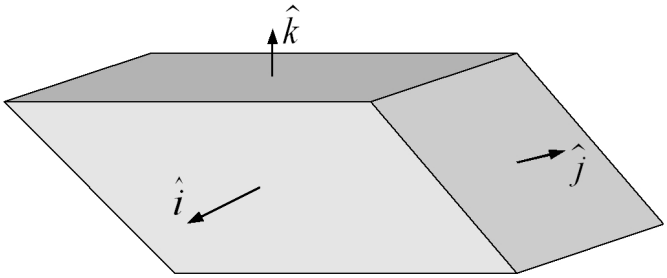

Figure 5.6: Hexaedral three-dimensional cell.

The six Eulerian fluxes at the cell interfaces must be evaluated to compute the new time step $\widetilde{\boldsymbol{U}}_{i,j,k}^{n+1}$. The flux at the generic interface is simply evaluated considering a one-dimensional Riemann problem between the two adjacent cells that overlook the interface; in particular, the scalar velocity considered in the Riemann problem (see Sec. 5.4) is the velocity component that is orthogonal to the interface surface.

5.3.3 Control of time accuracy

Using a linear cell reconstruction a second-order accuracy in space is reached, but using the time integration of Eq. (5.11) time accuracy is first-order. Time accuracy can be controlled and augmented by using Eq. (5.8):

$$\frac{d\widetilde{\boldsymbol{U}}_i}{dt} = -\frac{1}{\Delta x}\left(\boldsymbol{F}_{i+\frac{1}{2}} - \boldsymbol{F}_{i-\frac{1}{2}}\right) = \mathcal{F}\left(\widetilde{\boldsymbol{U}}_i\right) \tag{5.12}$$

where the fluxes $\boldsymbol{F}_{i+\frac{1}{2}}$ and $\boldsymbol{F}_{i-\frac{1}{2}}$, by means of the Riemann problem, are considered as functions of the conserved variables vector $\widetilde{\boldsymbol{U}}_i$. The above expression is

an ODE (Ordinary Differential Equation) and thus the desired time accuracy can be reached by classical ODE numerical integrators. The method of integrating the finite volume scheme by means of Eq. (5.12) is referred to as *method of lines*.

Considering an explicit integration by means of the Runge-Kutta methods, the second and third order time accuracy schemes are (neglecting the subscript i and the tilde$\widetilde{\ }$):

- 2^{nd} order (Heun scheme):

$$\begin{aligned} \boldsymbol{U}^{n+1} &= \boldsymbol{U}^n + \frac{\Delta t}{2}[\mathcal{F}(\boldsymbol{U}^n) + \mathcal{F}(\boldsymbol{U}_I)] \\ \boldsymbol{U}_I &= \boldsymbol{U}^n + \Delta t\, \mathcal{F}(\boldsymbol{U}^n) \end{aligned}$$

- 3^{rd} order (Shu-Osher scheme [45])

$$\begin{aligned} \boldsymbol{U}^{n+1} &= \frac{1}{3}(\boldsymbol{U}^n + 2\boldsymbol{U}_{IV}) \\ \boldsymbol{U}_{IV} &= \boldsymbol{U}_{III} + \Delta t\, \mathcal{F}(\boldsymbol{U}_{III}) \\ \boldsymbol{U}_{III} &= \frac{1}{4}(3\boldsymbol{U}^n + \boldsymbol{U}_{II}) \\ \boldsymbol{U}_{II} &= \boldsymbol{U}_I + \Delta t\, \mathcal{F}(\boldsymbol{U}_I) \\ \boldsymbol{U}_I &= \boldsymbol{U}^n + \Delta t\, \mathcal{F}(\boldsymbol{U}^n) \end{aligned}$$

In the present code the Shu-Osher time integration has been chosen. Using this scheme, the stability condition is $CFL \leq 1$ where the CFL number is defined as:

$$CFL = \frac{\Delta t\, S}{\Delta x} \tag{5.13}$$

where S is the maximum wave velocity that originates from the interface Riemann problem. Every finite volume has its time step Δt:

$$\Delta t_i = CFL\, \frac{\Delta x_i}{S_i}$$

where Δx_i and S_i are the local cell spacing and wave velocity. If the global time step Δt seen in Eq. (5.12) is the minimum between the entire space domain at time t^n (that is, $\Delta t = \min_i \Delta t_i$), time accuracy is preserved but the smallest cell (i.e., the one with smallest Δt_i) slows down the time evolution of the biggest cells. This problem becomes critical in case of stretched grids where the biggest cell can be 10000 times (or even more) the smallest one. If the steady-state solution is the only goal of the computation, time accuracy can be sacrificed by considering the local time step Δt_i for every finite volume. Using this method, convergence to steady-state solution is reached much faster.

5.3.4 Viscous fluxes

In case of viscous flow, the viscous fluxes must be added in Eq. (5.7):

$$\frac{d}{dt}\int_{x_{i-\frac{1}{2}}}^{x_{i+\frac{1}{2}}} \boldsymbol{U} d\xi + \boldsymbol{F}_{i+\frac{1}{2}} - \boldsymbol{F}_{i-\frac{1}{2}} = \boldsymbol{G}_{i+\frac{1}{2}} - \boldsymbol{G}_{i-\frac{1}{2}}$$

that is Eq. (5.7) in case of one-dimensional viscous flow where $\boldsymbol{G}_{i+\frac{1}{2}}$ and $\boldsymbol{G}_{i-\frac{1}{2}}$ represent the viscous fluxes evaluated at the cell interfaces $x_{i+\frac{1}{2}}$ and $x_{i-\frac{1}{2}}$.

The evaluation of the viscous fluxes is similar to the one of the Eulerian fluxes since the cell variables ($\widetilde{\boldsymbol{U}}_i$ in case of conserved variables) provide the value of the variables at the interface ($\boldsymbol{U}_{i+\frac{1}{2}}$ in case of conserved variables). Finally, the viscous fluxes are determined by the intercell values: $\boldsymbol{G}_{i+\frac{1}{2}} = \boldsymbol{G}(\boldsymbol{U}_{i+\frac{1}{2}})$. In case of Eulerian fluxes, the interface value is determined by the Riemann problem while in case of viscous fluxes a second order central differencing is used and thus the variables at the contiguous cells are needed ($\widetilde{\boldsymbol{U}}_{i-1}$, $\widetilde{\boldsymbol{U}}_i$, and $\widetilde{\boldsymbol{U}}_{i+1}$ in case of conserved variables):

$$\boldsymbol{G}_{i+\frac{1}{2}} = \boldsymbol{G}\left(\frac{\widetilde{\boldsymbol{U}}_{i+1} + \widetilde{\boldsymbol{U}}_i}{2}\right) \quad \text{and} \quad \boldsymbol{G}_{i-\frac{1}{2}} = \boldsymbol{G}\left(\frac{\widetilde{\boldsymbol{U}}_i + \widetilde{\boldsymbol{U}}_{i-1}}{2}\right)$$

The stability condition in case of pure viscous flow,

$$\frac{d}{dt}\int_{x_{i-\frac{1}{2}}}^{x_{i+\frac{1}{2}}} \boldsymbol{U} d\xi + = \boldsymbol{G}_{i+\frac{1}{2}} - \boldsymbol{G}_{i-\frac{1}{2}}$$

is:

$$\Delta t_{visc} = \frac{K\Delta x^2}{\nu}$$

where Δx is the cell spacing, ν is the kinematic viscosity and K is a coefficient that must satisfy the condition: $K \leq 0.3$. In the present code the integration time step Δt is the minimum between the Eulerian time step Δt_{eul} (i.e., CFL condition Eq. (5.13)) and the viscous time step Δt_{visc}. This choice ensures the stability for both the Eulerian and the viscous fluxes.

5.4 Riemann problem

As already seen in Sec. 5.3, the finite volume numerical scheme is based on the solution of the Riemann problem. In fact the intercell Eulerian flux $\boldsymbol{F}_{i+\frac{1}{2}}$ at the generic interface $x_{i+\frac{1}{2}}$ is the flux evaluated at the intercell variable $\boldsymbol{U}^{RP}_{i+\frac{1}{2}}$:

$$\boldsymbol{F}_{i+\frac{1}{2}} = \boldsymbol{F}\left(\boldsymbol{U}^{RP}_{i+\frac{1}{2}}\right)$$

where $\boldsymbol{U}^{RP}_{i+\frac{1}{2}}$ is the solution of the Riemann problem:

$$\boldsymbol{U}^{RP}_{i+\frac{1}{2}} = \mathcal{RP}\left(\boldsymbol{U}^{L}_{i+\frac{1}{2}}, \boldsymbol{U}^{R}_{i+\frac{1}{2}}\right)$$

The Riemann problem is the interface solution ($x = 0$) of the one-dimensional problem:

$$\begin{cases} \boldsymbol{U}_t + \boldsymbol{F}(\boldsymbol{U})_x = 0 \\ \boldsymbol{U}(x, t = 0) = \begin{cases} \boldsymbol{U}^L & \text{if } x < 0 \\ \boldsymbol{U}^R & \text{if } x > 0 \end{cases} \end{cases} \tag{5.14}$$

where $\boldsymbol{U}_t + \boldsymbol{F}(\boldsymbol{U})_x = 0$ is the one-dimensional differential form of the Eulerian conservation law (Eq. (5.6)) and $\boldsymbol{U}(x, t = 0)$ is the initial condition of the Riemann problem. The interface solution of the problem Eq. (5.14) is a function of the two piecewise left and right initial conditions $\boldsymbol{U}^L$ and $\boldsymbol{U}^R$ and thus it is represented by:

$$\boldsymbol{U}(x = 0, t) = \boldsymbol{U}^{RP} = \mathcal{RP}\left(\boldsymbol{U}^L, \boldsymbol{U}^R\right)$$

The function $\mathcal{RP}$ can be evaluated using an exact solver or an approximate solver. To better comprehend the characterization of the Riemann Problem, in the next subsections the one-dimensional Eulerian problem for a generic compressible fluid will be introduced and then some approximate Riemann solver for a generic fluid will be presented.

5.4.1 1D Euler equation with a generic EOS

The Euler equations in conservative differential form are:

$$\frac{\partial \boldsymbol{U}}{\partial t} + \frac{\partial \boldsymbol{F}(\boldsymbol{U})}{\partial x} = 0$$

setting:

$$\boldsymbol{U} = \begin{pmatrix} \rho \\ \rho u \\ E \end{pmatrix}, \quad \boldsymbol{F}(\boldsymbol{U}) = \begin{pmatrix} \rho u \\ \rho u^2 + p \\ u(E + p) \end{pmatrix} \quad \text{and} \quad E = \rho\left(\frac{1}{2}u^2 + e\right)$$

where $\boldsymbol{U}$ is the vector of conserved variables and $\boldsymbol{F}(\boldsymbol{U})$ is the vector of fluxes. If e denotes the internal energy, then some law (an Equation Of State) is required to close the whole system:

$$p = p(\rho, e)$$

In this framework the EOS has density and specific internal energy as independent variables. This formulation does not limit the results here presented since the properties of the Euler equations are not related to the chosen independent variables of the EOS.

The conservation laws can be also written in the quasi-linear form:

$$\frac{\partial \boldsymbol{U}}{\partial t} + \underline{\underline{\boldsymbol{A}}}(\boldsymbol{U})\frac{\partial \boldsymbol{U}}{\partial x} = 0$$

where the Jacobian matrix $\underline{\underline{\boldsymbol{A}}}(\boldsymbol{U})$ is:

$$\underline{\underline{\boldsymbol{A}}}(\boldsymbol{U}) = \frac{\partial \boldsymbol{F}(\boldsymbol{U})}{\partial \boldsymbol{U}} = \begin{pmatrix} 0 & 1 & 0 \\ K - u^2 & u(2-k) & k \\ (K-H)u & H - ku^2 & u(1+k) \end{pmatrix}$$

setting:

$$H = \frac{E+p}{\rho}, \quad k^{-1} = \rho \left.\frac{\partial e}{\partial p}\right|_{\rho} \quad \text{and} \quad K = a^2 + k(u^2 - H)$$

The speed of acoustic waves a is given by the following thermodynamic relation:

$$a = \sqrt{\frac{\dfrac{p}{\rho^2} - \left.\dfrac{\partial e}{\partial \rho}\right|_p}{\left.\dfrac{\partial e}{\partial p}\right|_{\rho}}}$$

The eigenvalues of the Jacobian matrix $\underline{\underline{\boldsymbol{A}}}(\boldsymbol{U})$ are: $\lambda_1 = u - a$, $\lambda_2 = u$ and $\lambda_3 = u + a$; the right eigenvectors are:

$$\boldsymbol{r_1}(\boldsymbol{U}) = \begin{pmatrix} 1 \\ u - a \\ H - ua \end{pmatrix}, \quad \boldsymbol{r_2}(\boldsymbol{U}) = \begin{pmatrix} 1 \\ u \\ H - \frac{a^2}{k} \end{pmatrix}, \quad \boldsymbol{r_3}(\boldsymbol{U}) = \begin{pmatrix} 1 \\ u + a \\ H + ua \end{pmatrix}$$

Note that the generic EOS $p = p(\rho, e)$ must satisfy the physical restrictions: $\rho > 0$ and $a \in \Re$. This latter constraint ensures that all the eigenvectors of the Jacobian matrix are real (i.e., hyperbolicity of the conservation laws).

In an alternative way, Euler equations can be rearranged and thus may be written in a non conservative form, when restricting to smooth solutions. For example, the primitive variables formulation is:

$$\frac{\partial \boldsymbol{W}}{\partial t} + \underline{\underline{\boldsymbol{A}}}(\boldsymbol{W})\frac{\partial \boldsymbol{W}}{\partial x} = 0$$

where $\boldsymbol{W}$ is the vector of primitive variables and $\boldsymbol{F}(\boldsymbol{W})$ is the vector of fluxes referred to primitive variables:

$$\boldsymbol{W} = \begin{pmatrix} \rho \\ u \\ p \end{pmatrix}, \quad \underline{\underline{\boldsymbol{A}}}(\boldsymbol{W}) = \begin{pmatrix} u & \rho & 0 \\ 0 & u & 1/\rho \\ 0 & \rho a^2 & u \end{pmatrix}$$

The left eigenvectors associated to the eigenvalues $\lambda_1 = u - a$, $\lambda_2 = u$ and $\lambda_3 = u + a$ of the Jacobian matrix $\underline{\underline{\boldsymbol{A}}}(\boldsymbol{W})$ are:

$$\boldsymbol{r_1}(\boldsymbol{W}) = \begin{pmatrix} 1 \\ -a/\rho \\ a^2 \end{pmatrix}, \quad \boldsymbol{r_2}(\boldsymbol{W}) = \begin{pmatrix} 1 \\ 0 \\ 0 \end{pmatrix}, \quad \boldsymbol{r_3}(\boldsymbol{W}) = \begin{pmatrix} 1 \\ +a/\rho \\ a^2 \end{pmatrix}$$

This formulation has the advantage to be strictly related to the 2^{nd} field invariants, which are the flow variables that are transported across the wave $\lambda_2 = u$ (see [48] for more information).

Euler equations can also be written using the wave variables formulation:

$$\frac{\partial \boldsymbol{V}}{\partial t} + \underline{\underline{\boldsymbol{A}}}(\boldsymbol{V})\frac{\partial \boldsymbol{V}}{\partial x} = 0$$

where $\boldsymbol{V}$ is the vector of wave variables and $\underline{\underline{\boldsymbol{A}}}(\boldsymbol{V})$ is the Jacobian matrix referred to the wave variables:

$$\boldsymbol{V} = \begin{pmatrix} \varphi \\ u \\ s \end{pmatrix}, \quad \underline{\underline{\boldsymbol{A}}}(\boldsymbol{V}) = \begin{pmatrix} u & a & 0 \\ a & u & T/\rho\, c_p \\ 0 & 0 & u \end{pmatrix}$$

where s is the entropy, T is the temperature, c_p is the specific heat at constant pressure, and φ is defined as:

$$d\varphi = \frac{a}{\rho} d\rho$$

This formulation has the advantage to be strictly related to the 1^{st} and 3^{rd} field invariants, which are the flow variables that are transported across the wave $\lambda_1 = u - a$ and $\lambda_3 = u + a$ respectively (see [48] for more information).

The left eigenvectors associated to the eigenvalues $\lambda_1 = u - a$, $\lambda_2 = u$ and $\lambda_3 = u + a$ of the Jacobian matrix $\underline{\underline{\boldsymbol{A}}}(\boldsymbol{V})$ are:

$$\boldsymbol{r_1}(\boldsymbol{V}) = \begin{pmatrix} 1 \\ -1 \\ 0 \end{pmatrix}, \quad \boldsymbol{r_2}(\boldsymbol{V}) = \begin{pmatrix} 1 \\ 0 \\ -\frac{\rho a \left.\frac{\partial e}{\partial p}\right|_\rho}{T} \end{pmatrix}, \quad \boldsymbol{r_3}(\boldsymbol{V}) = \begin{pmatrix} 1 \\ +1 \\ 0 \end{pmatrix}$$

Note that the eigenvalues are always the same, whatever is the set of the variable used to express the governing equations [15].

5.4.2 Riemann problem for a generic EOS

The Riemann Problem is:

$$\begin{cases} \boldsymbol{U}_t + \boldsymbol{F}(\boldsymbol{U})_x = 0 \\ \boldsymbol{U}(x, t=0) = \begin{cases} \boldsymbol{U}^L & \text{if } x < 0 \\ \boldsymbol{U}^R & \text{if } x > 0 \end{cases} \end{cases}$$

In solving the Riemann Problem we shall frequently make use of the vector $W = \{\rho, u, p\}^T$ of primitive variables, that is:

$$\begin{cases} \boldsymbol{W}_t + \boldsymbol{F}(\boldsymbol{W})_x = 0 \\ \boldsymbol{W}(x, t=0) = \begin{cases} \boldsymbol{W}^L & \text{if } x < 0 \\ \boldsymbol{W}^R & \text{if } x > 0 \end{cases} \end{cases}$$

For the case in which no vacuum is present, the exact solution of the Riemann Problem has three waves which are associated to the three eigenvalues of the Jacobian matrix of the system: $\lambda_1 = u - a$, $\lambda_2 = u$ and $\lambda_3 = u + a$ (Fig. 5.7).

The three waves separate four constant states, which from the left to the right are W_L (data on the left side), W_{*L}, W_{*R}, and W_R (data on the right side). The unknown region between the left and the right waves, the star region, is divided by a contact discontinuity (which is the wave $\lambda_2 = u$). The left and the right waves can be either shock or rarefaction waves. Both pressure p_* and velocity u_* between the left and right waves are constant, while the density has two constant values: ρ_{*L} and ρ_{*R}. More precisely, the three waves originated from a Riemann Problem are:

Contact discontinuities

The contact wave is a discontinuous wave associated with the 2^{nd} characteristic field ($\lambda_2 = u$) whose Generalized Riemann Invariants are:

$$\begin{cases} u = \text{const} \\ p = \text{const} \end{cases}$$

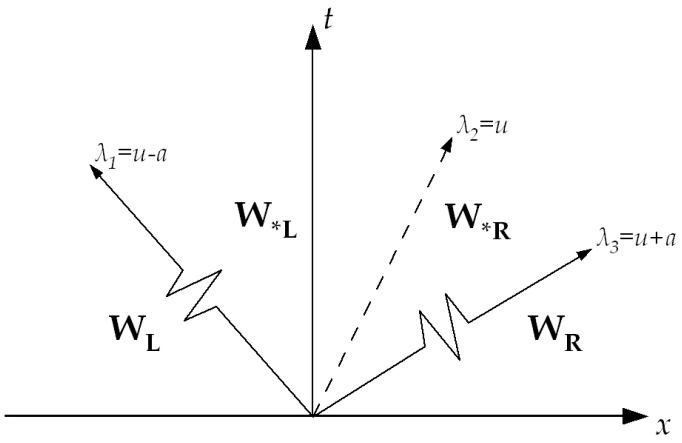

Figure 5.7: Schematic of the generic Riemann problem.

A contact wave is a discontinuous wave across which both pressure and velocity are constant but density jumps discontinuously as do variables that depend on density, such as specific internal energy, temperature, entropy, etc.

Rarefaction waves

A rarefaction wave is a smooth wave associated with the 1^{st} and 3^{rd} characteristic field across which ρ, u and p change. The wave has a fan-type shape and is enclosed by two bounding characteristics corresponding to the head and the tail of the wave. Across the wave the Generalized Riemann Invariants apply.

The Generalized Riemann Invariants associated with the 1^{st} characteristic field ($\lambda_1 = u - a$) are:

$$\begin{cases} u + \varphi = \text{const} \\ s = \text{const} \end{cases} \tag{5.15}$$

The Generalized Riemann Invariants associated with the 3^{rd} characteristic field ($\lambda_3 = u + a$) are:

$$\begin{cases} u - \varphi = \text{const} \\ s = \text{const} \end{cases} \tag{5.16}$$

Eq. (5.15) and Eq. (5.16) are not useful because variable φ is a non-physical

variable which has been introduced with the only goal to write the above Generalized Riemann Invariants in a close form. We want to give an approximate form of these relations that will allow us to use these relations in Sec. 5.5.

The differential form of the above expressions is:

$$\begin{cases} du \pm a\dfrac{d\rho}{\rho} = 0 \\ \\ ds = 0 \end{cases}$$

The hypothesis of small differences between the two states across the rarefaction wave is made. This hypothesis is acceptable in case of the Riemann problem that arises at the interfaces of a finite volume method, since the differences between two adjacent cells are small.

The speed of sound for a generic fluid is (see Sec. A.5):

$$a^2 = \left(\frac{\partial p}{\partial \rho}\right)_s = \frac{c_p}{c_v}\left(\frac{\partial p}{\partial \rho}\right)_T = \gamma\left(\frac{\partial p}{\partial \rho}\right)_T$$

where γ is the ratio of specific heats and, for a generic fluid, it is a function of pressure and density: $\gamma = \gamma(p, \rho)$. A generic fluid can be modeled in a trivial way: $p = \overline{Z}\rho RT$ where the compressibility factor $\overline{Z}$ is considered constant. Thus the speed of sound becomes:

$$a^2 = \gamma\frac{p}{\rho} \tag{5.17}$$

Using the isentropic transformation law $dp = a^2 d\rho$ (from the definition of the speed of sound), the relation between pressure and density along an isentropic transformation is:

$$\frac{dp}{p} = \gamma\frac{d\rho}{\rho}$$

Moreover, differentiating the speed of sound $a^2 = a^2(p, \rho)$, the relation $du \pm a\frac{d\rho}{\rho}$ can be rearranged in the following way:

$$du \pm \frac{da}{\delta} = 0$$

where δ is a function of pressure and density:

$$\delta(p, \rho) = \frac{1}{2}\left[\rho a\left(\frac{\partial a}{\partial p}\right)_\rho + \frac{\rho}{a}\left(\frac{\partial a}{\partial \rho}\right)_p\right] \tag{5.18}$$

Finally, the Generalized Riemann Invariants associated with the 1^{st} and 3^{rd} characteristic field become:

$$\begin{cases} du \pm \dfrac{da}{\delta} = 0 \\ \dfrac{dp}{p} = \gamma \dfrac{d\rho}{\rho} \end{cases}$$

In case of perfect gas, $\gamma = cost$, $\delta = (\gamma - 1)/2$, and thus the above expression can be integrated in a close form:

$$\begin{cases} u \pm \dfrac{a}{\delta} = \text{const} \\ \dfrac{p}{\rho^{\gamma}} = \text{const} \end{cases} \tag{5.19}$$

In the case of a generic fluid, Eq. (5.19) can also be used if a constant value for $\overline{\gamma}$ and $\overline{\delta}$ is assumed. For example, if a state (referred with $\bar{}$) is known, $\overline{\gamma}$ can be evaluated by means of Eq. (5.17) and $\overline{\delta}$ by means of Eq. (5.18).

Shock waves

The shock wave is a discontinuous wave associated with the 1^{st} and 3^{rd} characteristic field. All three quantities ρ, u and p change across a shock wave. Across the shock wave the Rankine-Hugoniot conditions apply: given a system of hyperbolic conservation laws: $\boldsymbol{U}_t + \boldsymbol{F}(\boldsymbol{U})_x = 0$ and a discontinuous solution of speed S_i associated with the λ_i-characteristic field, the Rankine-Hugoniot Conditions state:

$$\boldsymbol{F}(\boldsymbol{U}^R) - \boldsymbol{F}(\boldsymbol{U}^L) = S_i(\boldsymbol{U}^R - \boldsymbol{U}^L) \tag{5.20}$$

where $\boldsymbol{U}^L$ and $\boldsymbol{U}^R$ are the respective states immediately to the left and right of the discontinuity. The velocity S_i must satisfy the entropy condition [48]:

$$\lambda_i(\boldsymbol{U}^L) > S_i > \lambda_i(\boldsymbol{U}^R)$$

5.4.3 Approximate riemann solver for a generic EOS

Since the exact solution of the Riemann problem is a non trivial and time consuming computation, we want to provide an approximation of the interface solution $\boldsymbol{U}^{RP}_{i+\frac{1}{2}}$ of the Riemann problem (Eq. (5.14)). The need of an approximate evaluation is critical in the case of a generic fluid where the close form of the

Riemann problem does not exist. Several approximate Riemann solvers exist for ideal gas. We decided to extend the PVRS, HLL, HLLC and Roe Riemann Solver to a generic fluid.

Primitive Variables Riemann Solver (PVRS)

This family of Riemann solvers is based on the linearized form of the Euler equations, using the primitive variables:

$$\boldsymbol{W}_t + \overline{\underline{\underline{\boldsymbol{A}}}}\boldsymbol{W}_x = 0 \tag{5.21}$$

where $\overline{\underline{\underline{\boldsymbol{A}}}} = \underline{\underline{\boldsymbol{A}}}(\overline{\boldsymbol{W}})$ is the Jacobian matrix evaluated at the constant state $\overline{\boldsymbol{W}}$. Eq. (5.21) is a linear hyperbolic system which is a good approximation of the non linear Euler equations if it is assumed that the initial data $\boldsymbol{W}^L$ and $\boldsymbol{W}^R$ and the solution $\boldsymbol{W}^{RP}$ of the Riemann problem are close to the constant state $\overline{\boldsymbol{W}}$. Eq. (5.21) can be solved considering the Rankine-Hugoniot conditions (Eq. 5.20) across the waves of speed $\overline{\lambda}_1$ and $\overline{\lambda}_3$ (where $\overline{\lambda_i}$ are the eigenvalues of the matrix $\overline{\underline{\underline{\boldsymbol{A}}}}$). With this assumption the star region solution is:

$$\begin{cases} p^* &= \dfrac{1}{2}(p^L + p^R) + \dfrac{1}{2}(u^L - u^R)\overline{\rho a} \\ u^* &= \dfrac{1}{2}(u^L + u^R) + \dfrac{1}{2}(p^L - p^R)/(\overline{\rho a}) \\ \rho^{*L} &= \rho^L + (u^L - u^*)\overline{\rho}/\overline{a} \\ \rho^{*R} &= \rho^R + (u^* - u^R)\overline{\rho}/\overline{a} \end{cases}$$

where the constant state $\overline{\boldsymbol{W}}$ can be given by:

$$\overline{\rho} = \frac{1}{2}(\rho^L + \rho^R) \quad \text{and} \quad \overline{a} = \frac{1}{2}(a^L + a^R)$$

The Riemann problem is finally given by:

$$\boldsymbol{W}^{RP} = \begin{cases} \boldsymbol{W}^L & \text{if} \quad 0 \leq S^L \\ \boldsymbol{W}^{*L} & \text{if} \quad S^L \leq 0 \leq S^* \\ \boldsymbol{W}^{*R} & \text{if} \quad S^* \leq 0 \leq S^R \\ \boldsymbol{W}^R & \text{if} \quad S^R \leq 0 \end{cases}$$

where S^R, S^L, and S^* are the speeds of the three waves originated by the Riemann problem which can be computed by the following algorithm:

$$
\begin{aligned}
S^L &= \begin{cases} u^L - a^L & \text{if } p^* \le p^L \\ u^L + \dfrac{p^* - p^L}{\rho^L (u^* - u^L)} & \text{if } p^* > p^L \end{cases} \\
S^* &= u^* \\
S^R &= \begin{cases} u^L + a^L & \text{if } p^* \le p^R \\ u^R + \dfrac{p^* - p^R}{\rho^R (u^* - u^R)} & \text{if } p^* > p^R \end{cases}
\end{aligned}
$$

Note that if $p_* < p_k$ (k=L,R), the wave is a rarefaction and then the wave speed S_k corresponds to the characteristic speed of the head of the rarefaction. If the wave is a shock ($p_* > p_k$) then the wave speed corresponds to the shock speed (as obtained from the mass and momentum Rankine-Hugoniot relations).

This PVRS based on the Rankine-Hugoniot conditions supplies a very good approximation of the Riemann problem in the case of double shock solution. A PVRS accurate in the case of double expansion can be formulated by considering the generalized Riemann Invariants (Eq. (5.15) and (5.16)) instead of the Rankine-Hugoniot conditions.

HLL Riemann solvers

The central idea is to assume a wave configuration for the solution that consists of two waves separating three constant states. This assumption is strictly correct only for hyperbolic systems of two equations. The estimated intercell solution is given by:

$$
\boldsymbol{U}_{i+\frac{1}{2}} = \begin{cases} \boldsymbol{U}^L & \text{if } 0 \le S^L \\ \boldsymbol{U}^{HLL} & \text{if } S^L \le 0 \le S^R \\ \boldsymbol{U}^R & \text{if } S^R \le 0 \end{cases}
$$

where S^L and S^R are the fastest signal velocities perturbing the initial states left and right and $\boldsymbol{U}^{HLL}$ is the HLL star region, given by:

$$
\boldsymbol{U}^{HLL} = \frac{S^R \boldsymbol{U}^R - S^L \boldsymbol{U}^L + \boldsymbol{F}^L - \boldsymbol{F}^R}{S^R - S^L}
$$

and $\boldsymbol{F}^L = \boldsymbol{F}(\boldsymbol{U}^L)$ and $\boldsymbol{F}^R = \boldsymbol{F}(\boldsymbol{U}^R)$ are the left and right fluxes. Note that some assumption must be made to evaluate the velocities S^R and S^L (see, for example, the evaluation proposed for PVRS).

HLLC Riemann solvers

The shortcoming of the HLL scheme is the lack of the contact wave. This defect may be corrected by restoring the missing wave. This Riemann Solver is the HLLC scheme where C stands for Contact and is given by:

$$\boldsymbol{U}_{i+\frac{1}{2}} = \begin{cases} \boldsymbol{U}^L & \text{if} \quad 0 \leq S^L \\ \boldsymbol{U}^{*L} & \text{if} \quad S^L \leq 0 \leq S^* \\ \boldsymbol{U}^{*R} & \text{if} \quad S^* \leq 0 \leq S^R \\ \boldsymbol{U}^R & \text{if} \quad S^R \leq 0 \end{cases}$$

where the star region estimation is given by:

$$\boldsymbol{U}^{*k} = \begin{bmatrix} \rho^{*k} \\ \rho^{*k} u^{*k} \\ E^{*k} \end{bmatrix} = \rho^k \left(\frac{S^k - u^k}{S^k - S^*} \right) \begin{bmatrix} 1 \\ S^* \\ \dfrac{E^k}{\rho^k} + (S^* - u^k) \left[S^* + \dfrac{p^k}{\rho^k (S^k - u^k)} \right] \end{bmatrix}$$

with k=L and k=R.

Note that an evaluation for p_*, u_*, and the wave velocities S^R, S^L, and S^* must be provided (see, for example, the evaluation proposed for PVRS).

The Riemann solver of Roe

Roe's approach replaces the Jacobian matrix $\boldsymbol{A}(\boldsymbol{U})$ by a constant matrix $\tilde{\boldsymbol{A}} = \tilde{\boldsymbol{A}}(\boldsymbol{U}^L, \boldsymbol{U}^R)$ so that the problem:

$$\begin{cases} \boldsymbol{U}_t + \tilde{\boldsymbol{A}} \boldsymbol{U}_x = 0 \\ \boldsymbol{U}(x, t=0) = \begin{cases} \boldsymbol{U}^L & \text{if } x < 0 \\ \boldsymbol{U}_R & \text{if } x > 0 \end{cases} \end{cases}$$

is a linear system with constant coefficients which can be solved exactly. After algebra, the intercell flux is:

$$\boldsymbol{F}_{i+\frac{1}{2}} = \frac{1}{2}(\boldsymbol{F}^L + \boldsymbol{F}^R) - \frac{1}{2} \sum_{i=1}^{m} \tilde{\alpha}_i |\tilde{\lambda}_i| \tilde{\boldsymbol{K}}_i$$

where $\tilde{\lambda}_i = \tilde{\lambda}_i(\boldsymbol{U}^L, \boldsymbol{U}^R)$ are the real eigenvalues and $\tilde{\boldsymbol{K}}_i(\boldsymbol{U}^L, \boldsymbol{U}^R)$ are a complete set of linearly independent right eigenvalues of the linearized matrix $\tilde{\boldsymbol{A}}(\boldsymbol{U}^L, \boldsymbol{U}^R)$ and $\tilde{\alpha}_i(\boldsymbol{U}^L, \boldsymbol{U}^R)$ are the wave strengths. All these variables are function of a fictitious *tilde* state defined as follow:

$$\begin{cases} \tilde{\rho} = \sqrt{\rho^L \rho^R} \\ \\ \tilde{u} = \dfrac{\sqrt{\rho^R} u^R + \sqrt{\rho^L} u^L}{\sqrt{\rho^R} + \sqrt{\rho^L}} \\ \\ \tilde{H} = \dfrac{\sqrt{\rho^R} H^R + \sqrt{\rho^L} H^L}{\sqrt{\rho^R} + \sqrt{\rho^L}} \end{cases}$$

Note that the pressure $\tilde{p}$ can be obtained by the inversion of the thermodynamic relation:

$$\tilde{H} = \frac{1}{2}\tilde{u}^2 + e(\tilde{p}, \tilde{\rho}) + \frac{\tilde{p}}{\tilde{\rho}}$$

The Roe's solver gives an entropy violating solution in case of transonic rarefaction wave. Thus, the Roe's solver must be modified so as to avoid entropy violating solutions. This is usually referred to as an "entropy fix".

Note: the four Riemann solver here described have been tested on a simple one-dimensional Eulerian problem. No appreciable differences between the four Riemann problem have risen and thus, for the multidimensional computations presented in the following chapter the PVRS, has been chosen in order to reduce the time computation. In fact PVRS is one of the simplest Riemann problem solver that can be implemented in a numerical code.

5.5 Boundary conditions

The Eulerian and viscous fluxes at the interface must be evaluated by considering the variables in the contiguous cells that overlook the interface. As a consequence, the interface fluxes at the boundaries of the physical domain cannot be computed and thus some boundary conditions must be employed.

In the case of viscous fluxes, a "shell" of ghost cells is considered. These ghost cells surround the physical domain, thus permitting the evolution of the boundary viscous fluxes. The variables in the ghost cells are assigned depending on the boundary condition (wall, inflow/outflow, etc.). This approach is valid even for Eulerian fluxes but in the case of inflow/outflow condition a special treatment is required: a fictitious Riemann problem at the boundary interface is considered. This treatment has been adapted for the general fluid case and thus it is presented in the following subsections.

5.5.1 Supersonic outflow

In the case of supersonic outflow ($u > a$) the three waves $\lambda_1 = u - a$, $\lambda_2 = u$ and $\lambda_3 = u + a$ are directed outwards the physical domain (see Fig. 5.8).

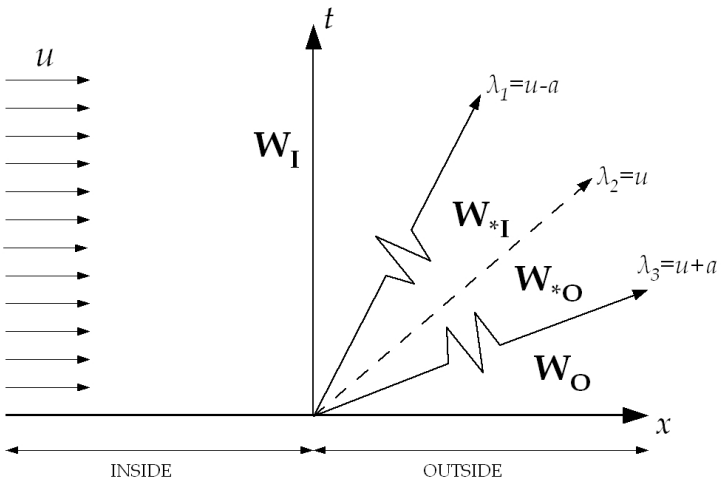

Figure 5.8: Schematic of the Riemann problem in case of supersonic outflow.

For that reason the solution at the interface (ρ_{int}, u_{int}, and p_{int}) is directly given by the known inside solution, i.e.:

$$\begin{cases} \rho_{int} &= \rho_I \\ u_{int} &= u_I \\ p_{int} &= p_I \end{cases}$$

where I means "inside".

Hence, in the case of supersonic outflow, no boundary conditions must be provided.

5.5.2 Supersonic inflow

In the case of supersonic inflow ($u > a$) the three waves $\lambda_1 = u - a$, $\lambda_2 = u$ and $\lambda_3 = u + a$ are directed inwards the physical domain (see Fig. 5.9).

For that reason the solution at the interface (ρ_{int}, u_{int}, and p_{int}) is completely given by the external conditions, i.e.:

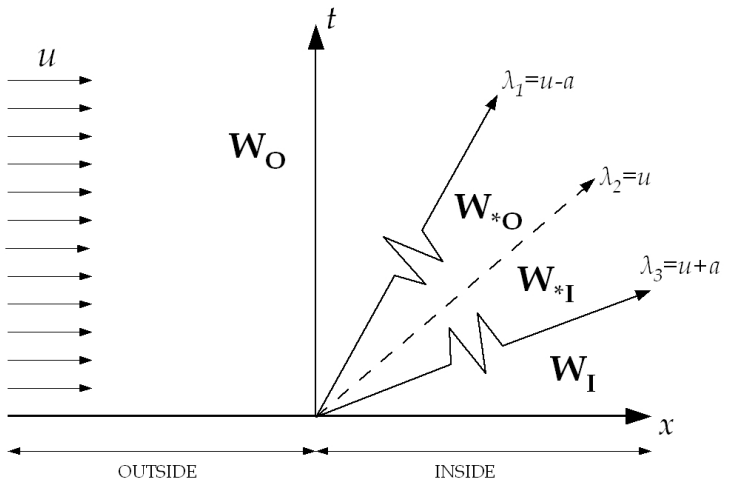

Figure 5.9: Schematic of the Riemann problem in case of supersonic inflow.

$$\begin{cases} \rho_{int} &= \rho_O \\ u_{int} &= u_O \\ p_{int} &= p_O \end{cases}$$

where O means "outside".

The outside state must be assigned since it is unknown. In the present code a typical choice for the supersonic inflow condition has been adopted: stagnation state and Mach number Ma. This approach is widely adopted because the stagnation inflow condition (for both supersonic and subsonic flow) represents the reservoir condition of most practical application (coolant at inlet manifold, hot-gas at combustion chamber, etc.). The stagnation state (referred with t) is characterized by two thermodynamic variables (pressure p_t and speed of sound a_t, in the present code) and it can be related to the static state by means of the following relations:

$$\begin{cases} h_t &= h + \dfrac{u^2}{2} = e + \dfrac{p}{\rho} + \dfrac{a^2 Ma^2}{2} \\ s_t &= s \end{cases}$$

In the case of a generic fluid, the static state (identified by p and ρ) can be computed from the stagnation state (p_t, and a_t) and the Mach number Ma using the following algorithm:

- the stagnation density ρ_t is evaluated by reversing the function $a_t = a(p_t, \rho_t)$

- the stagnation enthalpy h_t and entropy s_t are evaluated by the direct evaluation of the thermodynamic relations $h_t = e(p_t, \rho_t) + p_t/\rho_t$ and $s_t = s(p_t, \rho_t)$
- solving the non linear system:

$$\begin{cases} h_t &= e(p,\rho) + \dfrac{p}{\rho} + \dfrac{1}{2}a^2(p,\rho)Ma^2 \\ s_t &= s(p,\rho) \end{cases}$$

  it is possible to determine the static state (p, and ρ), having h_t, s_t and M as parameters.

5.5.3 Subsonic outflow

In the case of subsonic outflow ($u < a$) two waves ($\lambda_2 = u$ and $\lambda_3 = u + a$) are directed outwards the physical domain while the third ($\lambda_1 = u - a$) inwards (see Fig. 5.10).

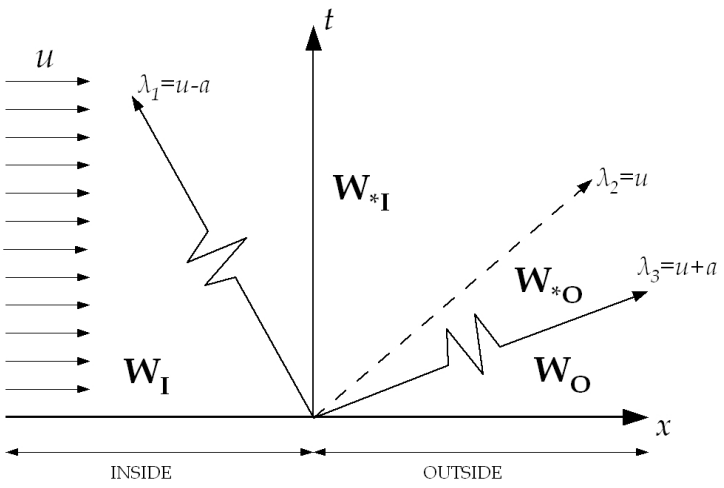

Figure 5.10: Schematic of the Riemann problem in case of subsonic inflow.

The inside state is known while the outside pressure p_O is assigned. To evaluate the interface solution some assumption are made:

- the wave $\lambda_1 = u - a$ is an expansion wave
- $p_{*I} = p_O$

These hypotheses are valid as long as the Riemann problem at the outflow interface is weak (that is, $\boldsymbol{W}_O \simeq \boldsymbol{W}_I$).

By using the relations of Sec. 5.4.2, the interface solution is evaluated as:

$$\begin{cases} \rho_{int} = \rho_{*I} = \rho_{*I}\left(\dfrac{p_O}{p_I}\right)^{1/\overline{\gamma}} \\ u_{int} = u_{*I} = u_I + \dfrac{a_I - a_{*I}}{\overline{\delta}} \\ p_{int} = p_{*I} = p_O \end{cases}$$

where $a_{*I} = a(p_{*I}, \rho_{*I})$ and $\overline{\gamma}$ and $\overline{\delta}$ are computed via Eq. (5.17) and Eq. (5.18), evaluated at the inside state I.

5.5.4 Subsonic inflow

In the case of subsonic inflow ($u < a$) two waves ($\lambda_2 = u$ and $\lambda_3 = u + a$) are directed inwards the physical domain while the third ($\lambda_1 = u - a$) outwards (see Fig. 5.11).

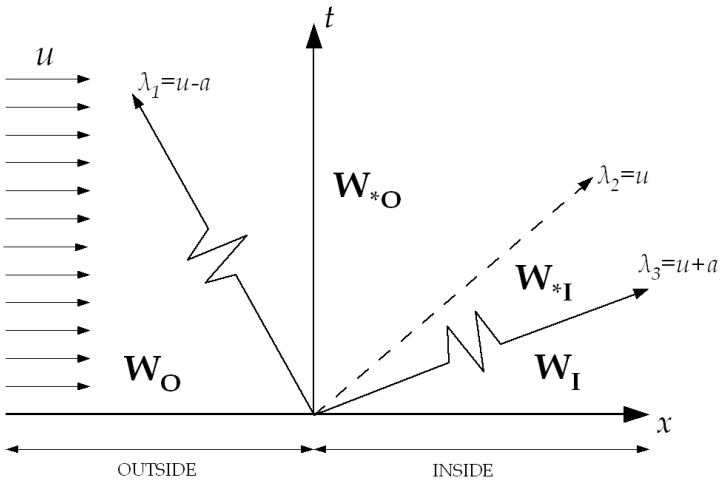

Figure 5.11: Schematic of the Riemann problem in case of subsonic outflow.

The inside state is known while the stagnation pressure p_t and stagnation speed of sound a_t are assigned as boundary conditions. As seen in Sec. 5.5.2 this im-

plies that the stagnation enthalpy h_t and entropy s_t are assigned. To evaluate the interface solution, some assumptions are made:

- the wave $\lambda_3 = u + a$ is an expansion wave
- the wave $\lambda_1 = u - a$ is adiabatic and isentropic (i.e., $h_{t,O} = h_{t,*O}$ and $s_{t,O} = s_{t,*O}$)

These hypotheses are valid as long as the Riemann problem at the outflow is weak (that is, $\boldsymbol{W}_O \simeq \boldsymbol{W}_I$).

By using the relations of Sec. 5.4.2, the following iterative algorithm must be employed to find the interface pressure $p_{int} = p_{*O}$:

1. a first trial value for p_{*O} is provided
2. $p_{*I} = p_{*O}$, that is the contact discontinuity $\lambda_2 = u$ relation
3. $\rho_{*I} = \rho_I \left(\dfrac{p_{*I}}{p_I} \right)^{1/\overline{\gamma}}$, that is the expansion wave $\lambda_3 = u + a$ relation
4. $u_{*I} = u_I + \dfrac{a_I - a_{*I}}{\overline{\delta}}$, that is the expansion wave $\lambda_3 = u + a$ relation
5. $u_{*O} = u_{*I}$, that is the contact discontinuity $\lambda_2 = u$ relation
6. ρ_{*O}, inverting the thermodynamic relation $s_t = s(p_{*O}, \rho_{*O})$
7. p_{*O} must satisfy the thermodynamic relation $h_t = h(p_{*O}, \rho_{*O}) + u_{*O}^2/2$; otherwise a new value for p_{*O} is provided and the procedure restarts from step 2

Once the convergence is reached, the interface solution is:

$$\begin{cases} \rho_{int} &= \rho_{*O} \\ u_{int} &= u_{*O} \\ p_{int} &= p_{*O} \end{cases}$$

5.6 Generic EOS

Using a conservative formulation of the governing equation implies that the generic equation of state must have density and pressure as independent variables:

$$T = T(\rho, p) \tag{5.22}$$

Having ρ and p as the independent thermodynamic variables is not a limitation since all the fluids of our interest can be modeled in that way. The only constraint lies in the limit case of perfect liquid (i.e., ρ =const). Expressions similar to Eq. (5.22) must be considered for the eEOS, μEOS, and kEOS (see Sec. 2.3 and 2.4). Moreover, since the Riemann solver (see Sec. 5.4) and the boundary conditions treatment (see Sec. 5.5) require the evaluation of other variables than temperature, specific internal energy, viscosity and thermal conductivity, more equations of state must be provided; these extra equations are: the specific heat at constant pressure EOS, the speed of sound EOS and the entropy EOS.

The thermodynamic properties of the generic fluid are stored in a database. The use of a database is necessary since the direct evaluation of the properties in a CFD code is impracticable because the time required to evaluate properties at one flow condition can be much larger than the time required to complete a single time step [50]. However the discretization of the thermodynamic properties must be performed efficiently and accurately; in fact, in subcritical/supercritical condition fluid properties change dramatically even for small density and pressure variations.

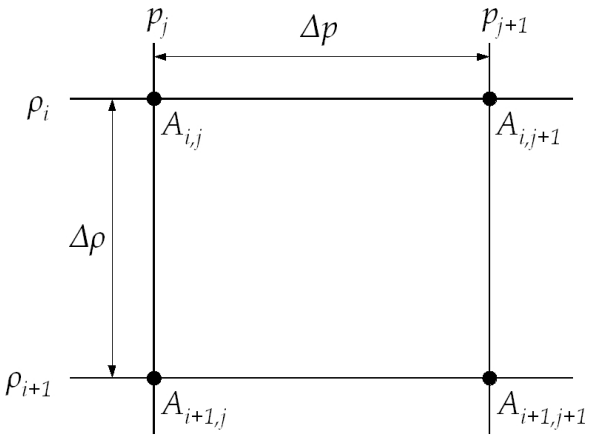

Figure 5.12: Schematic of the thermodynamic-database grid.

The database for the generic variable $A(p, \rho)$ is given by a two-dimensional grid with regular discretization Δp and $\Delta\rho$ (Fig. 5.12) where $A_{i,j}$ is the stored thermodynamic variable, which is computed from the equation of state $A = A(\rho, p)$:

$$A_{i,j} = A(\rho_i, p_j)$$

This kind of discretization permits to find the position i, j of the desired density $\overline{\rho}$ and pressure $\overline{p}$ in a direct and thus very efficient way:

$$\begin{cases} i &= \text{Int}\left(\dfrac{\overline{\rho} - \rho_{min}}{\Delta\rho}\right) \\ \\ j &= \text{Int}\left(\dfrac{\overline{p} - p_{min}}{\Delta p}\right) \end{cases}$$

where Int($\Re$) is the function that gives the integer part of the real number $\Re$ and ρ_{min} and p_{min} are the minimum value of density and pressure of the two-dimensional thermodynamic grid (i.e., $\rho_{min} = \rho_{i=0}$ and $p_{min} = p_{j=0}$). Once the position i, j is known, the sought value $\overline{A} = (\overline{p}, \overline{\rho})$ is given by a bilinear interpolation of the variable at positions $i, i+1, j, j+1$ (Fig. 5.13):

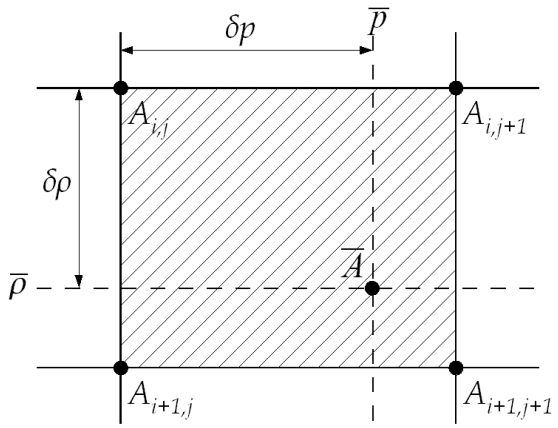

Figure 5.13: Schematic of the thermodynamic-database grid.

$$\overline{A} = a + b\ \ \delta\rho + c\ \ \delta p + d\ \ \delta\rho\,\delta p$$

where:

$$\begin{cases} a &= A_{i,j} \\ b &= \dfrac{A_{i+1,j} - A_{i,j}}{\Delta\rho} \\ c &= \dfrac{A_{i,j+1} - A_{i,j}}{\Delta p} \\ d &= \dfrac{A_{i,j} + A_{i+1,j+1} - A_{i+1,j} - A_{i,j+1}}{\Delta\rho\Delta p} \end{cases}$$

and

$$\delta\rho = \overline{\rho} - \rho_i \quad \text{and} \quad \delta p = \overline{p} - p_i$$

Since many polynomial form of the equation of state have the form $A = A(\rho, T)$ (such as the Van Der Waals and MBWR EOS), this function must be reverted to obtain an EOS with pressure and density as independent variables (i.e., such as Eq. (5.22)). The inversion can be made by an iterative method such as the Newton method. Since this operation is made apart from the CFD solver, this time consuming computation does not affect the efficiency of the CFD numerical solver.

5.7 Turbulence modeling

The turbulent flow is a flow regime which is characterized by strong fluctuations, both in time and in space, of velocity, temperature, pressure, etc. These fluctuations are chaotic, non stationary and three-dimensional since they occur both in the direction of the main flow than in the transversal directions. Eq. (5.6) can describe laminar flow as well as turbulent flow because it describes every scale of motion that characterizes the flow behaviour. The difference between laminar and turbulent flow is that the former is characterized by "large" scales only while the latter is characterized by both "large" and "small" scales. Moreover, the "small" scales of motion that characterize the turbulent flow cannot be neglected because they influence the average main flow (biggest scales of motion). In fact, the "small" scales transport and dissipate the energy of the main flow. Unfortunately, in case of turbulent flow, extremely fine computational grids are necessary to capture the smallest scales of motion and thus the computer resources do not suffice to describe the turbulent phenomena. This limitation of Eq. (5.6) relies on the fact that, in case of turbulent flow, the computational grid must have dimension proportional to Re^3 while in usual problems $Re = 10^6 - 10^9$. For that reason

a turbulence modeling to describe the macroscopic effect of the "small" scales is generally adopted while Eq. (5.6) describes the biggest scales (i.e., average main flow). This simplified approach is adopted considering the generic variable ϕ as composed by two part: a mean value $\overline{\phi}$ and a fluctuation (in time) ϕ':

$$\phi = \overline{\phi} + \phi'$$

where

$$\overline{\phi}(t) = \frac{1}{T}\int_{-T/2}^{+T/2} \phi(t+\tau)d\tau$$

and time T is much bigger than the period of turbulent fluctuations. The above decomposition is called Reynolds average modeling and the averaged Eq. (5.6) are called Reynolds Averaged Navier Stokes (RANS) equations. In case of compressible flow the Favre decomposition is used:

$$\phi = \widetilde{\phi} + \phi''$$

where

$$\widetilde{\phi}(t) = \frac{\overline{\rho\phi}}{\overline{\phi}} = \frac{1}{T}\frac{1}{\overline{\rho}}\int_{-T/2}^{+T/2} \rho\,\phi(t+\tau)d\tau$$

where $\widetilde{\phi}$ is the average value and ϕ'' is the fluctuation. Using this decomposition on Eq. (5.6), the governing equations are called Favre Averaged Navier Stokes (FANS) equations [51]. These equations present an additional term in the momentum and energy equation:

$$-\overline{\rho}\,\widetilde{u_i''u_j''} \quad \text{and} \quad \overline{\rho}\,\widetilde{u_j''h''}$$

called Reynolds stress tensor and Reynolds flux, respectively. These terms represent the macroscopic effect of the turbulent fluctuations (u_i'' and h'') which must be modeled using a proper turbulence model. Bussinesque supposed that the Reynolds turbulent terms can be related to the velocity and temperature gradients (as for the Newtonian-fluid law Eq. (5.3) and the Fourier's law Eq. (5.5)):

$$\begin{cases} -\ \overline{\rho}\,\widetilde{u_i''u_j''} = \mu_T\left(\dfrac{\partial\widetilde{u}_i}{\partial x_j} + \dfrac{\partial\widetilde{u}_j}{\partial x_i}\right) \\ \\ \overline{\rho}\,\widetilde{u_j''h''} = -\ k_T\dfrac{\partial\widetilde{T}}{\partial x_j} = -\dfrac{\mu_T\,c_p}{Pr_T}\dfrac{\partial\widetilde{T}}{\partial x_j} \end{cases}$$

where μ_T and k_T are the turbulent dynamic viscosity and thermal conductivity which can be related via the turbulent Prandtl number:

$$Pr_T = \frac{\mu_T \, c_p}{k_T}$$

where c_p is the specific heat at constant pressure; a reasonable value for Pr_T is 0.9. Differently from the molecular properties (μ and k), the turbulent dynamic viscosity and thermal conductivity are not properties of the fluid, since they are related to the flow behaviour and they can be much higher than the molecular properties: $\mu_T \gg \mu$ and $k_T \gg k$. For that reason turbulent flow is considerably different than laminar flow (in which $\mu_T = k_T = 0$).

The turbulence models that use the hypothesis of Bussinesque are called "eddy viscosity models" and they must provide a reasonable evaluation of the turbulent property μ_T (while k_T can be evaluated considering a constant value for Pr_T). The eddy viscosity model can be algebraic (also called "zero equation model") or can be described by one equation or two equations. A typical zero equation model is the Baldwin-Lomax model [4]; it has the advantage of a direct evaluation of the turbulent properties and thus it requires low computational cost. Two equations models are the $k - \varepsilon$ model [27] and $k - \omega$ model [52] in which two transport equations are employed: one to describe the behaviour of the turbulent kinetic energy k and one to describe the dissipation of the kinetic energy that occurs at the smallest scales of motion.

In the adopted numerical scheme the one-equation Spalart-Allmaras [46] turbulence model has been used. This one equation model affects the computational time much more than an algebraic model, but it was chosen because it is strictly "local" in the sense that the coefficients in the equations depend only on quantities that can be computed from the distance to the nearest wall and from the velocity field and its gradient in each point. This property is important when, as in the rectangular channel flow, geometrical configurations include more than a single wall. Zero equation models does not provide these advantages.

5.7.1 Spalart-Allmaras model

In the one-equation Spalart-Allmaras model [46] the kinematic turbulent viscosity $\nu_T = \mu_T/\rho$ is computed by a partial differential equation. In particular, this equation is a function of the intermediary variable $\widetilde{\nu}$ that is related to ν_T by:

$$\nu_T = \widetilde{\nu} \, f_{v1}(\chi)$$

where χ is the ratio between the two kinematic viscosities, $\chi = \widetilde{\nu}/\nu$, and f_{v1} is a damping function:

$$f_{v1}(\chi) = \frac{\chi^3}{\chi^3 + c_{v1}^3}$$

The constant c_{v1} is set equal to 7.1.

The partial differential equation that describes the behaviour of the intermediary variable $\widetilde{\nu}$ is:

$$\frac{D\widetilde{\nu}}{Dt} = b_{prod}(S, \widetilde{\nu}, d) - b_{dest}(\widetilde{\nu}, d) + \frac{1}{\sigma}\left[\nabla \cdot ((\nu + \widetilde{\nu})\nabla\widetilde{\nu}) + c_{b2}\left(\nabla\widetilde{\nu}\right)^2\right] \quad (5.23)$$

where S is the modulus of the vorticity, d is the distance from the wall and σ is set equal to $2/3$. The last term of Eq. (5.23) is the diffusion term and the constant c_{b2} is calibrated to 0.662. The functions b_{prod} and b_{dest} describe the production and destruction of the turbulent viscosity. In the Spalart-Allmaras model, the production of turbulent viscosity is related to the vorticity. This is a good assumption for the flow close to the wall.

The production function is:

$$b_{prod} = c_{b1}\,\widetilde{S}\,\widetilde{\nu}$$

where

$$\widetilde{S} = S + \frac{\widetilde{\nu}}{\kappa^2 d^2} f_{v2}(\chi)$$

and f_{v2} is a second damping function:

$$f_{v2}(\chi) = 1 - \frac{\chi}{1 + \chi f_{v1}(\chi)}$$

and κ is the Von Karman constant ($\kappa = 0.41$). The calibration constant c_{b1} is set equal to 0.135.

The destruction function is directly related to the wall distance d:

$$b_{dest} = c_{w1} f_w(r) \left(\frac{\widetilde{\nu}}{d}\right)^2$$

where r is a characteristic length:

$$r = \frac{\widetilde{\nu}}{\widetilde{S}\kappa^2 d^2}$$

and the function $f_w(r)$ is:

$$f_w(r) = g(r)\left[\frac{1 + c_{w3}^6}{g^6(r) + c_{w3}^6}\right]^{1/6}$$

where:

$$g(r) = r + c_{w2}\left(r^6 - r\right)$$

The calibration constants are:

$$\begin{aligned} c_{w1} &= \frac{c_{b1}}{\kappa^2} + \frac{1 + c_{b2}}{\sigma} \\ c_{w2} &= 0.2 \\ c_{w3} &= 2 \end{aligned}$$

where c_{w1} has been chosen to balance the production and destruction term.

Since a finite volume numerical scheme has been adopted, the turbulence equation Eq. (5.23) must be written in the "conservative law" form (i.e., integral form for a fixed volume):

$$\frac{d}{dt}\int_{\overline{\mathcal{V}}} \widetilde{\nu}\, dV + \oint_{\overline{\mathcal{S}}} \boldsymbol{E}^{SA} dS - \oint_{\overline{\mathcal{S}}} \boldsymbol{R}^{SA} dS - \int_{\overline{\mathcal{V}}} \boldsymbol{G}^{SA} dV = \int_{\overline{\mathcal{V}}} \boldsymbol{H}^{SA} dV$$

where $\boldsymbol{G}^{SA}$ (expressed in non-conservative form) and $\boldsymbol{R}^{SA}$ (expressed in conservative form) are the diffusion terms, $\boldsymbol{E}^{SA}$ (expressed in conservative form) is the convective term and $\boldsymbol{H}^{SA}$ is the production term (it is a source term expressed in non-conservative form):

$$\begin{aligned} \boldsymbol{G}^{SA} &= \frac{c_{b2}}{\sigma}\left(\nabla\widetilde{\nu}\right)^2 \\ \boldsymbol{R}^{SA} &= \frac{\nu + \widetilde{\nu}}{\sigma}\nabla\widetilde{\nu}\cdot\boldsymbol{n} \\ \boldsymbol{E}^{SA} &= \widetilde{\nu}\left(\boldsymbol{u}\cdot\boldsymbol{n}\right) \\ \boldsymbol{H}^{SA} &= b_{prod}(S, \widetilde{\nu}, d) - b_{dest}(\widetilde{\nu}, d) \end{aligned}$$

The above equation can be integrated as seen in Sec. 5.3.

Chapter 6

Validation

With advances in computing power, engineers increasingly rely on modeling and simulation for the design, analysis, and certification of engineering systems. Validation provides the primary means by which the overall accuracy of computational simulations can be assessed. Validation can be separated into two parts, code validation and solution validation. Code validation is used to find coding errors in the discrete solution to a given set of governing equations and boundary conditions. Code validation can be assessed by comparison to exact analytical solutions, comparison to highly accurate numerical benchmark solutions, and code-to-code comparisons. Solution validation (or numerical error assessment) is concerned with quantifying the numerical error of a given simulation. Solution validation should be performed for each application of the code that is significantly different than previous applications. For steady-state problems, the two main aspects of solution validation are iterative convergence and grid convergence. The former deals with the marching of a solution in pseudo-time toward a steady-state, whereas the latter addresses the adequacy of the mesh on which the discrete equations are being solved. The spatial order of accuracy is also an important metric for assessing the errors due to spatial resolution.

In this chapter, code validation and solution validation have been performed on two-dimensional turbulent test cases for both perfect gas and supercritical fluid. Solution verification has been achieved by an analysis of iterative convergence and grid convergence (for both perfect gas and supercritical fluid). These solutions have been compared with analytical solution, thus providing the validation of the code. At last, the code has been also validated by means of literature solution concerning a two-dimensional channel flow that presents some topics of the "actual" three-dimensional flow in cooling channels (such as supercritical fluid and strong wall temperature gradient).

6.1 Turbulent flat plate: perfect gas

In Chap. 5 a finite volume numerical scheme able to treat a general fluid described by a tabular EOS has been presented. The numerical scheme has been implemented on an pre-existing home-made finite volume numerical tool for perfect gas [16].

In this section we want to demonstrate the grid convergence and to compare the numerical solution with analytical solution for the original code, that is, perfect gas case with the EOS considered in the analytical close form. The numerical test case considered here is the low-Mach number turbulent flow on a flat plate for Reynolds number (based on the flat plate length) $Re = 10^7$. The considered fluid is the air treated as a perfect gas. The computational domain is a rectangle whose length is 3, width is 1 and the leading edge is 1.5 dimensionless units from the inlet section (Fig. 6.1). The no-slip condition is applied to half length of the lower side while the symmetry condition to the remaining part.

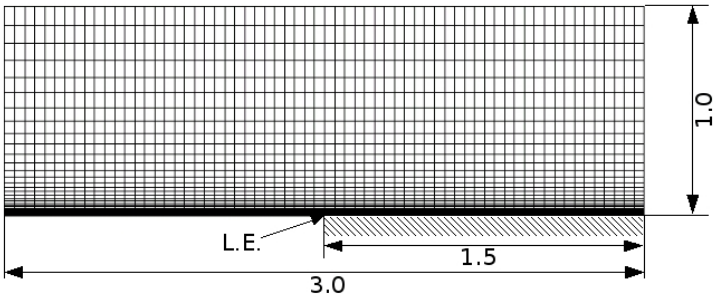

Figure 6.1: Computational mesh in dimensionless units.

The subsonic inflow is characterized by the stagnation pressure $p_0 = 1.02828\,bar$ and the stagnation speed of sound $a_0 = 348.57\,m/s$ (that is, $T_0 = 302.4\,K$) while the subsonic outflow is characterized by the static pressure $p = 1\,bar$. As a consequence, the flow far from the wall has a Mach number $Ma = 0.2$. Finally, the wall of the flat plate is adiabatic.

The numerical solutions were computed on three grid levels, the finest mesh being 64x64. The medium and coarse levels were obtained by removing every other vertex from the previous finer level, that is grid halving. The cells are clustered to the wall using a hyperbolic function in the whole boundary layer. The law parameters are set to yield a fine mesh width Δy_{min} at the wall and Δy_{max} in the far field. More details about the meshes used are reported in Tab. 6.1.

nxm mesh	64x64 (fine mesh)	32x32 (medium mesh)	16x16 (coarse mesh)
Δy_{min}	$0.5\ 10^{-5}$	$1.1\ 10^{-5}$	$2.7\ 10^{-5}$
Δy_{max}	0.087	0.173	0.340

Table 6.1: Characteristic data of meshes, in dimensionless units.

The dimensional lengths can be assessed by imposition of the Reynolds number ($Re = 10^7$). For these flow conditions the unit non-dimensional length is equal to $1.5\ m$ and thus, for example, Δy_{min} of the finest mesh (64x64) is $7.5\ \mu m$.

The qualitative convergence behaviour for the dimensionless velocity profile in a selected test section is reported in Fig. 6.2. This section, which is located at 1.3125 unit from leading edge, is far enough from the leading edge to consider the local flow sufficiently non affected by the leading edge effects and thus the existence of a similar non-dimensional velocity profile is guaranteed.

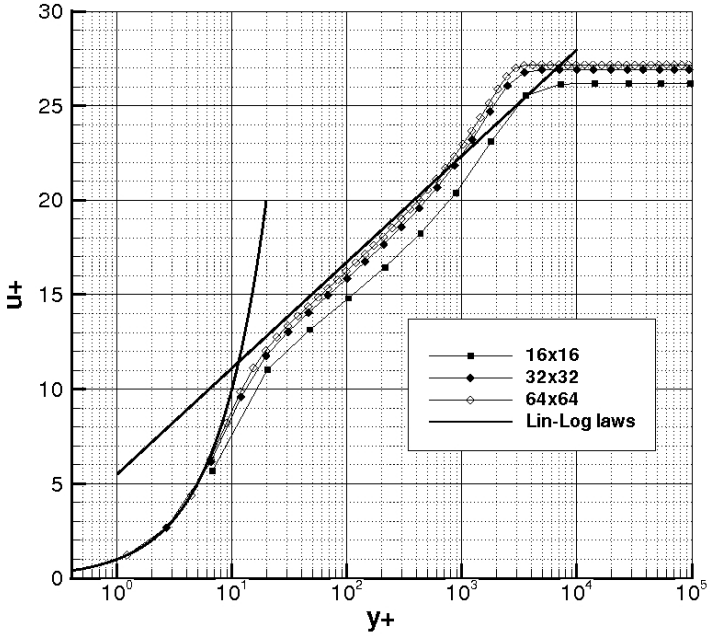

Figure 6.2: Numerical and exact-analytical solution for the turbulent boundary layer.

The non-dimensional velocity profile is a similar solution that occurs in turbu-

lent boundary layer along a flat plate and for a compressible fluid, i.e. $\rho = const$, (see [29] for more details). The present test case has been performed for an incompressible fluid, i.e. $\rho \neq const$ but, as a matter of fact, a low-Mach number flow is almost a constant-density flow, i.e. $\rho \simeq const$. As a consequence, the obtained solutions can be compared with the incompressible turbulent velocity profile.

The similar solution can be achieved if velocity and transversal axis (y-axis) are related to the *friction velocity*:

$$u^* = \sqrt{\frac{\tau_w}{\rho}}$$

and the characteristic length

$$y^* = \frac{\nu}{u^*}$$

where τ_w is the skin friction at wall and ν is the kinematic viscosity.

In the laminar sublayer, that is the layer close to the wall in which, due to the law velocity, the turbulent viscosity can be neglected, the dimensionless velocity profile is:

$$u^+ = y^+ \quad \text{for} \quad y^+ \leq 7$$

where u^+ and y^+ are the dimensionless velocity and length. This solution is called *linear law*.

Sufficiently far from the wall, the turbulent viscosity is much superior than the molecular viscosity. As a consequence, molecular viscosity can be neglected and the dimensionless velocity profile is:

$$u^+ = \frac{1}{\kappa} \ln (y^+) + B \quad \text{for} \quad y^+ \geq 30$$

where κ is the Von Karman constant ($\kappa = 0.41$) and the coefficient B is set equal to 5.5. This solution is called *logarithmic law*.

Fig. 6.2 exhibits a good agreement between the exact-analytical solution and the numerical solution. Moreover, numerical solution converges to the exact solution asymptotically, that is, as grid is refined the error between the numerical solution and the continuum solution decreases. These results, good approximation of the exact solution and asymptotic grid convergence, guarantee both solution and code validation.

Now we want to provide a quantitative estimation of the grid convergence error. This estimation can be computed by means of the Richardson extrapolation [40]. The Richardson extrapolation procedure is a technique in which three discrete solutions on different grid levels are used to obtain a solution extrapolated to the zero mesh size. These Richardson extrapolated values can be used as a more

accurate solution, or more important, as an approximation to the exact continuum solution, which can then be used to obtain error estimates in the discrete solutions. The underlying assumption in the Richardson extrapolation procedure is that the discrete solution f on a mesh level k have a single dominant error term of order p, that is:

$$f_k = f_{exact} + g_p h_k^p + \mathcal{O}(h_k^{p+1}) \tag{6.1}$$

where f_{exact} is the exact continuum solution, g_p is the coefficient of the p-th order term and h_k is some measure of the grid spacing on mesh level k. Validation of the numerical code can be assessed if the order p approximates the spatial order of accuracy of the numerical scheme. When three discrete solutions with a constant grid refinement factor ($r = h_2/h_1 = h_3/h_2$) are used, the system of equations found from the above equation can be solved for the order of accuracy to give the following relationship:

$$p = \frac{\ln \varepsilon_{32}/\varepsilon_{21}}{\ln r}$$

where ε_{21} and ε_{32} represent differences between the discrete solutions:

$$\varepsilon_{21} = f_2 - f_1 \quad \text{and} \quad \varepsilon_{32} = f_3 - f_2$$

Finally, an extrapolated estimation of the exact solution can be given by:

$$f_{exact} = \frac{r^p f_1 - f_2}{r^p - 1}$$

The required condition for applying general Richardson-type extrapolation is that the grids are sufficiently refined to be in the asymptotic grid convergence range, that is, the higher-order term in the Eq. 6.1 is small. Since numerical solutions were obtained for three grid refinement levels by grid halving, from mesh 1 (64x64, fine mesh) to mesh 3 (16x16, coarse grid), the refinement factor is $r = 2$.

The quantitative convergence behaviour for the skin friction coefficient C_f in the selected test section is reported in Table 6.2.

$C_{f,16x16}$	0.2693
$C_{f,32x32}$	0.2526
$C_{f,64x64}$	0.2493
$C_{f,extra}$	0.2485
p	2.3342

Table 6.2: C_fx100 and measured order of accuracy p at $x = 1.3125$.

It is evident that the numerical solutions are in the asymptotic range and that the measured order of accuracy of the numerical solution is close to the formal order of accuracy of the numerical scheme ($p_{formal} = 2$).

Note that, in order to compute the order of accuracy and the extrapolated estimation of the exact solution, the point value of the solution at each level was interpolated on the vertex of the coarsest grid by means of a bilinear interpolation (note that, the scheme being cell centered, the control points for different grid levels do not coincide). This operation affects the numerical solution by a second-order error term whose coefficient is the same for each grid size; therefore this interpolation does not corrupt the accuracy of the numerical solution.

Analysis of the spatial order of accuracy is a good evidence of the solution validation, even if iterative convergence analysis should be also provided. The standard method for assessing iterative convergence is to monitor the $L2$ norms of the residuals for the governing equations over the entire domain. The residuals should approach zero as iterative convergence is achieved.

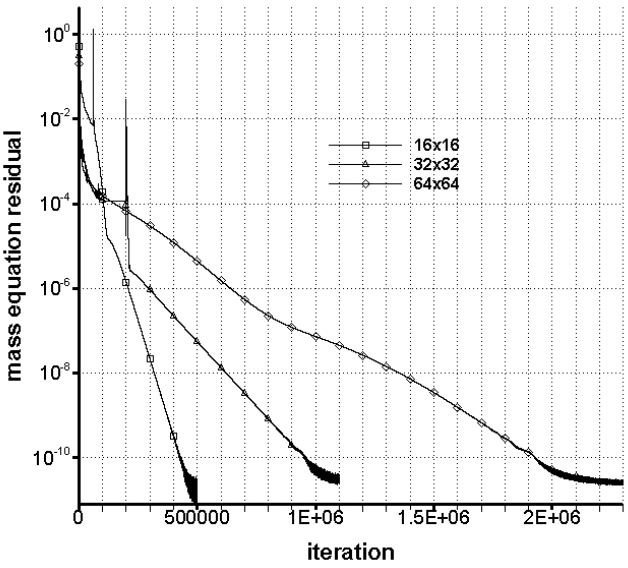

Figure 6.3: Mass equation residual for the three mesh refinements.

A solution can be considered fully iteratively converged, within the precision of the computer used, when the residuals are reduced to machine zero (approximately 15 orders of magnitude for a double-precision computer). However, the practice of monitoring iterative convergence does not necessarily provide information on the iterative error in a given flowfield quantity but the reduction of

the residuals to machine zero provides confidence that the iterative errors in the solution variables are small. Furthermore, for engineering calculations, it is not always necessary, or even possible, to converge the solution to machine zero.

The iterative convergence behaviour for the three mesh refinements is presented in Fig. 6.3 for the mass equation residual defined by:

$$\frac{1}{N}\sum_{i=1}^{N}\left|\frac{\rho^{n+1}-\rho^{n}}{t^{n+1}-t^{n}}\right|$$

where the sum in the above relation is extended over the entire finite volumes N of the grid and n is the generic iteration in the pseudo-time t. For this test case the mass equation residual has been reduced by approximately 12 orders of magnitude on all grid levels and it converges to machine zero by approximately 500000 iterations for coarsest grid and 2000000 for finest grid. The larger number of iterations for this downstream location is indicative of the hyperbolic nature of the problem.

6.2 Effect of the EOS discretization

In this section we want to demonstrate that the finite volume numerical scheme for a generic fluid described in Chap. 5, reproduces the perfect gas case as accurately as the pre-existing numerical tool for perfect gas [16]. As a matter of fact, this comparison is a code-to-code comparison and thus it is an important assessment in demonstrating that the numerical method presented in Chap. 5 is well formulated and that its implementation has been performed without relevant coding errors. Moreover, since the EOS must be provided in a tabular form having density and pressure as independent variables (see Sec. 5.6), the code-to-code comparison will also give an estimation of the error introduced by the discretization of the equations of state.

The code-to-code comparison has been performed on the same two-dimensional turbulent flat plate flow presented in Sec. 6.1, using the medium size mesh 32x32. Three numerical solutions have been performed, each one characterized by a different discretization of the EOS (see Tab. 6.3).

Density discretization step is refined from EOS mesh 1 ($\Delta\rho = 0.10\ kg/m^3$) to EOS mesh 3 ($\Delta\rho = 0.01\ kg/m^3$) while pressure discretization step is fixed ($\Delta p = 2000\ Pa$). We decided to focus on density discretization only because the exact solution of the flat plate flow is $p = const$ and thus pressure discretization affects the numerical solution in a minor way.

The dimensional velocity profiles in the test section (Sec. 6.1) for the three tabular-EOS solutions and the analytical-EOS solution are shown in Fig. 6.4.

EOS mesh	$\Delta\rho\ [kg/m^3]$	$\Delta\rho/\rho$	$\Delta p\ [Pa]$	$\Delta p/p$
1	0.10	8.6%	2000	2%
2	0.05	4.3%	2000	2%
3	0.01	0.9%	2000	2%

Table 6.3: Density and pressure discretization step for the computed solution and their percentage value with respect to the flat-plate, low-Mach solution: $p = 1\ bar$, $\rho \simeq 1.16\ kg/m^3$.

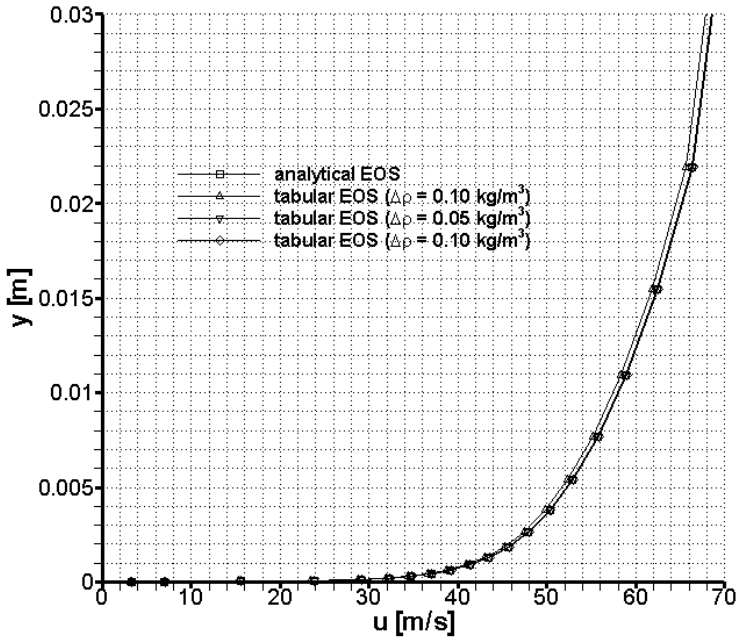

Figure 6.4: Velocity profiles at the test section, for the tabular-EOS solutions and the analytical-EOS solution.

Differences between these solutions are almost not discernible from Fig. 6.4. However, the error of the tabular-EOS solutions with respect to the analytical EOS solution is not negligible; for example at the height $y = 7.5\ 10^{-5}\ m$ the velocity errors are summarized in Tab. 6.4.

EOS mesh	velocity error
1	1.3%
2	0.4%
3	0.3%

Table 6.4: Velocity percentage error with respect to the analytical-EOS solution, in the test section and height $y = 7.5\ 10^{-5}\ m$.

Concerning the skin friction coefficient, its error with respect to the analytical-EOS is reported in Tab. 6.5.

EOS mesh	C_f error
1	0.12%
2	0.06%
3	0.03%

Table 6.5: C_f percentage error with respect to the analytical-EOS solution, in the test section.

The C_f error is very small since a discretization density step $\Delta\rho/\rho$ of 8.6% (mesh 1) produces a 0.12% error in the skin friction coefficient. This little influence of the EOS table discretization on the numerical solution (with special regard to the wall variables) is very promising and thus wall parameters (such as skin friction and heat transfer coefficient) can be computed with enough confidence for engineering applications. However, the discretization of the thermodynamic properties must be performed accurately, especially in the transcritical fluid condition since fluid properties change dramatically (and often they present a peak value) even for small density and pressure variations.

6.3 Turbulent flat plate: supercritical fluid

In Sec. 6.2 the present numerical code has demonstrated the capability to describe a perfect gas flow (described by means of a tabular EOS) within the same accuracy of solution obtained by means of standard numerical tool (i.e., tools using the analytical perfect gas EOS). Now we want to validate the numerical code and

the solution in the case of supercritical fluid (i.e., high density fluid). In particular, we will demonstrate that the present numerical code maintains the formal spatial order of accuracy (i.e., 2^{nd} order) even in the case of supercritical fluid and that the obtained solution well approximates the analytical solution. These results will be achieved using the same analysis (Richardson extrapolation and comparison with incompressible analytical solution) and the same geometrical test case (two-dimensional flat plate) already seen in Sec. 6.1. Moreover, similarly to the cited test case, a low Mach number turbulent flow on a flat plate with a Reynolds number $Re = 10^7$ has been considered. The fluid is the methane described by the equation of state presented in App. C. Since the Reynolds number is the same of the test case presented in Sec. 6.1, the dimensionless geometry of meshes remains unchanged (see Tab. 6.1). The subsonic inflow is characterized by the stagnation pressure $p_0 = 80\ bar$ and the stagnation speed of sound $a_0 = 440\ m/s$ (that is, $T_0 = 300\ K$) while the subsonic outflow is characterized by the static pressure $p = 77.78\ bar$. As a consequence, the flow far from the wall has a Mach number $Ma = 0.2$. Finally, the wall of the flat plate is adiabatic. Imposing the Reynolds number $Re = 10^7$ for this flow conditions, the unit non-dimensional length is equal to $17.2\ mm$; for example Δy_{min} of the finest mesh (64x64) is $0.086\ \mu m$.

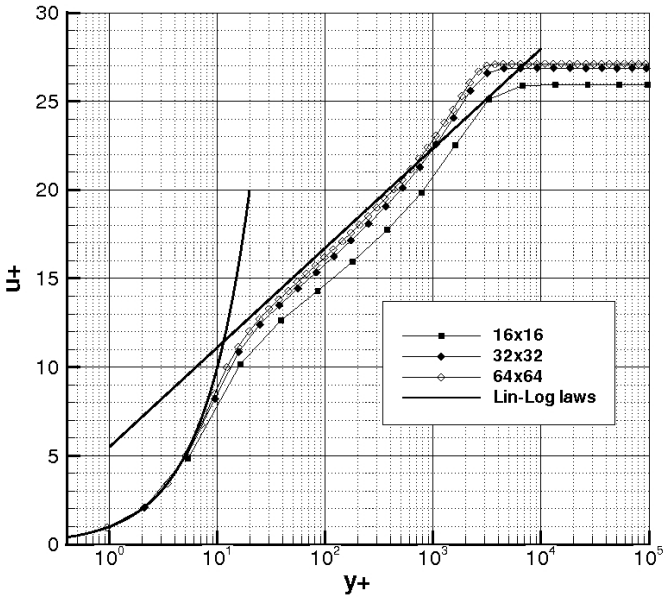

Figure 6.5: Numerical and exact-analytical solution for the turbulent boundary layer.

The qualitative convergence behaviour for the dimensionless velocity profile in the selected test section (located at 1.3125 unit from the leading edge) is reported in Fig. 6.5. This figure exhibits a good agreement between the exact-analytical solution for the incompressible flow and the numerical solution. Moreover, numerical solution converges to the exact solution asymptotically. These results guarantee both solution and code validation for the supercritical high-density flow regime and thus give confidence on the results presented in the next chapter.

Al already see in Sec. 6.1, a quantitative estimation of the grid convergence error is given by Richardson extrapolation procedure applied to the skin friction coefficient C_f (see Tab. 6.6).

$C_{f,16x16}$	0.2765
$C_{f,32x32}$	0.2559
$C_{f,64x64}$	0.2505
$C_{f,extra}$	0.2485
p	1.9200

Table 6.6: C_fx100 and measured order of accuracy p at $x = 1.3125$.

It is evident that the numerical solutions are in the asymptotic range and that the measured order of accuracy of the numerical solution is close to the formal order of accuracy of the numerical scheme ($p_{formal} = 2$). To reduce to a minimum influence the effect of the EOS discretization on the numerical solution, the EOS have been discretized with a very high accuracy: $\Delta\rho/\rho = 0.03\%$ and $\Delta p/p = 0.05\%$.

6.4 2D channel test case

In this section we want to validate the present numerical tool using literature solutions concerning two-dimensional channel flow that presents some topics of the "actual" three-dimensional flow in cooling channels (such as supercritical fluid and strong temperature gradients). This validation has been performed using the CFD results presented for a 2D test case by Wennerberg et al. [49]. In the literature it is not easy to find numerical or experimental solutions of real fluid in a channel with a strong wall temperature gradient. The test case concerns two-dimensional flow with asymmetric heating as shown in Fig. 6.6: the cold wall is adiabatic, while the hot is at $T = 900\ K$. The duct has a length to height ratio $L/D = 50$ and the flow Reynolds number based on D is 42000. An inviscid wall is assumed before the channel entry, in order to have the same boundary conditions provided in Ref. [49]. The considered fluid is the supercritical nitrogen,

its inlet temperature is $152.8\ K$ and its inlet pressure is $7.6\ MPa$ (note that the nitrogen critical point is $T_c = 126.5\ K$ and $p_c = 3.399\ MPa$).

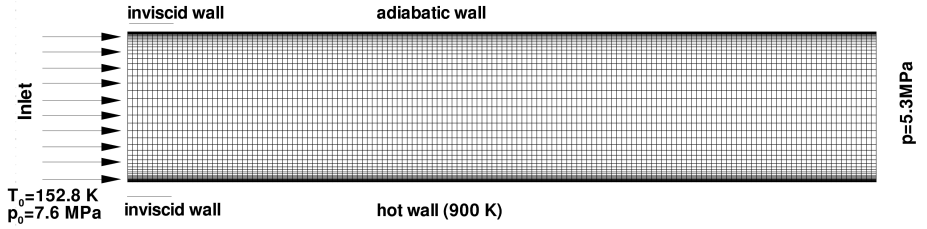

Figure 6.6: Geometry and boundary conditions for asymmetrically heated two-dimensional channel flow (the plot is not in scale: channel height is enlarged 10 times with respect to channel length).

Unfortunately some data necessary to reproduce the test case are not available. In particular, the exit pressure and the equation of state used for supercritical nitrogen are not provided in Ref. [49]. For that reason the validation has been performed only on a quality level, assuming an exit pressure of $5.3\ MPa$ which has been chosen on the basis of the exit velocity profiles presented in Ref. [49]. Moreover, a channel height of $0.035\ mm$ has been obtained from Reynolds number and the inlet density and viscosity. For the present computations both the Van Der Waals equation of state and a fictitious perfect gas law are assumed for the supercritical nitrogen. The computational grid is made of 151(stream direction) x 64(cross direction) volumes, which are clustered toward the walls to accurately describe the turbulent boundary-layers.

The results obtained for both perfect gas and supercritical fluid assumption are shown in Fig. 6.7 and Fig. 6.8. In particular, the exit velocity and temperature profiles are shown in Fig. 6.7 where also results of Ref. [49] are shown for the sake of comparison. The present code well reproduces the reference velocity profiles (both for perfect gas and real fluid) and the temperature profile, showing the typical velocity peak near the hot wall caused by the expansion of the heated fluid.

The Mach number and density profiles on the channel centerline (both for perfect gas and real fluid) are shown in Fig. 6.8. A maximum difference of 5% in the Mach number between the present and reference simulations is probably due to the uncertain inlet/outlet conditions, while the large differences on the density

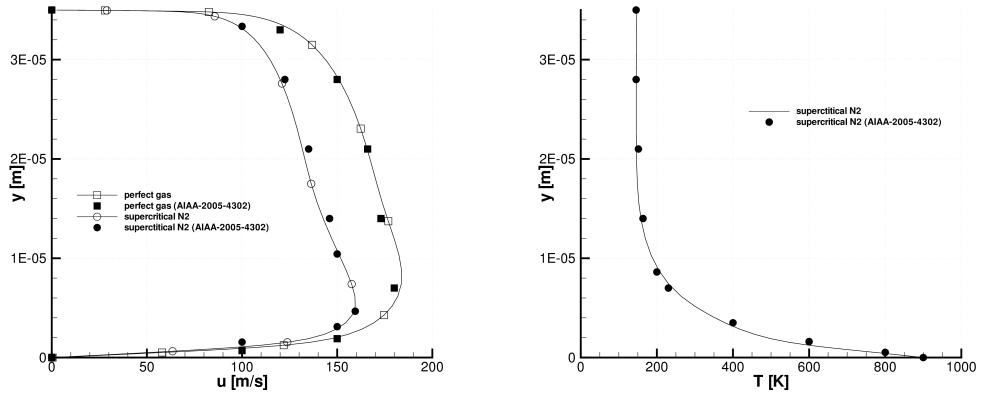

(a) Velocity profiles at channel exit for supercritical nitrogen and perfect gas.

(b) Temperature profile at channel exit for supercritical nitrogen.

Figure 6.7: Comparison between the present computations and the results published in Ref. [49].

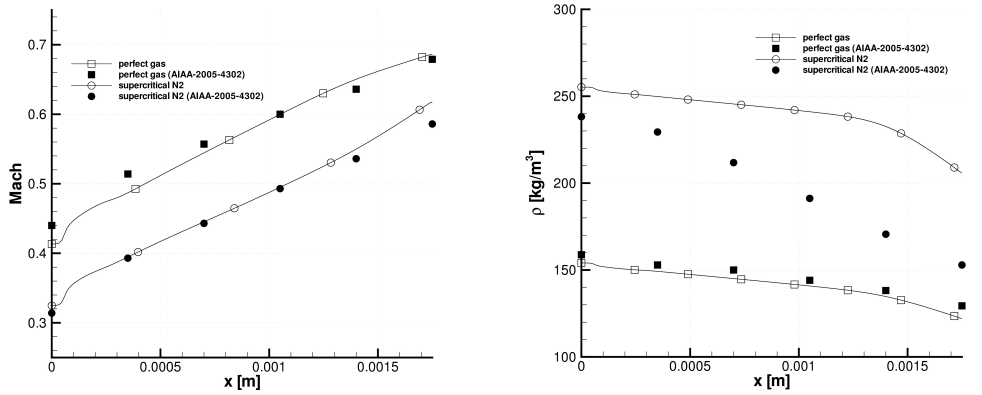

(a) Mach number profiles on channel centerline for real fluid and perfect gas.

(b) Density profiles on channel centerline for real fluid and perfect gas.

Figure 6.8: Comparison between the present computations and the results published in Ref. [49].

profile of the real fluid is due to the inaccuracy of the Van Der Waals equation of state; in fact the density profiles for the trivial case of perfect gas are in good accuracy. Moreover, the density error of the Van Der Waals equation with respect to the online NIST database [2] in the nitrogen supercritical range can be as large as 30%.

Chapter 7

3D results

In this chapter, three-dimensional straight channel flow is analyzed using the CFD code presented in Chap. 5 and 6. The selected working fluid is the methane in its subcritical/supercritical thermodynamic state; more precisely, pressure is supercritical while temperature is transcritical. This is the typical methane flow regime in cooling channel (see Sec. 2.5.1). Many computations with different inflow conditions (in terms of stagnation pressure and temperature) and wall temperature distribution have been performed in order to analyze their effect on coolant flow behaviour (velocity field, temperature stratification, etc.) and on coolant performances (pressure loss, wall heat flux, etc.). Moreover, the aspect ratio effect has been analyzed considering different aspect ratios (from 1 to 8) for each test case.

7.1 Test cases description

To show the channel aspect ratio effect, four different cross section geometries have been considered. More precisely, the channel sections have the same area while the base and the height are varied in order to get different aspect ratios: 1, 2, 4, and 8. The channel area is kept constant with the intent on comparing flows with the same mass flow rate if the inflow, outflow, and wall boundary conditions are kept constant. Obviously this intent is not fulfilled since the aspect ratio has a strong effect on the skin friction and heat flux affecting the flow and thus has a strong effect on the entering mass flow rate. However, the choice to have constant cross sectional area seems to be appropriate as it permits to compare cooling systems with the same weight (see Sec.3.6).

The cross sectional area is $A = 0.08\ mm^2$ and the length of the channels, which is constant for all test cases, is $L = 30\ mm$. Since $\sqrt{A}/L \simeq 100$ it is possible to say that the channel is long enough to ensure that, sufficiently far from the inlet section, the flow is fully developed. This means that the flow is

not affected by the inlet configuration (in case of rocket engine applications, it is the type of connecter between coolant manifold and cooling channels). The dimensions of the four channel geometries are summarized in Tab. 7.1.

AR	$A\ [mm^2]$	$L\ [mm]$	$b\ [mm]$	$h\ [mm]$
1	0.08	30	0.2828	0.2828
2	0.08	30	0.2	0.4
4	0.08	30	0.1414	0.5657
8	0.08	30	0.1	0.8

Table 7.1: Channel dimensions (in terms of cross area A, length L, base b, and height h) for the selected aspect ratios.

Channel dimensions are much smaller than in actual application; in fact, the height of a "real" cooling channel with high aspect ratio (that is $AR > 4$) is typically around $1\ cm$ while in our computations the maximum height is ten times smaller. Small dimensions have been selected with the intent on reducing the flow Reynolds number (based on the hydraulic diameter) to one order of magnitude. In fact the high Reynolds number of the actual rocket engine cooling channels (up to $4 \cdot 10^6$ in case of hydrogen channel flow [14]) represents a computational challenge because of the very thin boundary layers, thus requiring extremely fine grids and long computation times [50]. To avoid these difficulties, without loosing sight of the main phenomena that occur in cooling channels, the dimensions of the channel have been selected so that the maximum Reynolds number is $3 \cdot 10^5$. However, the computed channel flows show many features of the "real" cooling passages: high aspect ratio of the cross section (defined "high" when greater than 4), high wall temperature differences that induce thermal stratification, and realistic flow conditions (supercritical pressure and transcritical temperature). Six test cases have been considered: three having the same inlet stagnation pressure while inlet stagnation temperature varies and three having the same inlet stagnation temperature while inlet stagnation pressure varies. Exit pressure is the same for the six test cases. Concerning wall temperature distribution, on the hot side (that is the bottom wall) the imposed wall temperature is $600\ K$ (for all test cases), while on the cold side (that is the top wall) the imposed wall temperature is equal to the stagnation inlet temperature of the coolant. Then a linear distribution of temperature is imposed on the side wall to simulate the fin effect. The boundary conditions for the six test cases are summarized in Tab. 7.2. Note that the cold side wall temperature is equal to the stagnation inlet temperature to simulate the adiabatic wall condition of the "real" cooling channels. In fact, to avoid a discontinuity of the wall temperature distribution, the direct imposition of the adiabatic

wall condition on the top wall has not been considered. As a consequence of this choice, a non-zero heat flux is present on the top wall.

Test Case	$p_{0,in}\ [bar]$	$T_{0,in}\ [K]$	$p_{exit}\ [bar]$	$T_{w,cold}\ [K]$	$T_{w,hot}\ [K]$
1	90	220	70	220	600
2	90	183	70	183	600
3	90	130	70	130	600
4	90	180	70	180	600
5	100	180	70	180	600
6	110	180	70	180	600

Table 7.2: Boundary conditions for the six test cases.

Every geometric configuration is characterized by a three-dimensional computational grid composed by NxMxL volumes in order to discretize the coolant flow along the base (N volumes), the height (M volumes) and the length (L volumes) of the channel. Since the flow is symmetric with respect to the vertical centerplane, only one-half of the physical domain is discretized and a symmetric flow condition is imposed as boundary condition on the channel centerplane. The NxMxL volumes are clustered near the walls to accurately describe the turbulent boundary layers (i.e., the non-dimensional parameter y^+ at wall must be of order 1). The mesh distribution of the four geometric configurations are shown on Fig. 7.1 and their computational dimensions are summarized in Tab. 7.3.

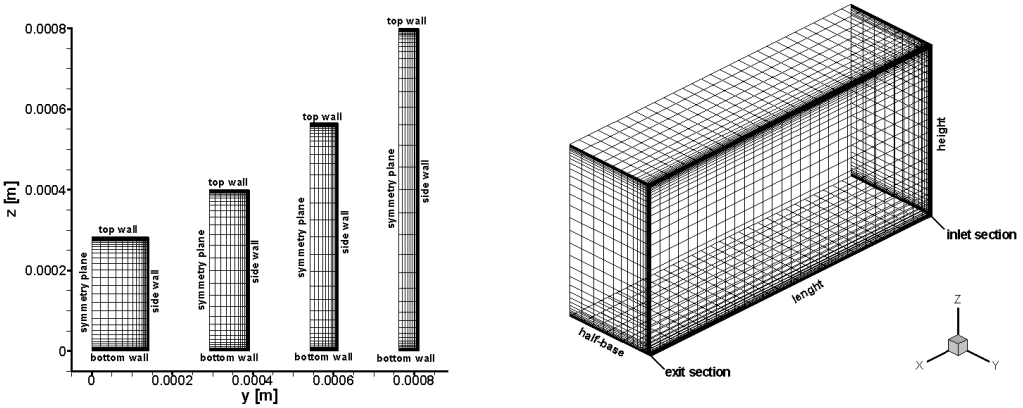

(a) Cross sectional meshes of the four channel configurations.

(b) 3D mesh of the generic channel configuration (the figure is not in scale).

Figure 7.1: Computational meshes schematic.

AR	$N/2$ (base)	M (height)	L (length)
1	25	50	30
2	24	50	30
4	22	54	30
8	20	60	30

Table 7.3: Number and distribution of the volumes used to discretize the four channel configuration.

7.2 Flow description

In this section the flow behaviour of the methane inside cooling channel is described. This description is based on test case 3 with particular regard to the highest aspect ratio configuration (that is, AR$=8$). This test case is of great interest since flow conditions reproduce the real methane working conditions in rocket cooling channels (see Sec. 2.5.1). In fact, methane enters the channel having a supercritical stagnation pressure $p_{0,in} = 90\ bar$ and a subcritical stagnation temperature $T_{0,in} = 130\ K$ while wall temperature ranges from $600\ K$ at the hot-side to the nearly adiabatic value $130\ K$ at the cold-side.

The peculiar three-dimensional behaviour of the flow is shown by pressure, temperature, density, streamwise velocity, specific heat at constant pressure, speed of sound, compressibility factor and Mach number fields in Fig. from 7.2 to 7.9. These figures show the evolution of the variables at different sections, from the inlet toward the exit, which are located every $5\ mm$ along the channel streamwise direction.

Methane enters the channel in a subcritical liquid-like state (its density is over $400\ kg/m^3$) and along the channel it is accelerated by hot wall heating, thus creating an asymmetric behaviour of the flow. However, the pressure distribution (see Fig. 7.2) is one-dimension like, regardless of the evident three-dimensional geometry of the channel and of the asymmetric thermal boundary conditions. This behaviour, induced by constant sectional area of the channel, characterizes all the 24 three-dimensional computations performed in this framework.

Fig.7.3 shows temperature stratification at different cross sections: note that the high temperature flow region, induced by the hot wall boundary conditions, grows as the fluid moves from the inlet to the exit section but it remains close to the hot wall along the whole length. For that reason, the fluid far from the bottom wall is nearly at the inlet condition and a pronounced thermal stratification occurs. This effect is due to the high inertia of the flow with respect to the thermal diffusivity of the coolant flow. Since the inertia is high when the density is high, in case of transcritical flow (high-density flow) the thermal diffusivity is less effective than in a low-density flow (such as test case 1).

Fig.7.4 shows density stratification along the channel flow. Note that density varies more than one order of magnitude, from the gas-like density $22\ kg/m^3$ at $T = 600\ K$ to the liquid-like density $405\ kg/m^3$ at $T = 130\ K$. Thus, in a cross section two different thermodynamic behaviours coexist. This phenomenon is clearly visible in Fig. 7.5 where the compressibility factor along the channel is presented: close to the hot-wall, methane behaves like a compressible fluid (i.e., a gas) since $Z \simeq 1$ while close to the cold wall methane behaves almost like an incompressible fluid (i.e., a liquid) since $Z \ll 1$. Between these two regions, fluid is characterized neither like a gas nor like a liquid. The highly different thermodynamic behaviour in a single channel cross section proves that an adequate "non-standard" numerical techniques must be employed to describe the peculiar flow inside cooling channels. For example, in Ref. [37] the strong difference between coolant flow behaviour described by perfect gas law and a proper equation of state is highlighted.

The analysis of Fig. 7.6 clearly shows that the streamwise velocity is asymmetrically distributed; in fact the heating from the hot wall implies a greater acceleration of the flow near the bottom wall than near the top wall.

Note that, since every channel section has a constant pressure while temperature ranges from the minimum value $130\ K$ to the maximum value $600\ K$, thermodynamic parameters variation across a channel section is similar to the isobaric properties variation seen in Sec. 2.5.2. For that reason, speed of sound (Fig. 7.7) and specific heat at constant pressure (Fig. 7.8) show a peak value in a given cross section. The peak value is a minimum in case of speed of sound and it is a maximum in case of specific heat and, for a given pressure (that is, for a given section), the peak value occurs at the pseudo-critic temperature. Since the pseudo-critic temperature is close to the critical temperature ($T_c = 190.53\ K$ in case of methane), a peak value of many thermodynamic parameters in a given cross section is expected for a transcritical flow regime. For that reason, this behaviour is not present in the case of fully supercritical working condition, like in the case of hydrogen in cooling channels. Obviously, the methane peak value of c_p (up to four times the "normal" value) is of great advantage to cooling performances since specific heat is a direct measure of heat absorbing capacity of the fluid. However, methane peak value of specific heat is less than half of that of supercritical hydrogen. This means that methane is a less efficient coolant with respect to the hydrogen and then more coolant mass flow rate is needed (for a comparison between methane and hydrogen cooling performances see also Sec. 4.5).

Finally, Fig. 7.9 shows Mach number field along the channel flow. Comparing streamwise velocity field (Fig. 7.6) and Mach number distribution in the last channel section, it is clear that high Mach number region is wider than high streamwise velocity region. It is a direct consequence of the wide low speed of sound region that is present in the channel cross section (see Sec. 7.7).

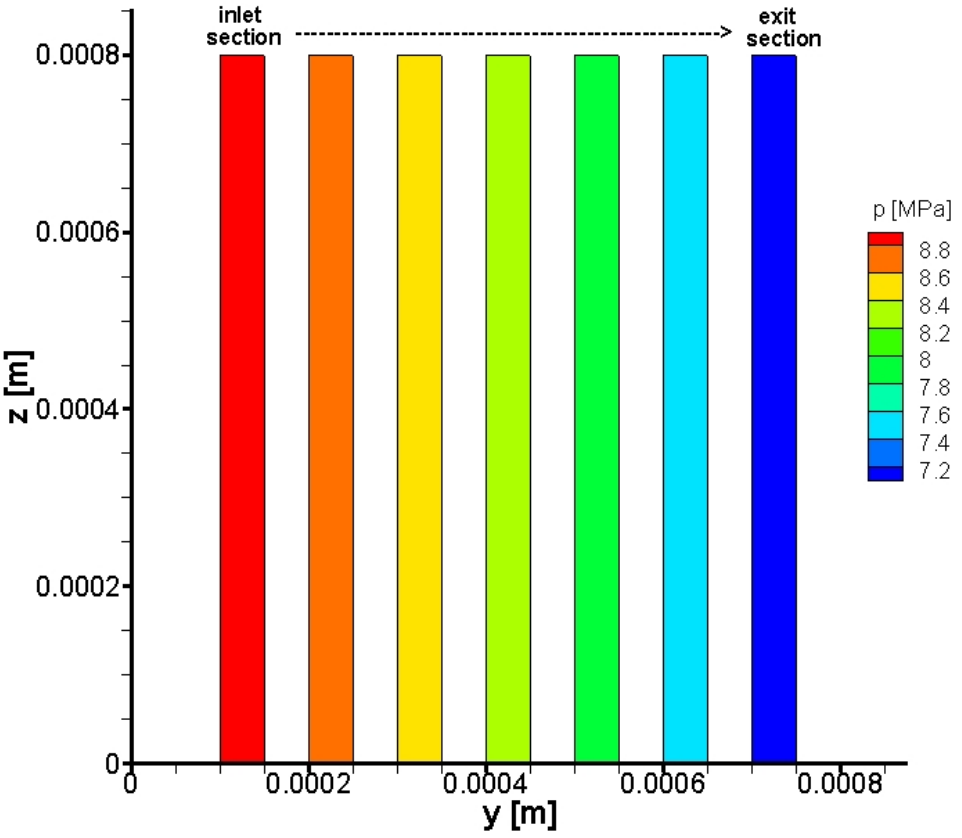

Figure 7.2: Pressure contour plots of various cross section of the channel, for test case 3 and AR$=8$.

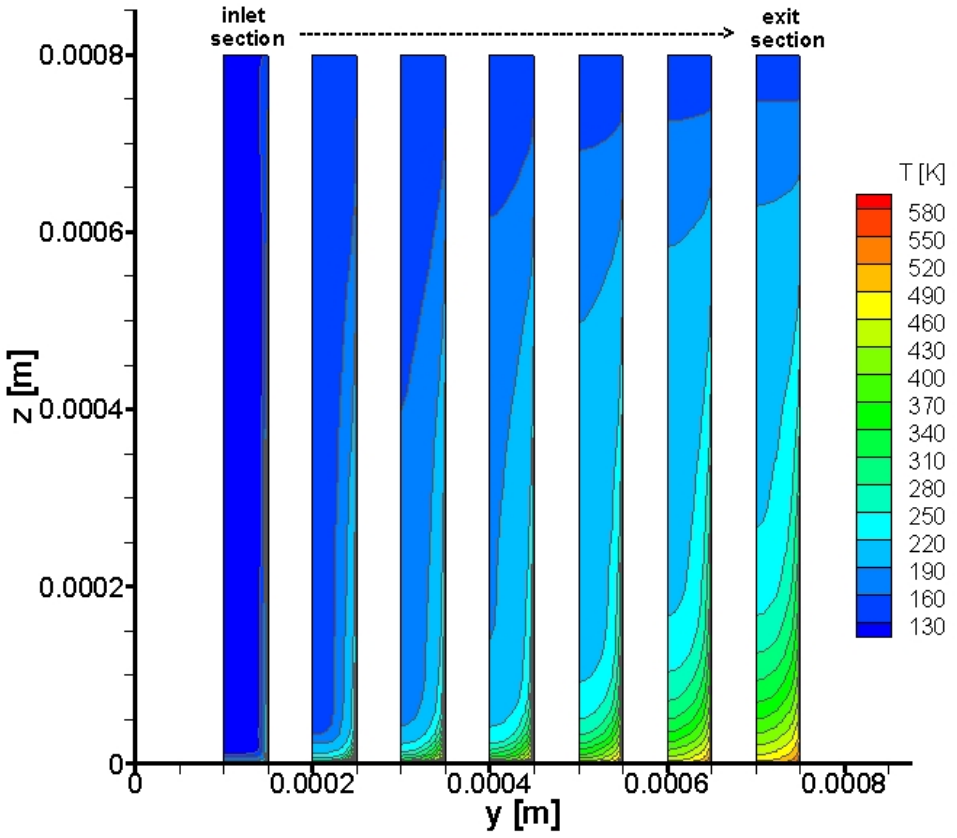

Figure 7.3: Temperature contour plots of various cross section of the channel, for test case 3 and AR$=8$.

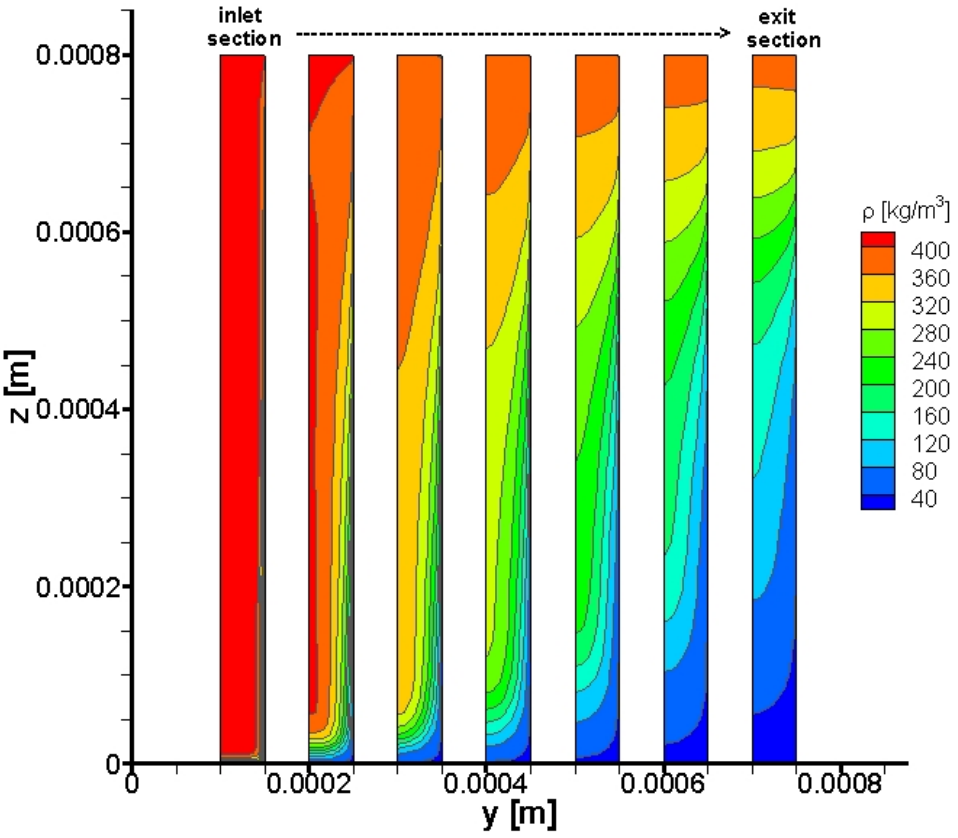

Figure 7.4: Density contour plots of various cross section of the channel, for test case 3 and AR$=8$.

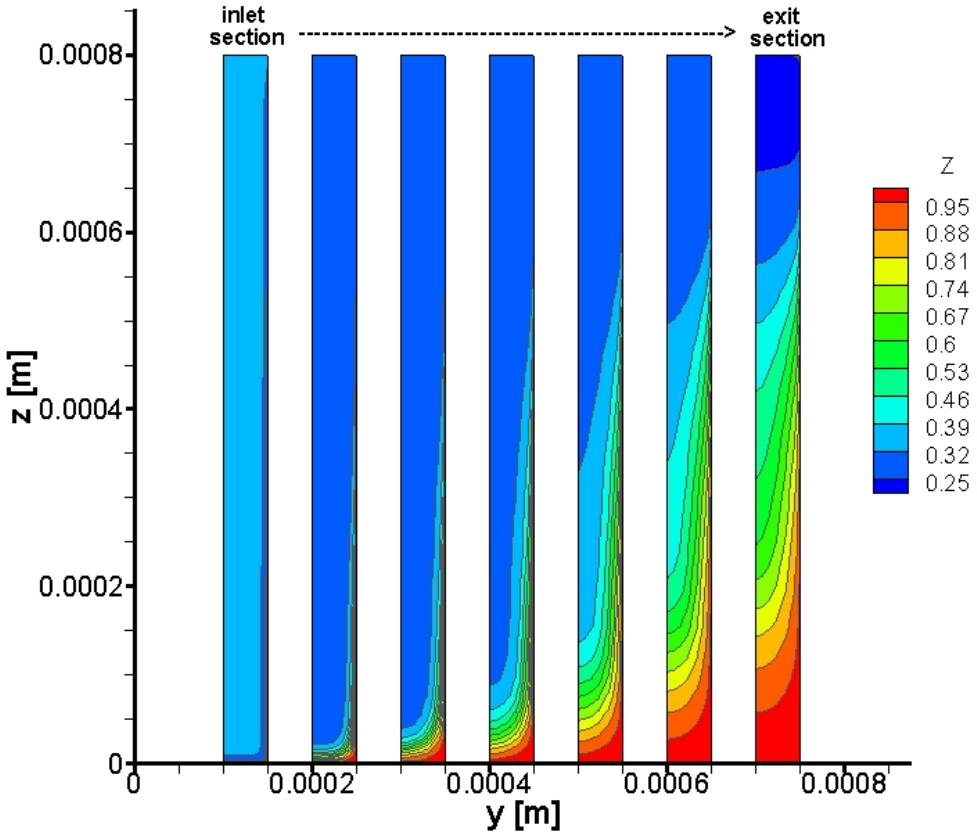

Figure 7.5: Compressibility factor contour plots of various cross section of the channel, for test case 3 and AR$=8$.

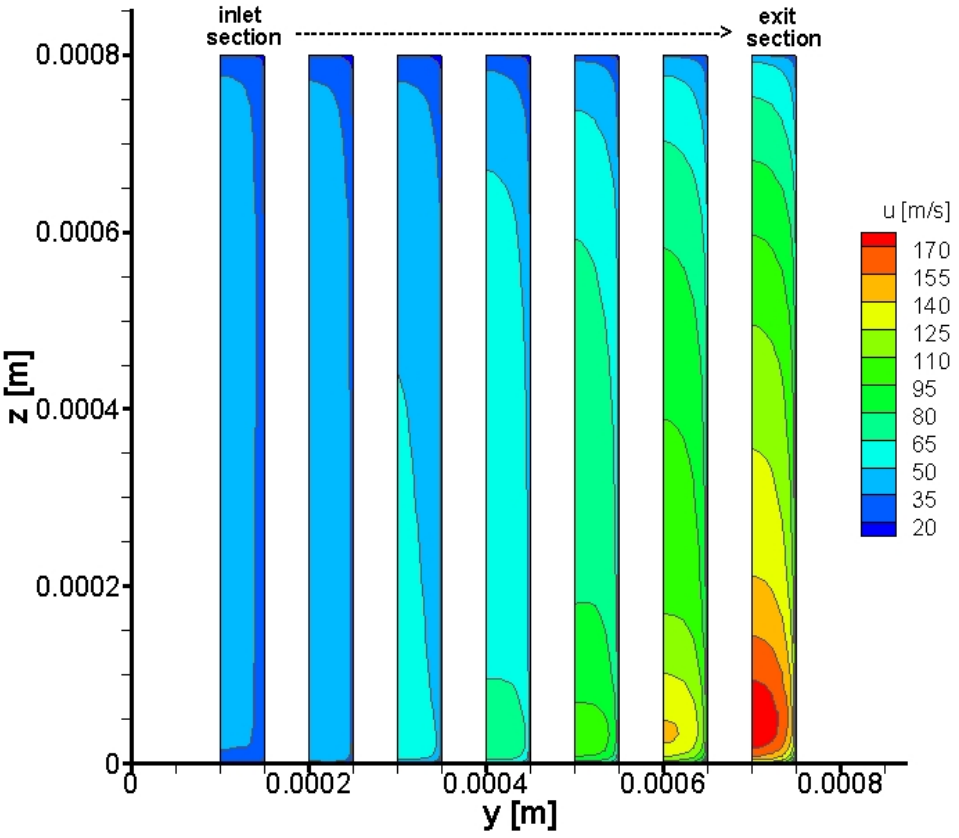

Figure 7.6: Streamwise velocity contour plots of various cross section of the channel, for test case 3 and AR$=8$.

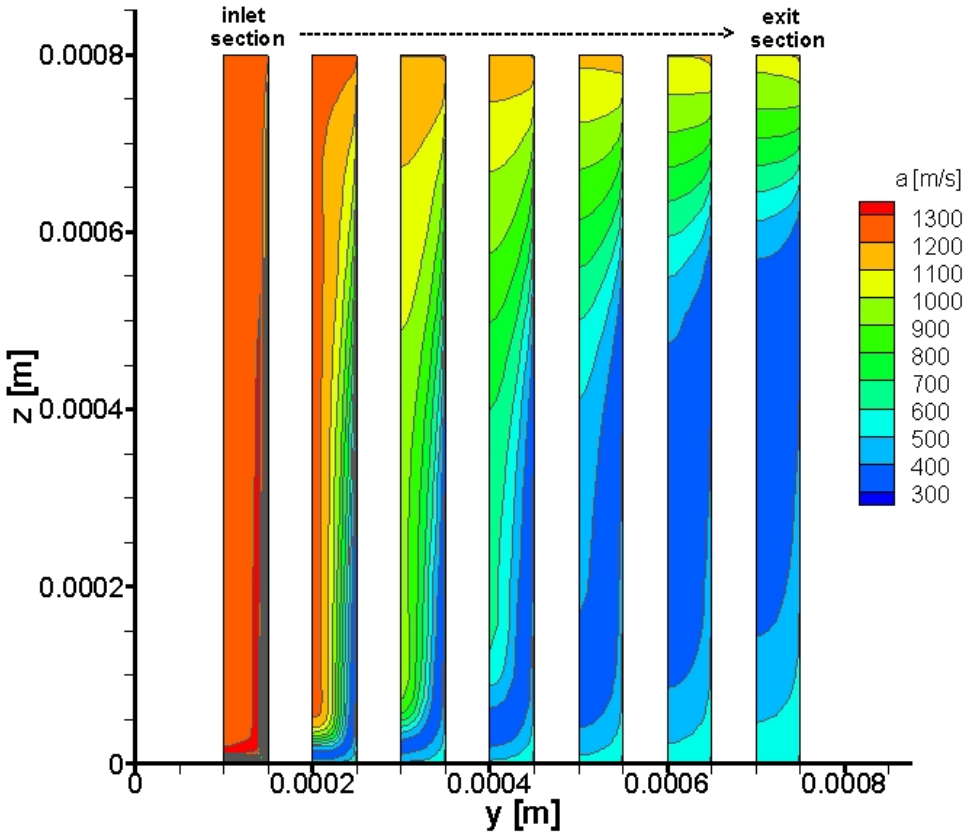

Figure 7.7: Speed of sound contour plots of various cross section of the channel, for test case 3 and AR$=8$.

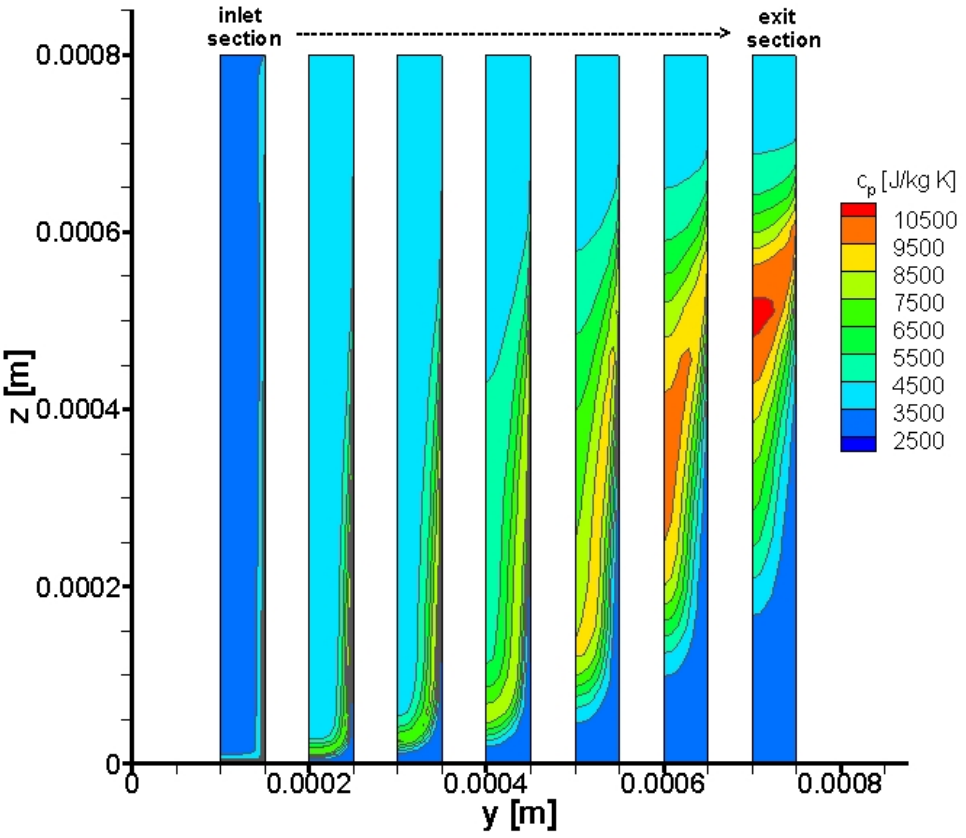

Figure 7.8: Specific heat at constant pressure contour plots of various cross section of the channel, for test case 3 and AR$=8$.

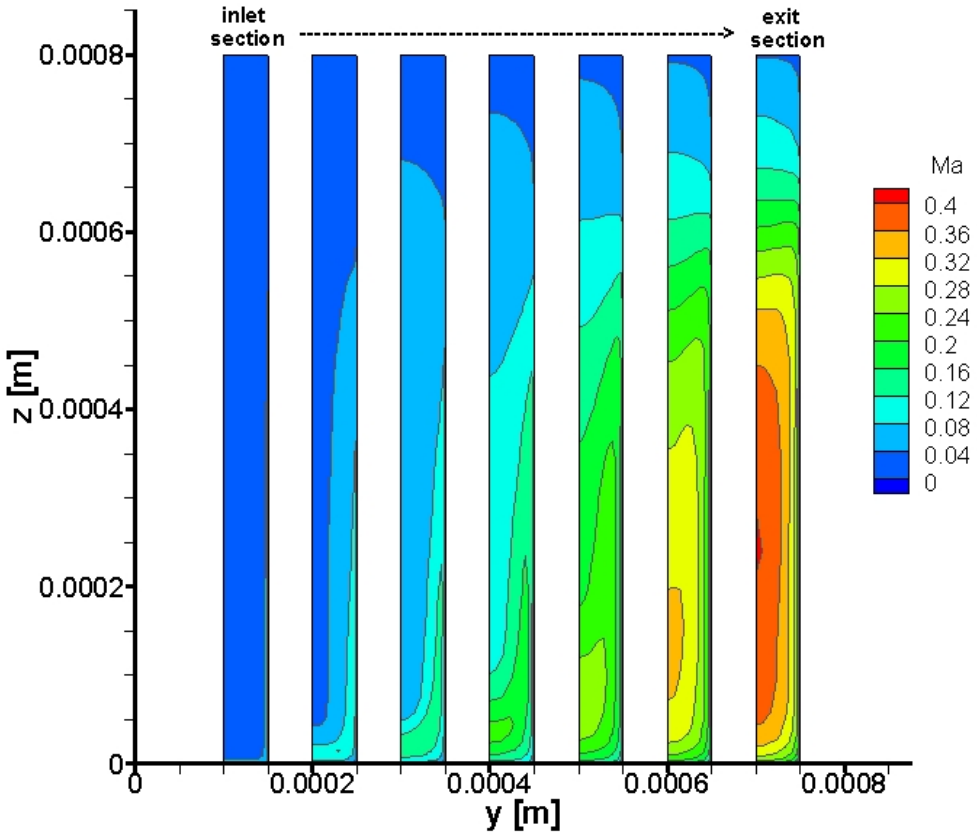

Figure 7.9: Mach number contour plots of various cross section of the channel, for test case 3 and AR$=8$.

7.3 Parametric analysis: aspect ratio effect

In this section, we want to describe how wall heat transfer and skin friction vary with different geometric configurations (that is, AR$=1$, 2, 4, and 8). In particular, the attention is focused on test case 3. In Fig. 7.10 wall heat flux on the side and bottom wall are respectively presented.

At first glance, it is evident that wall heat flux (such as skin friction) is negligible in the proximity to the channel corners. This three-dimensional effect is due to the enlargement of the boundary layers in this zone. In fact, the side-wall boundary layer and the bottom-wall boundary layer interact in the corner zone thus reducing velocity and temperature gradients at wall. Wall heat flux at the side wall presents a maximum value close to the bottom wall which significantly reduces when aspect ratio increases. Moreover, the heat flux distribution along the side wall tends to become flat at high aspect ratio. This means that high aspect ratio geometric configuration distributes wall heat transfer in a better way and thus coolant is heated more efficiently (i.e., coolant absorbs more heat from hot-gas). Note that, since a temperature distribution is imposed on the wall, a small amount of heat entering from the wall is present in the proximity of the top wall. Obviously, in the real applications, this minor effect does not occur since the top wall is adiabatic. Concerning wall heat flux distribution on the bottom wall, as the aspect ratio increases the heat flux reduces. Thus, it is possible to say that high aspect ratio cooling channel absorbs heat flux mostly from the side wall then from the bottom wall.

Skin friction distribution on the side wall and on the bottom wall is presented in Fig. 7.11. Skin friction clearly increases whith aspect ratio, thus confirming that high aspect ratio configuration optimizes cooling performances in spite of larger pressure loss (that is, larger skin friction). Note that on the side wall skin friction has a maximum value is the cold wall region. This is due to the smaller boundary layer displacement in the cold zone than in the hot zone. To better comprehend the aspect ratio effect on heat transfer and friction loss, on Fig. 7.12 the average heat transfer rate and friction force per unit length are presented. Heat transfer rate and friction force per unit length of channel are defined by:

$$\frac{dQ}{dx} = \int_{P_w} q_w dP_w \quad \text{and} \quad \frac{dT}{dx} = \int_{P_w} \tau_w dP_w$$

where P_w is the perimeter of a given cross section at the abscissa x. In Fig. 7.12 the area below the curve dQ/dx represents the heat transfer rate absorbed by the coolant along the entire length of the channel, while the area below the curve dT/dx represents the friction force acting on the coolant along the entire length of the channel. As already noticed in this section, Fig. 7.12 clearly confirms that both friction force and coolant-flow heat-absorbing capacity increase with as-

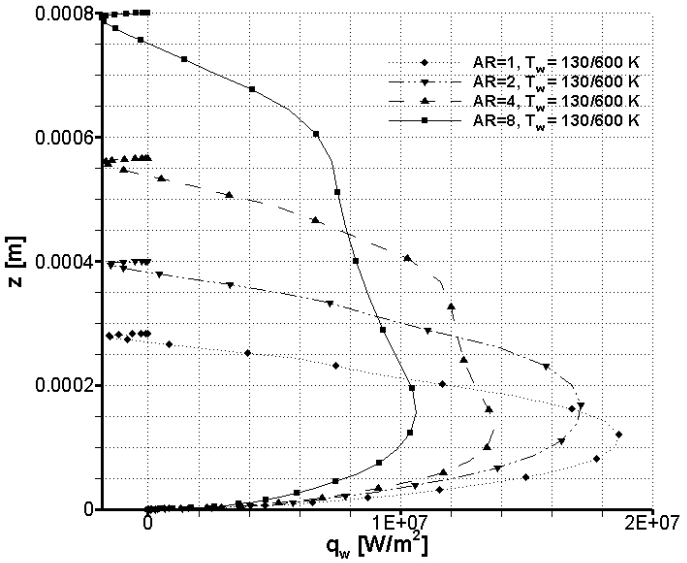

(a) Wall heat flux distribution on the side wall, for test case 3.

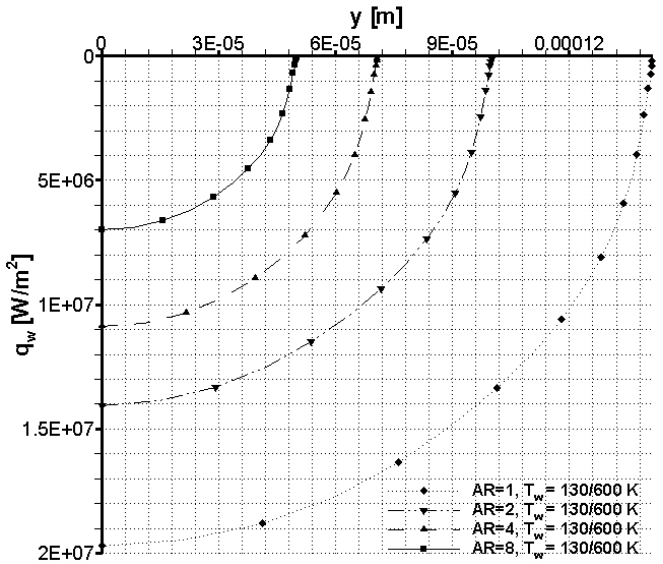

(b) Wall heat flux distribution on the bottom wall, for test case 3.

Figure 7.10: Wall heat flux distribution along the periphery of the channel.

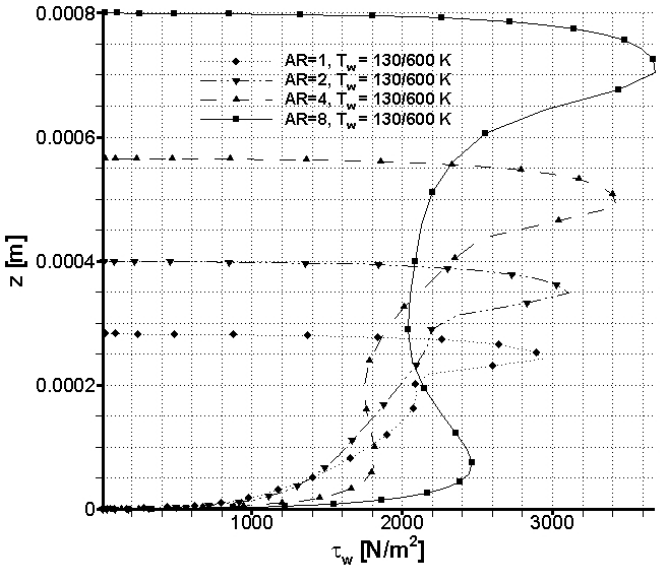

(a) Skin friction distribution on the side wall, for test case 3.

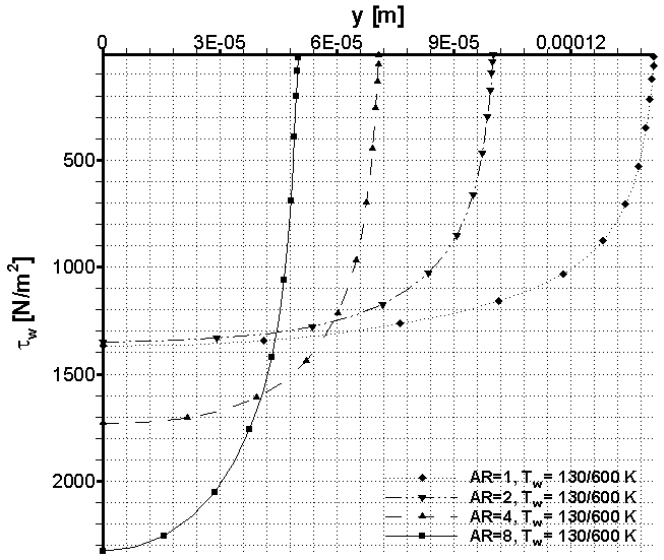

(b) Skin friction distribution on the bottom wall, for test case 3.

Figure 7.11: Skin friction distribution along the periphery of the channel.

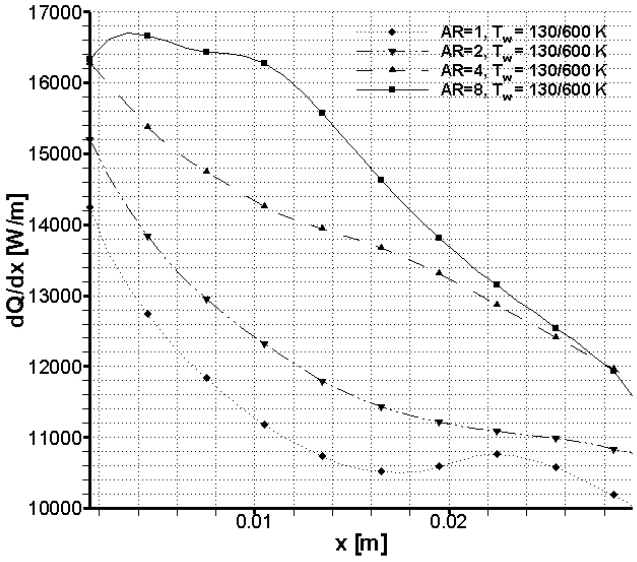

(a) Heat transfer rate per unit length of channel, for test case 3.

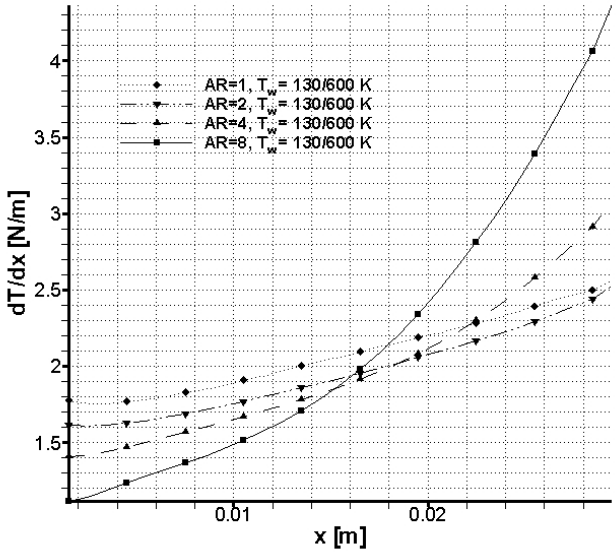

(b) Friction force per unit length of channel, for test case 3.

Figure 7.12: Heat transfer and friction force along the channel streamwise direction.

pect ratio. The latter effect is the fin enhancement effect (see also Sec. 3.6) which is due to the perimeter increase with aspect ratio; in fact, having a constant cross sectional area, from AR$=1$ to AR$=8$, the perimeter increases by 60%. However, in Fig. 7.12 the fin enhancement effect is dimmed by the fact that, due to the chosen inflow conditions (see Sec. 7.1), mass flow rate decreases when aspect ratio increases. To better value the fin enhancement effect, in Fig. 7.13 the heat transfer rate per unit length and unit mass flow rate is presented. Its definition is:

$$\frac{1}{\dot{m}}\frac{dQ}{dx} = \frac{1}{\dot{m}}\int_{P_w} q_w dP_w = \frac{1}{m}\frac{dE}{dx}$$

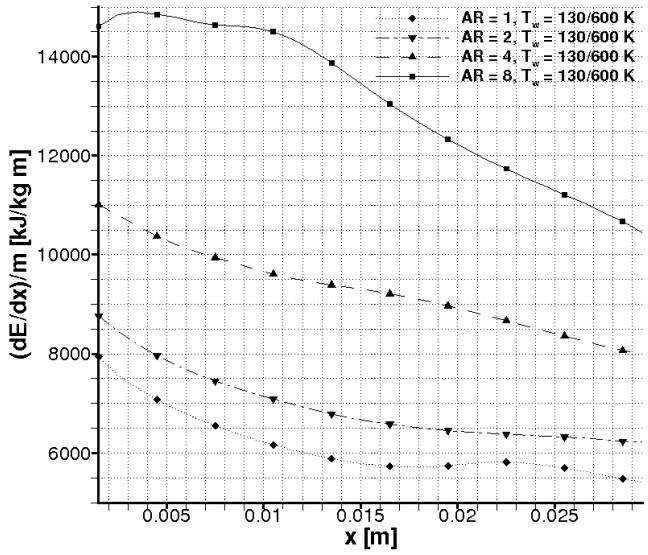

Figure 7.13: Heat transfer rate per unit length of channel and per unit coolant mass flow rate, for test case 3.

This parameter is of great importance since it represents the thermal energy E absorbed by the unit mass of coolant m in the unit length of channel and it can be considered as a concrete estimation of coolant efficiency. Looking Fig. 7.13, it is easy to say that coolant efficiency is more than doubled when aspect ratio is increased from 1 to 8. Thus, it is confirmed that high aspect ratio configurations have a positive influence on cooling performances. This influence is due to both the perimeter increase of the channel section and the uniform distribution of the heat flux around the channel periphery. In fact, in the case of AR$=1$ and 8 the former effect can justify an increase of the cooling efficiency by 60% only.

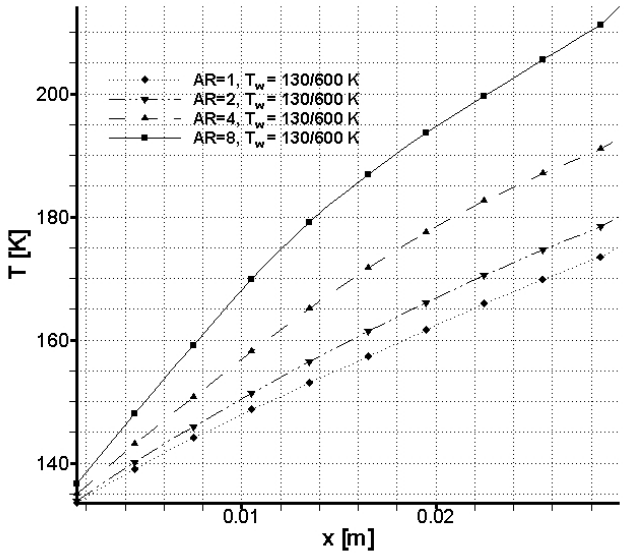

(a) Coolant temperature increase along the channel length, for test case 3.

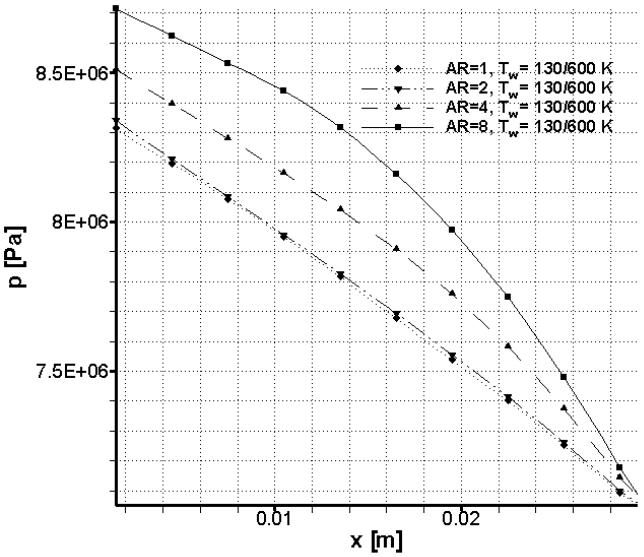

(b) Coolant pressure loss along the channel length, for test case 3.

Figure 7.14: Heat transfer and friction force along the channel streamwise direction.

The channel configuration effect on heat transfer rate and friction force influences the coolant flow also. This influence is clearly visible on coolant temperature increase and pressure loss (see Fig. 7.14). In these figures temperature and pressure at a given section are evaluated using the "bulk" average definition:

$$T_b = \frac{1}{\dot{m}} \int_A T \, \rho u dA \quad \text{and} \quad p_b = \frac{1}{\dot{m}} \int_A p \, \rho u dA$$

As a consequence of what seen in this section, the highest is the aspect ratio the highest is the coolant temperature increase and pressure loss. For example, temperature increase through the exit and inlet section is $83\ K$ for AR$= 8$ case and $44\ K$ for AR$= 1$ case while pressure loss is $18\ bar$ for AR$= 8$ and $15\ bar$ for AR$= 1$.

7.4 Parametric analysis: inlet temperature effect

In this section the methane flow behaviour of test cases 1, 2, and 3 is described to evaluate the inlet temperature effect. In these test cases the inlet stagnation pressure and exit pressure are kept constant ($p_{0,in} = 90\ bar$ and $p_{exit} = 70\ bar$) while inlet stagnation temperature is varied: $T_{0,in} = 220\ K$ for test case 1, $T_{0,in} = 183\ K$ for test case 2, and $T_{0,in} = 130\ K$ for test case 3. In Tab. 7.4 the mass flow rate per unit area, heat absorbed per unit mass, and pressure loss for test cases 1, 2, and 3 are summarized. At first glance, it is evident that, as already noticed in the previous section, for a given test case mass flow rate strongly decreases with aspect ratio. This is due to the higher friction force and heat transfer rate that affect channels with higher aspect ratio. Comparing different test cases with the same channel geometric configuration (i.e., the same aspect ratio) it is also evident that, as the inlet stagnation temperature decreases, the mass flow rate increases due to the higher fluid density. With respect to heat absorbed and pressure loss for a given test case, they increase with aspect ratio (as already seen in the previous section), but for a given channel configuration the inlet temperature effect is not straightforward. This is particularly true for the heat absorbed by coolant since pressure loss is little affected by inlet stagnation temperature. In fact, as a matter of fact, test cases 1, 2, and 3 have the same pressure gradient $p_{0,in} - p_{exit}$ and for a given channel aspect ratio the skin friction acts on the same surface. Heat absorbed has not a monotonic tendency since it is a minimum for test case 2 and it is a maximum for test case 1 (except for AR$= 8$). This anomalous trend is probably due to the different thermal boundary conditions of the considered test cases. In fact, to study the inlet temperature effect, also the temperature distribution along the channel periphery is varied: wall temperature ranges from $220\ K$ to $600\ K$ for test case 1, from $183\ K$ to $600\ K$ for test case 2, and from $130\ K$ to $600\ K$ for test

$T_{0,in}\ [K]$	AR	$\frac{\dot{m}}{A}\ [\frac{kg}{m^2\ s}]$	$\frac{E}{m}\ [\frac{kJ}{kg}]$	$\Delta p\ [bar]$
220	1	9220.	203.4	15.89
220	2	8857.	230.0	16.23
220	4	7892.	352.7	17.04
220	8	6691.	368.9	17.76
183	1	16797.	172.3	15.75
183	2	15746.	201.2	16.23
183	4	13153.	275.5	17.40
183	8	10041.	401.1	18.61
130	1	23184.	188.4	14.87
130	2	21636.	212.2	15.16
130	4	18430.	283.0	16.49
130	8	13844.	397.7	18.15

Table 7.4: Mass flow rate per unit area, heat absorbed per unit mass and pressure loss along the channel, for test cases 1, 2, and 3.

case 3. Thus, these different thermal conditions do not permit to easily quantify the inlet temperature effect on the heat absorbed by the coolant.

In Fig. 7.15, 7.16, and 7.17 the temperature and velocity contour plots, as well as wall heat flux and skin friction distributions in the last cross section, for the test cases 1, 2, and 3 are shown. In particular, every figure is divided into two parts; on the upper part temperature field of the last channel section is shown and wall heat flux distribution is represented as a vector field applied along the periphery of the channel cross section; wall heat flux is positive if the vector is directed outward the channel section; on the lower part, streamwise velocity field of the last channel section is shown and skin friction distribution is represented as a vector field applied along the periphery of the channel cross section. Note that the vector length are based on the same scale and thus vectors of different figures can be directly compared.

Fig. 7.15, 7.16, and 7.17 clearly point out that temperature stratification is more effective if the inlet stagnation temperature is higher. In fact, in test case 1 temperature contour lines are flatter than test case 2 and 3. This temperature behaviour implies that temperature gradients inside the channel cross section, and thus wall heat transfer, are smaller. The condition of flat temperature distribution is a sort of "equilibrium" condition in which coolant is at the same wall temperature condition and thus there is no need to transfer heat flux any more (adiabatic

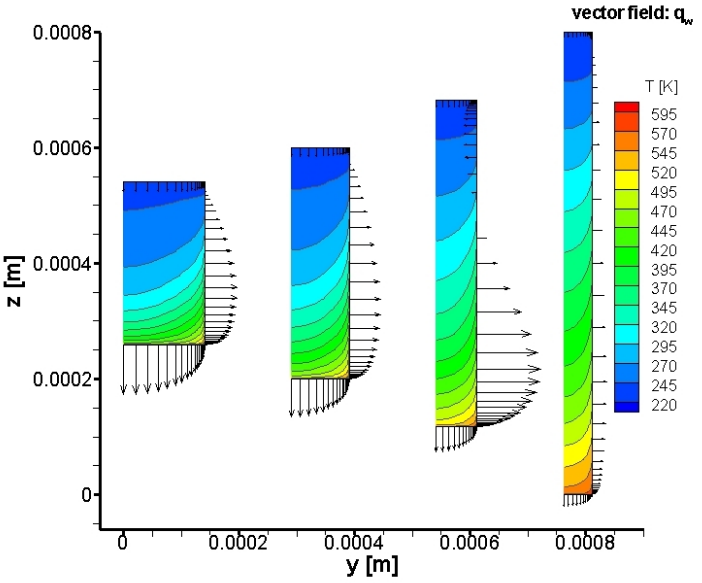

(a) Temperature contour plots of last cross section and wall heat flux distribution of last cross section.

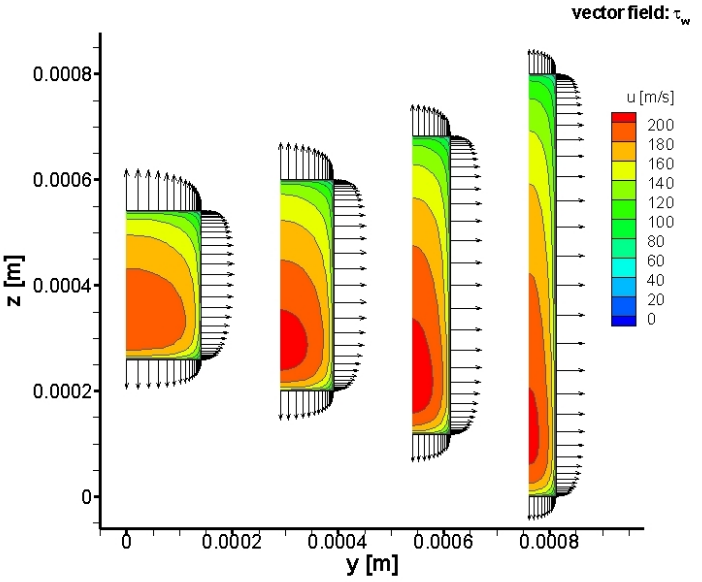

(b) Streamwise velocity contour plots and skin friction distribution of last cross section.

Figure 7.15: Velocity and temperature fields and wall heat flux and skin friction distribution of test case 1.

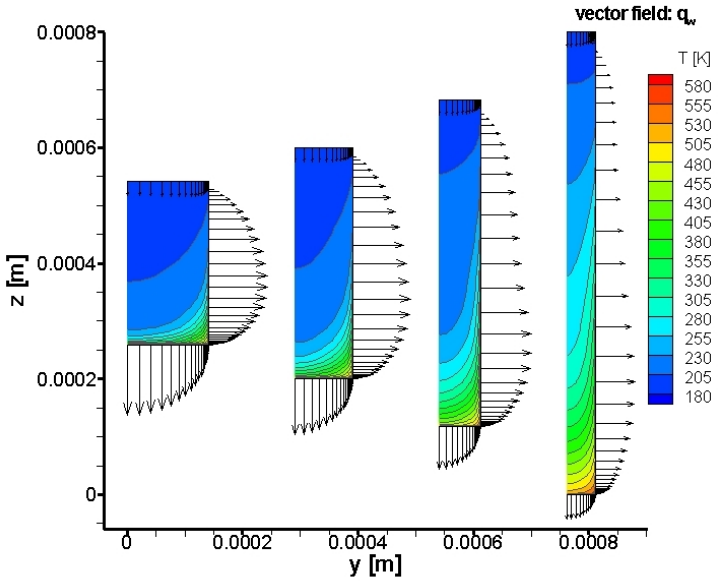

(a) Temperature contour plots of last cross section and wall heat flux distribution of last cross section.

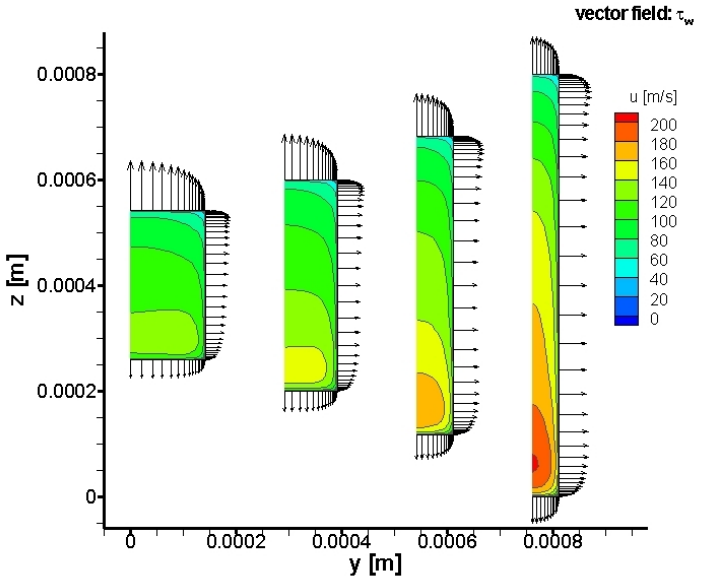

(b) Streamwise velocity contour plots and skin friction distribution of last cross section.

Figure 7.16: Velocity and temperature fields and wall heat flux and skin friction distribution of test case 2.

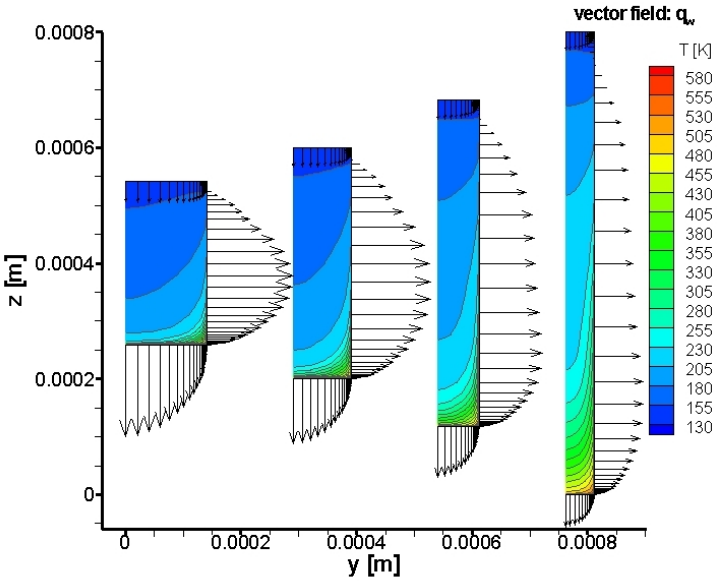

(a) Temperature contour plots of last cross section and wall heat flux distribution of last cross section.

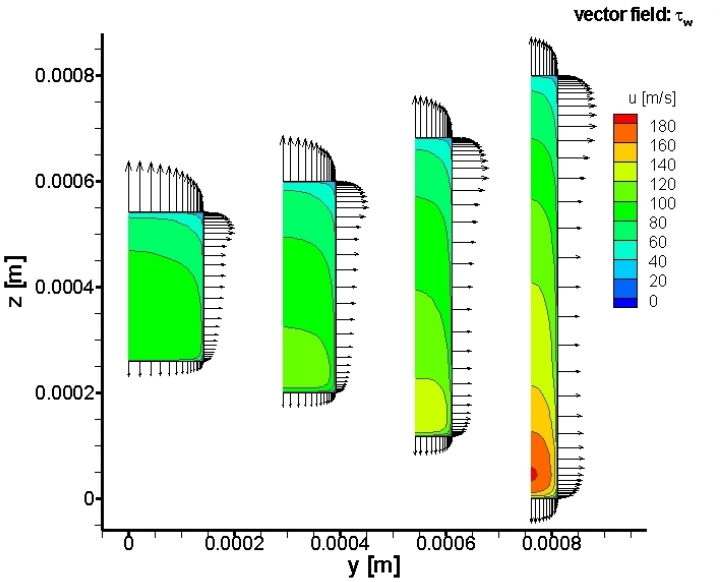

(b) Streamwise velocity contour plots and skin friction distribution of last cross section.

Figure 7.17: Velocity and temperature fields and wall heat flux and skin friction distribution of test case 3.

condition). Test case 1 with aspect ratio 8 is close to this "ideal" condition; in fact, temperature contour lines are almost horizontal and wall heat flux is highly reduced. The equilibrium condition is hardly reached in case of strong wall temperature differences because of the long time required to diffuse heat in case of strong differences between coolant temperature and wall temperature. This can be easily explained by considering the common fact that between two bodies at different temperatures, both the heat transfer rate and the time required to reach thermal equilibrium are higher if theirs temperature difference is higher. As a direct consequence, the lower is the inlet temperature, and thus the higher is the gradient between coolant and wall temperature, the more is the heat transfer rate through the wall. Moreover, it is easy to notice that, for a given test case, high aspect ratio configuration leads to a more pronounced thermal stratification. This implies that wall heat flux distribution along the side wall is more regular and it is not characterized by the peak value that is present in case of low aspect ratio (see also Sec. 7.3). Note that temperature stratifies more effectively in case of high aspect ratio because the channel base dimension becomes negligible with respect to the height dimension and thus the flow variables differences along the base-direction are of secondary effect with respect to that along the height-direction. It can be said that, in case of high aspect ratio, the problem reduces to a two-dimensional flow: streamwise-direction and height-direction flow. Thus, the simplified "quasi 2D" tool presented in Chap. 4 seems to be a promising tool to describe high aspect ratio coolant flow since it is based on realistic assumption (i.e., thermal stratification along the channel height-direction).

As already pointed out, stagnation inlet temperature has a minor effect on skin friction and thus coolant pressure loss. Fig. 7.15, 7.16, and 7.17 confirm this trend even if skin friction distribution along the periphery of the channel is slightly different as inlet temperature varies. Concerning streamwise velocity plots, temperature stratification induces a velocity peak value close to the bottom wall. In fact, close to the bottom wall the low-density, high-temperature flow region is accelerated more than the high-density, low-temperature flow region close to the top wall, due to the induced thermal expansion by the hot wall.

Fig. 7.18 shows the coolant streamwise velocity on the channel centerplane and at last cross section, for AR$=$ 1, and 8. These figures clearly show that velocity peak value is more pronounced in case of higher aspect ratio and lower inlet temperature. Note that streamwise velocity is higher when inlet temperature is higher even if mass flow rate is lower (see Tab. 7.4). This is due to the strong density dependence on temperature, in case of subcritical/supercritical fluid; for example, methane density (for a pressure of 90 bar) varies from 150 kg/m^3 at $T = 220$ K (test case 1) to 400 kg/m^3 at $T = 130$ K (test case 3). Finally we can resume the inlet temperature effect by saying that when it decreases, mass flow rate strongly increases while pressure loss is affected in a minor way.

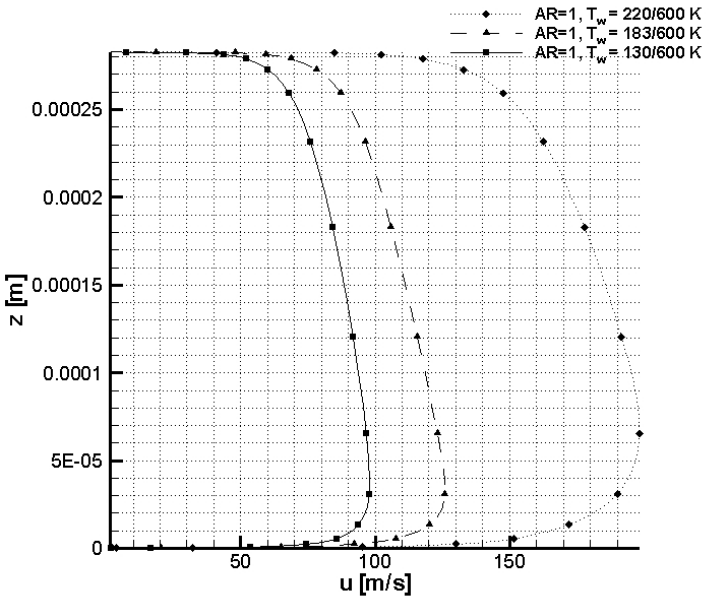

(a) Streamwise velocity on the channel centerplane, for AR$=1$.

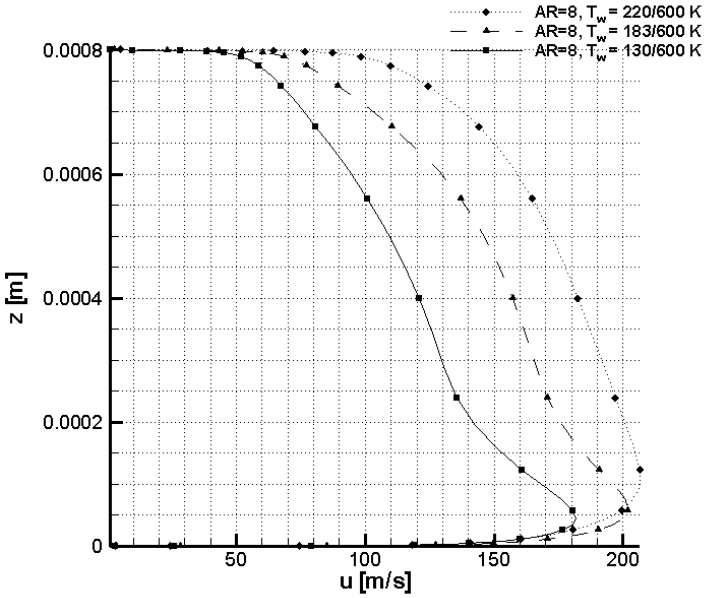

(b) Streamwise velocity on the channel centerplane, for AR$=8$.

Figure 7.18: Streamwise velocity on the channel centerplane and at last cross section.

7.5 Parametric analysis: inlet pressure effect

In this section the methane flow behaviour of test cases 4, 5, and 6 is described to evaluate the inlet pressure effect. In these test cases the inlet stagnation temperature and exit pressure are kept constant ($T_{0,in} = 180\ K$ and $p_{exit} = 70\ bar$) while inlet stagnation pressure is varied: $p_{0,in} = 90\ bar$ for test case 4, $p_{0,in} = 100\ bar$ for test case 5, and $p_{0,in} = 11\ MPa$ for test case 6. In Tab. 7.5 the mass flow rate per unit area, heat absorbed per unit mass, and pressure loss for test cases 4, 5, and 6 are summarized.

$p_{0,in}\ [bar]$	AR	$\frac{\dot{m}}{A}\ [\frac{kg}{m^2\ s}]$	$\frac{E}{m}\ [\frac{kJ}{kg}]$	$\Delta p\ [bar]$
90	1	17534.	172.9	15.56
90	2	16414.	201.6	16.11
90	4	13687.	275.5	17.32
90	8	10378.	401.0	18.58
100	1	21883.	169.8	22.89
100	2	20517.	198.4	23.70
100	4	17131.	271.6	25.56
100	8	13042.	394.9	27.47
110	1	25605.	168.4	30.11
110	2	23985.	196.9	31.22
110	4	20051.	270.0	33.69
110	8	15313.	392.0	36.25

Table 7.5: Mass flow rate per unit area, heat absorbed per unit mass and pressure loss along the channel, for test cases 4, 5, and 6.

At first glance, it is evident that, for a given channel geometry (i.e., the same aspect ratio), mass flow rate increases with the inlet stagnation pressure. This effect is mostly due to the increasing inlet density with the inlet pressure. Moreover, pressure drop is strongly driven by stagnation inlet pressure since the difference $p_{0,in} - p_{exit}$ is a direct measure (for a given aspect ratio) of the pressure gradient imposed along the channel. On the contrary, heat absorbed by coolant is affected by inlet pressure in a minor way; however, it slightly reduces as $p_{0,in}$ increases.

As already shown in the previous section, in Fig. 7.19, 7.20, and 7.21 the temperature and velocity contour plots, as well as wall heat flux and skin friction distributions in the last cross section, for test cases 4, 5, and 6, are shown.

For a given channel aspect ratio, temperature stratification is little affected by inlet pressure variation. However, since heat transfer coefficient (as well as wall

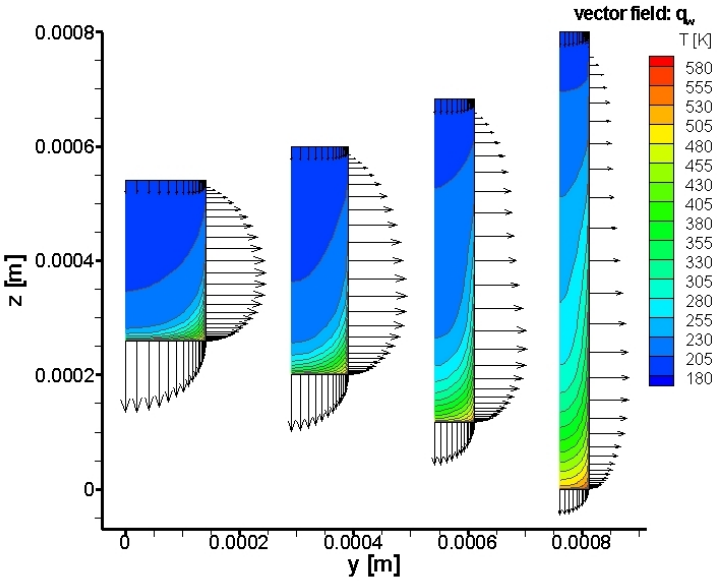

(a) Temperature contour plots of last cross section and wall heat flux distribution of last cross section.

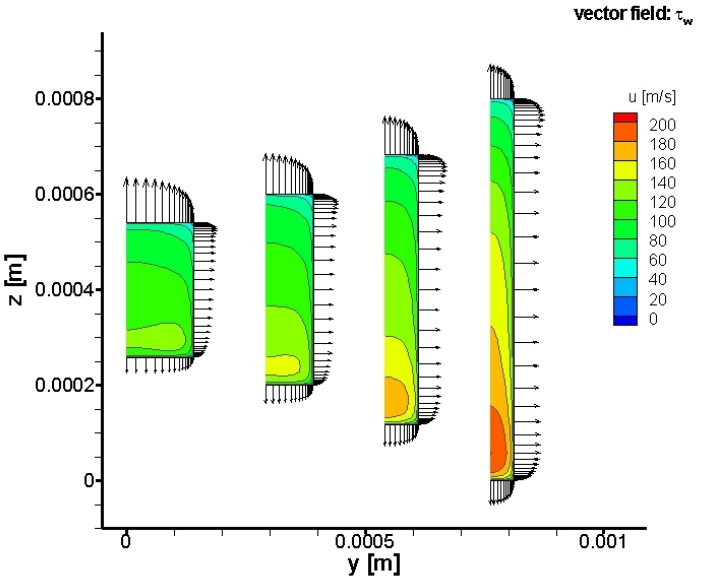

(b) Streamwise velocity contour plots and skin friction distribution of last cross section.

Figure 7.19: Velocity and temperature fields and wall heat flux and skin friction distribution of test case 4.

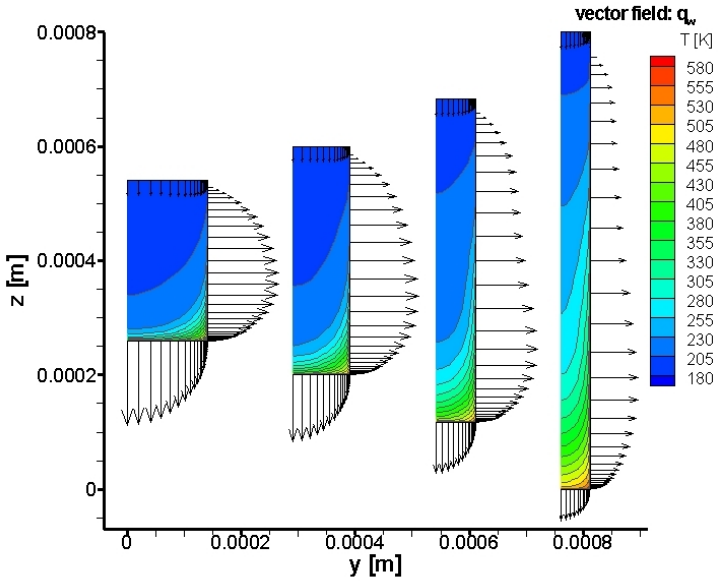

(a) Temperature contour plots of last cross section and wall heat flux distribution of last cross section.

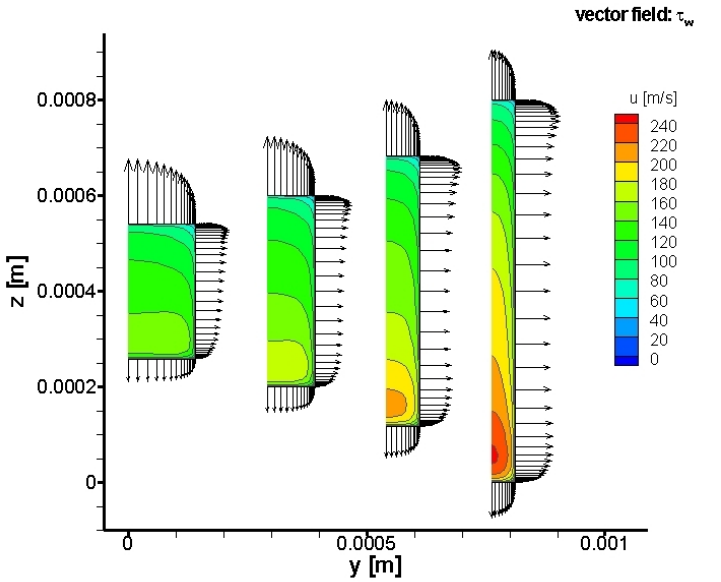

(b) Streamwise velocity contour plots and skin friction distribution of last cross section.

Figure 7.20: Velocity and temperature fields and wall heat flux and skin friction distribution of test case 5.

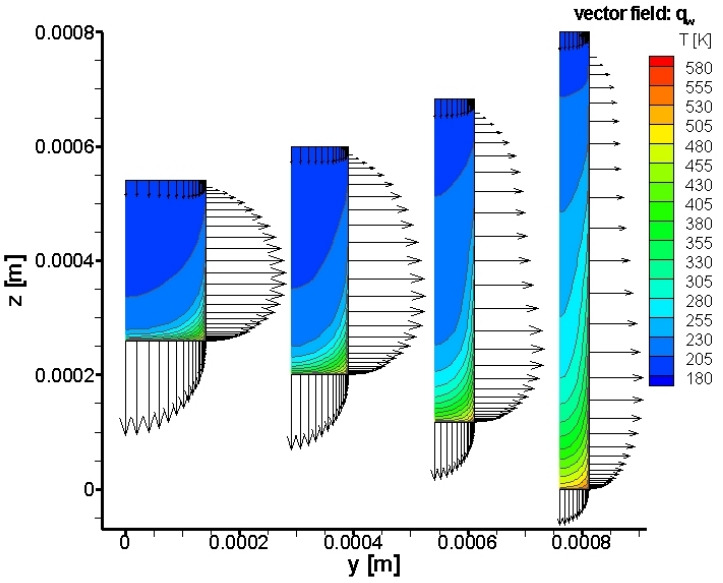

(a) Temperature contour plots of last cross section and wall heat flux distribution of last cross section.

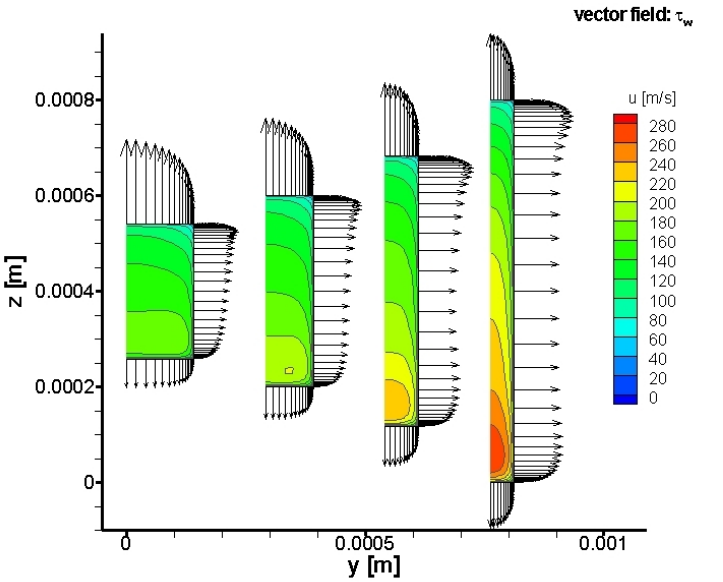

(b) Streamwise velocity contour plots and skin friction distribution of last cross section.

Figure 7.21: Velocity and temperature fields and wall heat flux and skin friction distribution of test case 6.

friction factor) is strongly affected by mass flow rate (as a first approximation, $h \sim (\rho u)^{0.8}$ [12]), wall heat flux increases with inlet pressure. It is confirmed by Fig. 7.22 in which heat transfer rate per unit length along channel streamwise direction and for the given aspect ratio 8 is plotted.

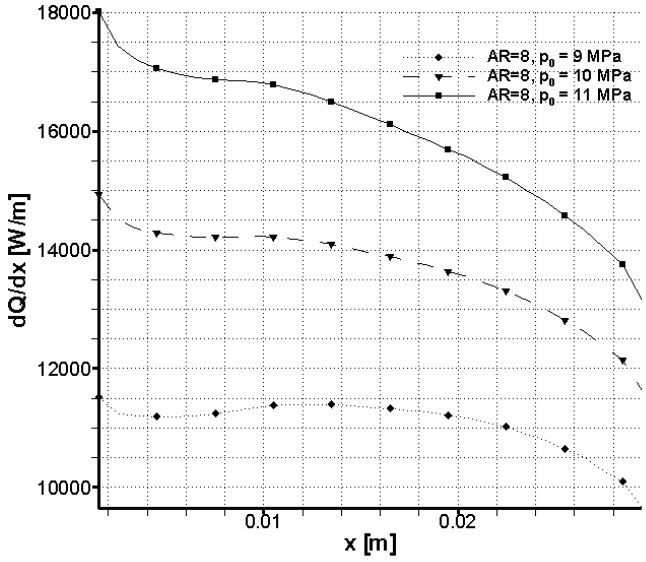

Figure 7.22: Heat transfer rate per unit length of channel, for test cases 4, 5 , and 6, with AR$= 8$.

Fig. 7.19, 7.20, and 7.21 also show that the inlet stagnation pressure effect for a given channel geometric configuration on streamwise velocity distribution and on skin friction is straightforward: due to the increasing mass flow rate the peak value of streamwise velocity and skin friction increases.

Finally, we can resume the inlet pressure effect saying that as it increases, mass flow rate increases as well as coolant pressure drop. Heat absorbed by coolant is affected by inlet pressure in a minor way.

Conclusions

The physical models and the numerical tools carried out in this thesis have permitted to analyze the regenerative cooling, with particular regard to the cooling channel flow. In fact, the capability of predicting wall thermal behaviour, as well as coolant fluid-dynamics is of great interest in order to prevent thermal failure of the engine and to minimize the requested coolant pump power. In particular, in case of cryogenic engines with high aspect ratio cooling channels, the description of coolant flow is a critical issue due to the strong thermal stratification that occurs in this type of channels and the real-fluid behaviour of cryogenic coolants (such as hydrogen and methane). Thus non standard and innovative numerical tools have been studied and developed. The computations obtained with these tools are of great interest since they have pointed out many peculiar phenomena occurring in such technological environment, which are hardly seen in scientific literature. The activity leading to this results can be summarized into three steps described as follows.

As a first step, a proper physical and mathematical model has been selected to describe the thermodynamic behaviour of the coolant. In fact, since in many applications the coolant is one of the cryogenic propellants (such as hydrogen or methane), its behaviour can be described neither by perfect gas law (that is, $p = \rho RT$), nor by perfect liquid law (that is, $\rho = const$). Moreover, even if in actual applications coolant pressure is always supercritical, the wide variation of coolant working conditions (pressure drop of tens of bar along cooling channel and temperature gradient of up to $600\ K$ in a channel cross section) imposes the use of highly accurate polynomial equation of state based on many coefficients (up to 32), which is referred to as "Modified Benedict-Webb-Rubin" equation of state. This equation, as well as proper equations to describe viscosity and thermal conductivity, has been implemented on computer subroutines to represent hydrogen and methane thermodynamic behaviour. The implemented subroutines provide results which are perfectly in line with the data published by N.I.S.T. Moreover, they are able to describe the one-phase hydrogen and methane behaviour of both high-density fluid (that is, subcritical temperature, liquid-phase region), low-density fluid (that is, subcritical temperature, vapour-phase region), and the supercritical

fluid (that is, supercritical temperature region).

As a second step, the coupled hot-gas/wall/coolant behaviour that occurs in regenerative cooling system has been described by a simple and fast "quasi 2D" tool. This tool is an extension of one-dimensional physical model based on semi-empirical relations. In fact, while hot-gas expansion and coolant dynamic behaviour is considered one-dimension like (along the streamwise direction), wall and coolant temperature behaviour is also analyzed in the radial direction. It permits to take into account the strong wall and coolant thermal stratification that occurs in high aspect ratio cooling channels. In particular, wall thermal stratification has been described by means of a simple one-dimensional model in the radial direction and the coolant thermal stratification has been modeled by means of the Kacynski turbulent thermal conductivity. The name "quasi 2D" model has been chosen since it highlights that, even if the model is one-dimensional, it considers temperature as a two-dimensional variable. The capability of predicting coolant and wall thermal behaviour with a single, although simplified, tool is the most interesting and original property of the "quasi 2D" model. This promising model has been validated with respect to the regenerative cooling system data of the European rocket engine, Vulcain, which operates with hydrogen as coolant. A fictitious methane-based cooling system has been considered for the same engine for the sake of a qualitative comparison between hydrogen and methane as coolants. This comparison has shown that both coolants exhibit a strong temperature stratification in the channel cross section and that methane is a less effective coolant with respect to the hydrogen thus indicating that methane-based cooling-system design for future engines is a critical issue.

As a third step, a proper finite volume numerical tool in order to describe the turbulent three-dimensional flow inside cooling channels has been build up. The flow model is based on Navier Stokes governing equations written in a conservative form and without any thermodynamic characterization of the working fluid (i.e., equations of state). This general treatment of the governing equations allows to describe the flow of a generic fluid by means of a proper thermodynamic database. The database can be easily built using the above mentioned subroutines for hydrogen and methane thermodynamic description. Particular efforts have been focused on the Riemann problem solver and on boundary condition for a generic fluid. The most interesting and original property of this numerical tool is that it can describe the flow of a generic one-phase compressible fluid since any type of equation of state can be implemented. The CFD numerical tool has been validated with respect to exact solutions and numerical solutions published in literature, for both perfect gas and supercritical fluid. The validation proved that the considered CFD tool is well modeled and implemented and that it is adequate to describe coolant flow inside cooling passages (that is, three-dimensional, high-Reynolds turbulent flow of a non perfect fluid with strong temperature gradients).

Three-dimensional computations have been performed on straight channels having methane as working fluid. The channel is long enough to ensure that the flow far from the inlet section is fully developed. Many computations have been performed in order to analyze the effect of the main parameters: channel cross section aspect ratio, and the inlet stagnation temperature and pressure. Methane working conditions are the same than in "real" applications since pressure is supercritical (pressure ranges from $110\ bar$ to $70\ bar$) while temperature is transcritical (temperature ranges from $130\ K$ to $600\ K$). Channel cross section aspect ratio has been varied from 1 to 8. Moreover, to avoid long computational time, coolant flow Reynolds number has been reduced by one order of magnitude than in actual applications. This implies that cooling channel dimensions are much smaller than the real ones. However, the main phenomena that characterize methane as coolant have been pointed out:

- A strong methane thermal stratification has been noticed, particularly in the high aspect ratio cases (that is, AR$= 4$, and 8)
- The streamwise velocity exhibits an asymmetric peak value due to the asymmetric wall temperature distribution. This peak value is more pronounced as temperature gradients in a channel cross section are stronger.
- Due to the transcritical working condition of methane, specific heats presents a peak value inside the channel cross section thus influencing the heat absorbing capacity of the coolant flow.
- Increasing channel aspect ratio, coolant efficiency increases (that is, coolant heat absorption increases). As a drawback, coolant pressure drop increases.
- High aspect ratio cooling channel exhibits a more regular distribution of wall heat flux distribution along the channel periphery than low aspect ratio cooling channel.
- Due to the boundary layer enlargement, wall heat transfer is inefficient at the channel corner.
- Inlet temperature mostly affects mass flow rate and wall heat transfer rate absorbed by coolant.
- Inlet pressure mostly affects mass flow rate and coolant pressure drop.

The computations performed are of great interest since the peculiar behaviour of transcritical methane inside cooling channels is not yet presented in scientific literature. In fact, up to now, only hydrogen and nitrogen have been considered as

working fluids in cooling channel CFD computations; those fluids do not possess the methane peculiar behaviour since their working condition is “fully” supercritical (i.e., both temperature and pressure over the critical value).

In conclusion, even if this work can be considered as a first effort in describing the regenerative cooling environment, the presented models have shown a great potential and thus they are promising tools for the design of regenerative cooling system: the “quasi 2D” tool permits to describe in a simple and fast way the main parameters that affect the coupled hot-gas/wall/coolant environment and thus it can be used in an optimization process while the CFD three-dimensional tool can be used to better characterize the three-dimensional behaviour of the coolant flow only. In particular, the semi-empirical relations that affect the “quasi 2D” tool can be tuned by means of the more accurate three-dimensional CFD tool.

Appendix A

Thermodynamic relations

In the following sections, the thermodynamic relations presented in Sec. 2.4 are derived. The subject of this appendix can be found in [42].

A.1 Constant volume specific heat

The specific heat capacity at constant volume c_v is defined as:

$$c_v = \left(\frac{\partial e}{\partial T}\right)_v$$

where e is the specific internal energy, T is the temperature and v is the specific volume ($v = 1/\rho$, where ρ is the density).

Considering the specific internal energy and entropy as functions of specific volume and temperature and differentiating these relations:

$$\begin{cases} e &= e\left(T, v\right) \\ de &= \left(\frac{\partial e}{\partial T}\right)_v dT + \left(\frac{\partial e}{\partial v}\right)_T dv = c_v dT + \left(\frac{\partial e}{\partial v}\right)_T dv \end{cases} \tag{A.1}$$

$$\begin{cases} s &= s\left(T, v\right) \\ ds &= \left(\frac{\partial s}{\partial T}\right)_v dT + \left(\frac{\partial s}{\partial v}\right)_T dv \end{cases}$$

From the first principle of thermodynamics, $de = Tds - pdv$, the entropy and internal energy derivatives can be related:

$$\begin{cases} \left(\dfrac{\partial s}{\partial T}\right)_v = \dfrac{c_v}{T} \\ \\ \left(\dfrac{\partial s}{\partial v}\right)_T = \dfrac{p}{T} + \dfrac{1}{T}\left(\dfrac{\partial e}{\partial v}\right)_T \end{cases} \tag{A.2}$$

A second differentiation of the entropy, considering that the mixed second derivatives are equal, gives:

$$\frac{1}{T}\left(\frac{\partial e}{\partial v}\right)_T = \left(\frac{\partial p}{\partial T}\right)_v - \frac{p}{T}$$

and thus Eq. (A.1) becomes:

$$\begin{cases} ds &= \dfrac{c_v}{T} + \left(\dfrac{\partial p}{\partial T}\right)_v dv \\ \\ de &= c_v dT + \left[T\left(\dfrac{\partial p}{\partial T}\right)_v - p\right] dv \end{cases} \tag{A.3}$$

A second differentiation of the internal energy, considering that the mixed second derivatives are equal, gives:

$$\left(\frac{\partial c_v}{\partial v}\right)_T = T\left(\frac{\partial^2 p}{\partial T^2}\right)_v$$

Using density instead of specific volume:

$$\left(\frac{\partial c_v}{\partial \rho}\right)_T = -\frac{T}{\rho^2}\left(\frac{\partial^2 p}{\partial T^2}\right)_\rho$$

Integrating this relation along a generic isotherm T, from the rarefied-gas state ($\rho \to 0$) to the actual state, we obtain:

$$c_v(\rho, T) = c_{v0} - \int_0^\rho \left[\frac{T}{\rho^2}\left(\frac{\partial^2 p}{\partial T^2}\right)_\rho\right]_T d\rho$$

where the subscript T in the integral indicates that it must be computed having constant temperature, while density ranges from zero to the actual value ρ.

The term c_{v0} is the specific heat at constant volume for a rarefied gas ($\rho \to 0$) and thus it is a function of the temperature only: $c_{v0} = c_{v0}(T)$.

Considering the thermodynamic theory of perfect gas, c_{v0} can be linked to the specific heat at constant pressure via the gas constant R ($R = \Re/W$, where $\Re$ is the universal gas constant and W is the molecular weight of the fluid):

$$c_{v0} = c_{p0} - R$$

where c_{p0} is the rarefied-gas specific heat. Finally, the specific heat at constant volume

$$c_v(\rho, T) = c_{p0} - R - \int_0^\rho \left[\frac{T}{\rho^2} \left(\frac{\partial^2 p}{\partial T^2} \right)_\rho \right]_T d\rho$$

can be computed from the generic equation of state in the form $p = p(\rho, T)$, its derivatives and a function that describes the specific heat for the rarefied gas $c_{p0} = c_{p0}(T)$.

A.2 Constant pressure specific heat

The specific heat capacity at constant pressure is defined by:

$$c_p = \left(\frac{\partial h}{\partial T} \right)_p$$

where h is the specific enthalpy: $h = e + pv$.

Considering the specific enthalpy as a function of pressure and temperature and differentiating this relation:

$$\begin{cases} h &= h\,(p, T) \\ dh &= \left(\dfrac{\partial h}{\partial p} \right)_T dp + \left(\dfrac{\partial h}{\partial T} \right)_p dT = \left(\dfrac{\partial h}{\partial p} \right)_T dp + c_p dT \end{cases}$$

Moreover, considering Eq. (A.3), the differential of the equation of state written in the form $v = v(p, T)$ and that $dh = de + pdv + vdp$, gives:

$$dh = \underbrace{\left[c_v + T \left(\frac{\partial p}{\partial T} \right)_v \left(\frac{\partial v}{\partial T} \right)_p \right]}_{c_p} dT + \underbrace{\left[v + T \left(\frac{\partial p}{\partial T} \right)_v \left(\frac{\partial v}{\partial p} \right)_T \right]}_{\left(\frac{\partial h}{\partial p} \right)_T} dp$$

Using the triple-product rule for the equation of state in the general form $f(p, v, T) = 0$

$$\left(\frac{\partial v}{\partial T} \right)_p \left(\frac{\partial T}{\partial p} \right)_v \left(\frac{\partial p}{\partial v} \right)_T = -1 \tag{A.4}$$

the specific heat at constant pressure finally becomes:

$$c_p = c_v - T\frac{\left(\dfrac{\partial p}{\partial T}\right)_v^2}{\left(\dfrac{\partial p}{\partial v}\right)_T}$$

Using density instead of specific volume gives:

$$c_p = c_v + \frac{T}{\rho^2}\frac{\left(\dfrac{\partial p}{\partial T}\right)_\rho^2}{\left(\dfrac{\partial p}{\partial \rho}\right)_T}$$

The specific heat at constant pressure can be computed from the derivatives of the generic equation of state in the form $p = p(\rho, T)$ and from the specific heat at constant volume.

In the case of perfect gas (i.e., rarefied gas, $\rho \to 0$), the equation of state is $p = \rho RT$ and the relationship between c_p and c_v becomes:

$$c_p = c_v + R \tag{A.5}$$

as already stated in the previous section.

A.3 Entropy

We intend to compute entropy changes from a reference state $s_0(\rho_0, T_0)$. Therefore, the integral:

$$s(\rho, T) = s_0(\rho_0, T_0) + \int_{\rho_0, T_0}^{\rho, T} ds \tag{A.6}$$

must be considered. Room conditions are often chosen as reference state: $p_0 = 1.01325\ bar$ and $T_0 = 298.15\ K$.

The entropy is a state functions, and this allows us to choose any integration path. The path described in Fig. A.1 is considered here: an isothermal expansion to zero density, followed by an isochoric heating, and by an isothermal compression. In this situation, heating takes place in a region where the fluid can be considered as a perfect gas, since the density approaches zero.

Eq. (A.6) is then written:

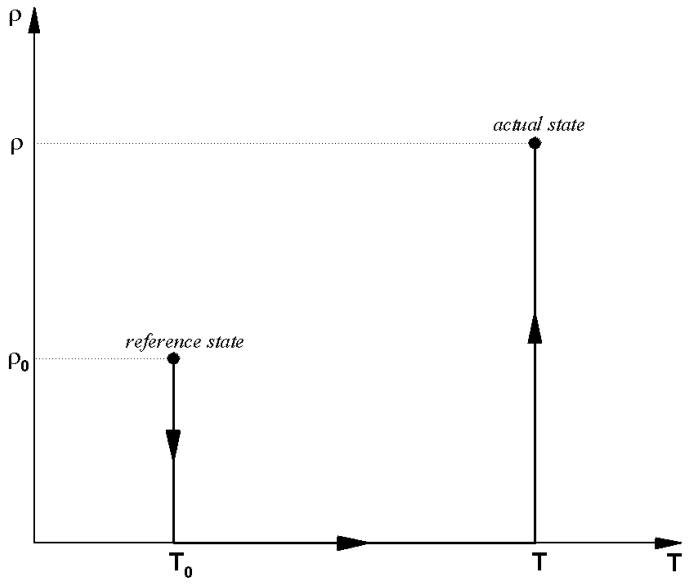

Figure A.1: Integration path for the calculation of a state function from the reference state to the actual state.

$$s(\rho,T) = s_0(\rho_0,T_0) + \underbrace{\int_{\rho_0,T_0}^{0,T_0} ds}_{\textit{isotherm}} + \underbrace{\int_{0,T_0}^{0,T} ds}_{\textit{isochoric (perfect gas)}} + \underbrace{\int_{0,T}^{\rho,T} ds}_{\textit{isotherm}} \tag{A.7}$$

Considering Eq. (A.3) in terms of density instead of specific volume, gives:

$$ds = \frac{c_v}{T}dT - \frac{1}{\rho^2}\left(\frac{\partial p}{\partial T}\right)_\rho d\rho$$

And thus the entropy differential for an isochoric process is:

$$ds = -\frac{1}{\rho^2}\left(\frac{\partial p}{\partial T}\right)_\rho d\rho$$

and for an isothermal process is:

$$ds = \frac{c_v}{T}dT$$

Then the integral Eq. (A.7) becomes:

$$s = s_0 - \int_{\rho_0}^{0} \left[\frac{1}{\rho^2} \left(\frac{\partial p}{\partial T} \right)_\rho \right]_{T_0} d\rho + \int_{T_0}^{T} \left[\frac{c_v}{T} \right]_{\rho=0} dT - \int_0^\rho \left[\frac{1}{\rho^2} \left(\frac{\partial p}{\partial T} \right)_\rho \right]_T d\rho$$

Considering that for the perfect gas ($\rho \to 0$) the specific heat at constant volume is a function of the temperature and using Eq. A.5, the above relation becomes:

$$\begin{aligned} s = \; & s_0 - R \ln \left(\frac{T}{T_0} \right) + \int_{T_0}^{T} \frac{c_{p0}(T)}{T} dT - \int_{\rho_0}^{0} \left[\frac{1}{\rho^2} \left(\frac{\partial p}{\partial T} \right)_\rho \right]_{T_0} d\rho + \\ & - \int_0^\rho \left[\frac{1}{\rho^2} \left(\frac{\partial p}{\partial T} \right)_\rho \right]_T d\rho \end{aligned} \tag{A.8}$$

Although this equation is correct, it cannot be directly solved in this form. In fact, with an equation of state of the Benedict-Webb-Rubin-type, the analytical computation of integrals in Eq. A.8 leads to the indeterminate form $\infty - \infty$. Therefore, some additional terms must be introduced to remove the ambiguity:

$$\begin{aligned} s = \; & s_0 - R \ln \left(\frac{T\rho}{T_0 \rho_0} \right) + \int_{T_0}^{T} \frac{c_{p0}(T)}{T} dT + \int_{\rho_0}^{0} \left[\frac{R}{\rho} - \frac{1}{\rho^2} \left(\frac{\partial p}{\partial T} \right)_\rho \right]_{T_0} d\rho + \\ & + \int_0^\rho \left[\frac{R}{\rho} - \frac{1}{\rho^2} \left(\frac{\partial p}{\partial T} \right)_\rho \right]_T d\rho \end{aligned} \tag{A.9}$$

where the term

$$\int_{\rho_0}^{\rho} \frac{R}{\rho} d\rho = \int_{\rho_0}^{0} \frac{R}{\rho} d\rho + \int_0^\rho \frac{R}{\rho} d\rho$$

has been added to the entropy equation.

Using Eq. A.9 entropy can be computed by differentiating the BWR-type equation of state with respect to temperature. Eq. A.9 can be further reduced; in fact the reference state is, as a matter of fact, a perfect gas condition ($T_0 \gg T_c$ and $p_0 \ll p_c$, where subscript c means "critical") for many common fluids, such as N_2, O_2, air, H_2, CH_4, etc. This implies that along the isotherm-T_0 the fluid behaves like a perfect gas ($p = \rho RT$) and then the integral

$$\int_{\rho_0}^{0} \left[\frac{R}{\rho} - \frac{1}{\rho^2} \left(\frac{\partial p}{\partial T} \right)_\rho \right]_{T_0} d\rho$$

is zero.

Finally the entropy can be computed as:

$$s = s_0 - R \ln \left(\frac{\rho R T}{p_0} \right) + \int_{T_0}^{T} \frac{c_{p0}(T)}{T} dT + \int_0^\rho \left[\frac{R}{\rho} - \frac{1}{\rho^2} \left(\frac{\partial p}{\partial T} \right)_\rho \right]_T d\rho$$

where we have considered $p_0 = \rho_0 R T_0$

A.4 Internal energy and enthalpy

As with the entropy in the last section, the specific internal energy changes from a reference state $e_0(\rho_0, T_0)$ are computed by:

$$e(\rho, T) = e_0(\rho_0, T_0) + \int_{\rho_0, T_0}^{0, T_0} de + \int_{0, T_0}^{0, T} de + \int_{0, T}^{\rho, T} de$$

Considering Eq. A.3 in terms of density instead of specific volume, gives

$$de = c_v dT + \left[\frac{p}{\rho^2} - \frac{T}{\rho^2} \left(\frac{\partial p}{\partial T} \right)_\rho \right] d\rho$$

And thus the internal energy differential for an isochoric process is:

$$de = c_v dT$$

and for an isothermal process is:

$$de = \left[\frac{p}{\rho^2} - \frac{T}{\rho^2} \left(\frac{\partial p}{\partial T} \right)_\rho \right] d\rho$$

A treatment paralleling that for entropy gives the following results for internal energy:

$$e = e_0 - R\,(T - T_0) + \int_{T_0}^{T} c_{p0}(T) dT + \int_0^\rho \left[\frac{p}{\rho^2} - \frac{T}{\rho^2} \left(\frac{\partial p}{\partial T} \right)_\rho \right]_T d\rho \quad \text{(A.10)}$$

Replacing the specific enthalpy definition ($h = e + p/\rho$) in the above equation gives:

$$h = h_0 + \frac{p - \rho RT}{\rho} + \int_{T_0}^{T} c_{p0}(T)dT + \int_0^{\rho} \left[\frac{p}{\rho^2} - \frac{T}{\rho^2} \left(\frac{\partial p}{\partial T} \right)_{\rho} \right]_T d\rho$$

As for entropy, the reference state has been considered as a perfect gas condition ($p_0 = \rho_0 R T_0$).

Note that, differently from entropy, the specific internal energy and enthalpy reference state e_0 and h_0 are related to the reference temperature only: $e_0(T_0)$ and $h_0(T_0)$; in fact, since the reference state is a perfect gas state, Eq. A.10 becomes:

$$e = e_0 - R\,(T - T_0) + \int_{T_0}^{T} c_{p0}(T)dT$$

This equation states that the internal energy is a function of temperature only and then: $e_0 = e_0(T_0)$. Similar conclusion can be achieved for the enthalpy.

A.5 Speed of sound

The definition for the speed of sound a is:

$$a^2 = \left(\frac{\partial p}{\partial \rho} \right)_s$$

As for other thermodynamic variables, we want to express the speed of sound as a function of a generic equation of state written in the form: $p = p(\rho, T)$. This goal can be achieved considering the specific enthalpy and entropy as a function of pressure and temperature, and differentiating these relations:

$$\begin{cases} h &= h\,(p, T) \\ dh &= \left(\dfrac{\partial h}{\partial p} \right)_T dp + \left(\dfrac{\partial h}{\partial T} \right)_p dT = \left(\dfrac{\partial h}{\partial p} \right)_T dp + c_p dT \end{cases}$$

$$\begin{cases} s &= s\,(p, T) \\ ds &= \left(\dfrac{\partial s}{\partial p} \right)_T dp + \left(\dfrac{\partial s}{\partial T} \right)_p dT \end{cases}$$

From the first principle of thermodynamics written in terms of enthalpy ($dh = Tds + vdp$), the entropy and internal energy derivatives can be related:

$$\begin{cases} \left(\dfrac{\partial s}{\partial T}\right)_p = \dfrac{c_p}{T} \\ \\ \left(\dfrac{\partial s}{\partial p}\right)_T = \dfrac{1}{T}\left(\dfrac{\partial h}{\partial p}\right)_T - \dfrac{v}{T} \end{cases}$$

A second differentiation of the entropy, considering that the mixed second derivatives are equal, gives:

$$\left(\frac{\partial h}{\partial p}\right)_T = v - T\left(\frac{\partial v}{\partial T}\right)_p$$

and thus:

$$\left(\frac{\partial s}{\partial p}\right)_T = -\left(\frac{\partial v}{\partial T}\right)_p$$

The entropy differentials with respect to pressure and temperature and with respect to volume and temperature (Eq. (A.3)) are:

$$\begin{cases} ds = \dfrac{c_p}{T}dT - \left(\dfrac{\partial v}{\partial T}\right)_p dp \\ \\ ds = \dfrac{c_v}{T}dT + \left(\dfrac{\partial p}{\partial T}\right)_v dv \end{cases} \tag{A.11}$$

Along an isentropic path (and considering density instead of specific volume) the above equation becomes:

$$\begin{cases} \dfrac{c_p}{T} + \dfrac{1}{\rho^2}\left(\dfrac{\partial \rho}{\partial T}\right)_p \left(\dfrac{\partial p}{\partial T}\right)_s = 0 \\ \\ \dfrac{c_v}{T} - \dfrac{1}{\rho^2}\left(\dfrac{\partial p}{\partial T}\right)_\rho \left(\dfrac{\partial \rho}{\partial T}\right)_s = 0 \end{cases}$$

and then:

$$a^2 = \left(\frac{\partial p}{\partial \rho}\right)_s = \left(\frac{\partial p}{\partial T}\right)_s \left(\frac{\partial T}{\partial \rho}\right)_s = -\frac{c_p}{c_v}\left(\frac{\partial p}{\partial T}\right)_\rho \left(\frac{\partial T}{\partial \rho}\right)_p$$

Finally, using Eq. (A.4), the speed of sound becomes:

$$a^2 = \frac{c_p}{c_v}\left(\frac{\partial p}{\partial \rho}\right)_T$$

In the critical point, since $\left(\frac{\partial p}{\partial v}\right)_T = 0$, the speed of sound reaches the limit value of zero.

A.6 Isothermal compressibility

The isothermal compressibility is defined by:

$$\beta = -\frac{1}{v}\left(\frac{\partial v}{\partial p}\right)_T$$

It represents the capability of compressing a fluid at constant temperature. It is a very low coefficient for a liquid, while it increases for low pressure gas (i.e., rarefied gas).

Using the first principle of thermodynamics and considering the internal energy and entropy as a function of pressure and specific volume (Eq. (A.11)), the following expression is given:

$$c_p - c_v = vT\frac{\alpha^2}{\beta}$$

where

$$\alpha = \frac{1}{v}\left(\frac{\partial v}{\partial T}\right)_p$$

is the thermal expansion and represents the tendency of a fluid to increase in volume when heated. Since β is positive for all the substances (no expansion is allowed during a compression), the term $c_p - c_v$ is always positive. This implies that the specific heat at constant pressure is always bigger than the specific heat at constant volume ($c_p \geq c_v$). The limit case ($c_p = c_v$) is reached in two situations: $T \to 0$ and $\alpha = 0$. The latter case occurs when density reaches a maximum value for a given pressure. This is the case of water at the temperature of $4\ ^\circ C$ under room pressure $1\ bar$.

In the critical point, since $\left(\frac{\partial p}{\partial v}\right)_T = 0$, the isothermal compressibility reaches an infinite value (i.e., the speed of sound is zero) and then $c_p - c_v \to \infty$. This means that in the critical point the specific heat at constant pressure is infinite while the specific heat at constant volume is finite.

Appendix B

Hydrogen thermodynamic properties

The hydrogen molecule is composed of two hydrogen atoms. There are two quantum states modifications of hydrogen molecules called ortho-hydrogen and para-hydrogen. The differentiating feature of these two molecules is the relative orientation of the nuclear spin of the individual atoms. The spins may be in the same direction or they may be in opposite directions, because the nuclear spin is a quantized motion and therefore only certain motions are allowed.

The molecules with anti-parallel (opposed) nuclear spin have even quantum numbers, are in the lowest energy state, and are called para-hydrogen. Conversely the molecules with parallel (aligned) nuclear spin have odd quantum numbers, are in a higher energy level, and are called ortho-hydrogen.

The percentage of ortho-para concentrations in the mixture is temperature dependent (see Fig. B.1 from [41]). The term equilibrium hydrogen is, as the name implies, the equilibrium concentration at a given temperature. At low temperatures the thermal equilibrium favors the para modification. At $20.267\ K$ the equilibrium composition is 99.7% para and only 0.3% ortho-hydrogen. Conversely, the equilibrium composition near ambient temperature is 75% ortho and 25% para. This composition is usually designated normal-hydrogen.

The conversion of ortho-hydrogen to para-hydrogen is an exothermic process. The amount of heat given off in the conversion is temperature dependent. The conversion of a non equilibrium ortho-para composition to an equilibrium composition is a very slow process in the absence of a catalyst, a sharp gradient in magnetic field, or external radiation. For example at $80\ K$ the half life of the conversion is greater than a year.

In general the larger differences in the properties of ortho- and para-hydrogen will occur in the derived properties where heat is important. Properties like en-

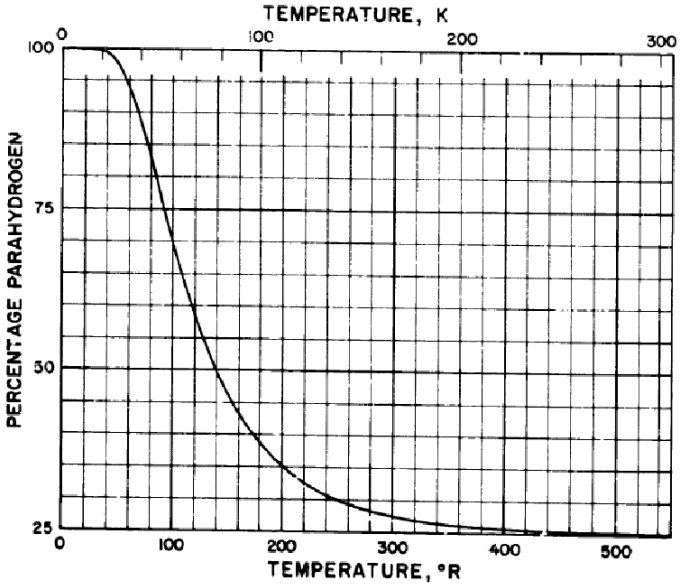

Figure B.1: Hydrogen composition at equilibrium (from [41]).

thalpy, specific heat capacity and thermal conductivity show large differences (see Fig. B.2 and Fig. B.3 from [32])

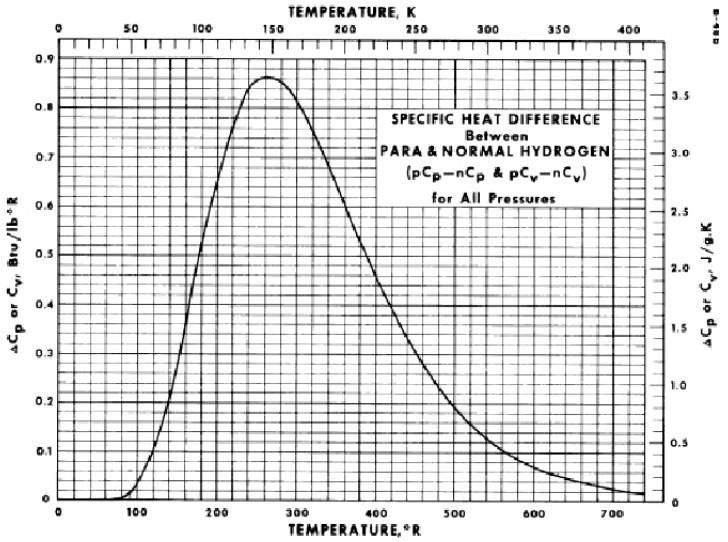

Figure B.2: Specific heat difference between para and normal hydrogen, for all pressures (from [32]).

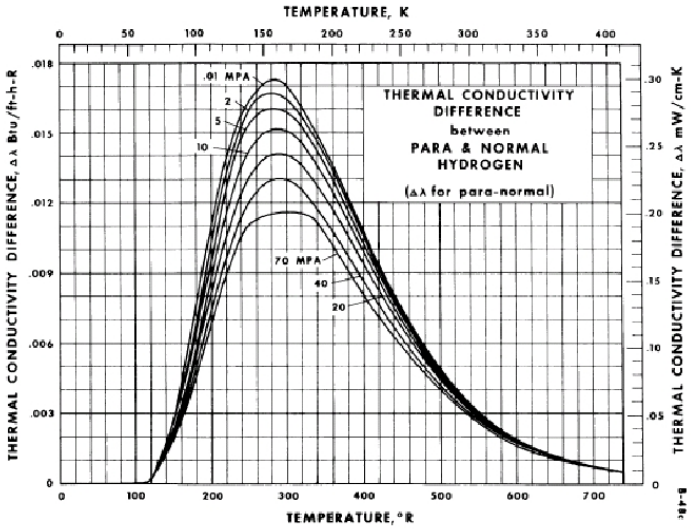

Figure B.3: Thermal conductivity difference between para and normal hydrogen with pressure as parameter (from [32]).

Hydrogen used in rocket propulsion applications is carried as a liquid in the para-modification because of boil-off problems typical of normal- or ortho-hydrogen. Commercially available liquid hydrogen, however, may contain up to 5 or 10 per cent unconverted ortho-hydrogen [18]. For that reason, in case of rocket propulsion applications, the hydrogen thermodynamic properties are generally referred to para-hydrogen. Para-hydrogen thermodynamic equations are taken from [19].

B.1 Para-hydrogen equation of state

A 20-term modified Benedict-Webb-Rubin (MBWR) equation of state is used to represent the pressure-volume-temperature surface of para-hydrogen:

$$p\left(\rho, T\right) = \sum_{i=1}^{6} A_i\left(T\right) \cdot \rho^i + \sum_{j=1}^{2} B_j\left(T\right) \cdot \rho^{2j+1} \cdot e^{-c\rho^2}$$

The terms $A_i(T)$ and $B_j(T)$ are polynomials in T and $1/T$:

$$
\begin{aligned}
A_1(T) &= RT \\
A_2(T) &= n_1 T + n_2 + \frac{n_3}{T} + \frac{n_4}{T^2} + \frac{n_5}{T^3} \\
A_3(T) &= n_6 T + n_7 + \frac{n_8}{T} \\
A_4(T) &= n_9 T + n_{10} \\
A_5(T) &= n_{11} T + n_{12} \\
A_6(T) &= n_{13} \\
B_1(T) &= \frac{n_{14}}{T^2} + \frac{n_{15}}{T^3} + \frac{n_{16}}{T^4} \\
B_2(T) &= \frac{n_{17}}{T^2} + \frac{n_{18}}{T^3} + \frac{n_{19}}{T^4} \\
c &= n_{20}
\end{aligned}
$$

where R is the gas constant: $R = \Re/W$, $\Re$ is the universal perfect gas constant: $\Re = 8.314\ J/K\ mol$ and W is the molecular weight.

If p is in $[MPa]$, T in $[K]$ and ρ in $[g/cm^3]$, the coefficients for para-hydrogen are:

$$
\begin{aligned}
R &= +0.41260486 \cdot 10^{+1} \\
n_1 &= +0.44446150 \cdot 10^{+2} \\
n_2 &= -0.38659604 \cdot 10^{+4} \\
n_3 &= -0.10966550 \cdot 10^{+6} \\
n_4 &= +0.12080022 \cdot 10^{+7} \\
n_5 &= -0.54747655 \cdot 10^{+7} \\
n_6 &= -0.33278647 \cdot 10^{+3} \\
n_7 &= +0.81345734 \cdot 10^{+5} \\
n_8 &= +0.26294257 \cdot 10^{+6} \\
n_9 &= +0.30063983 \cdot 10^{+5} \\
n_{10} &= -0.33024955 \cdot 10^{+7} \\
n_{11} &= -0.24686707 \cdot 10^{+6} \\
n_{12} &= +0.47555234 \cdot 10^{+8} \\
n_{13} &= -0.12064332 \cdot 10^{+9} \\
n_{14} &= -0.49289827 \cdot 10^{+8} \\
n_{15} &= +0.15925894 \cdot 10^{+10}
\end{aligned}
$$

$$\begin{aligned} n_{16} &= -0.87182365 \cdot 10^{+10} \\ n_{17} &= +0.66330266 \cdot 10^{+11} \\ n_{18} &= +0.16366622 \cdot 10^{+11} \\ n_{19} &= -0.12954419 \cdot 10^{+14} \\ n_{20} &= +0.10500000 \cdot 10^{+4} \end{aligned}$$

The reference temperature, pressure, enthalpy and entropy are, for para-hydrogen: $T_0 = 20.268\ K$, $p_0 = 1\ MPa$, $h_0 = 209.9406\ J/g$ and $s_0 = 21.17642\ J/g\ K$.

The para-hydrogen rarefied-gas specific heat at constant pressure is:

$$c_p^0 = \sum_{i=0}^{4} m_i \cdot T^i$$

where (if $c_p^0 = [J/g\ K]$):

$$\begin{aligned} m_0 &= +0.1031200 \cdot 10^{+2} \\ m_1 &= 0 \\ m_2 &= 0 \\ m_3 &= 0 \\ m_4 &= 0 \end{aligned}$$

for $T \leq 40\ K$;

$$\begin{aligned} m_0 &= +0.14759936 \cdot 10^{+2} \\ m_1 &= -0.2197388 \\ m_2 &= +0.32100769 \cdot 10^{-2} \\ m_3 &= -0.12061502 \cdot 10^{-4} \\ m_4 &= +0.57121808 \cdot 10^{-8} \end{aligned}$$

for $40\ K < T \leq 150\ K$;

$$\begin{aligned} m_0 &= +0.66557899 \cdot 10^{+1} \\ m_1 &= +0.15621077 \\ m_2 &= -0.86913643 \cdot 10^{-3} \\ m_3 &= +0.18972274 \cdot 10^{-5} \\ m_4 &= -0.14418461 \cdot 10^{-8} \end{aligned}$$

for $150\ K < T \leq 500\ K$ and

$$\begin{aligned} m_0 &= +0.14411486 \cdot 10^{+2} \\ m_1 &= -0.71767870 \cdot 10^{-3} \\ m_2 &= +0.18638538 \cdot 10^{-5} \\ m_3 &= -0.53065470 \cdot 10^{-9} \\ m_4 &= +0.46649305 \cdot 10^{-13} \end{aligned}$$

for $T > 500\ K$.

The critical parameters for para-hydrogen are:

$$\begin{aligned} T_c &= 32.976K \\ p_c &= 1.2925Mpa \\ \rho_c &= 0.03143\tfrac{g}{cm^3} \end{aligned}$$

B.2 Para-hydrogen transport properties

For para-hydrogen rarefied-gas viscosity μ^* in $[g/cm\ s]$, a two-part fit is used, having temperature T in $[K]$:

$$\mu^* = 8.5558 \left(\frac{T^{3/2}}{T + 19.55}\right) \left(\frac{T + 650.39}{T + 1175.9}\right)$$

for $T \leq 100\ K$ and

$$\mu^* = 1.779\ T^{0.6835}$$

for $T > 100\ K$.

The viscosity is then:

$$\mu = \left[\mu^* + A\ e^{B/T}\right] \cdot 10^{-6}$$

where $A\ e^{B/T}$ is the viscosity excess for low temperatures:

$$\begin{aligned} A(\rho) &= 10^{\left(5.7694 + \ln\rho + 65\ \rho^{3/2} - 6 \cdot 10^{-4}\ e^{127.2\rho}\right)} \\ B(\rho) &= 10 + 7.2 \left[\left(\frac{\rho}{0.07}\right)^6 - \left(\frac{\rho}{0.07}\right)^{3/2} - 17.63\ e^{R(\rho)}\right] \\ R(\rho) &= \begin{cases} -58.75 \left(\frac{\rho}{0.07}\right)^3 & \text{if} \quad \rho \leq 0.0776\ \frac{g}{cm^3} \\ -80 & \text{if} \quad \rho > 0.0776\ \frac{g}{cm^3} \end{cases} \end{aligned}$$

At elevated temperatures (rarefied-gas behaviour): $\mu \to \mu^*$.

The excess function $k - k^*$ for para-hydrogen is nearly function of density alone:

$$k - k^* = \begin{cases} \rho_R \cdot 10^{-7} & \text{if} \quad \rho_R \leq 0.1 \\ \dfrac{10^P}{A} & \text{if} \quad \rho_R > 0.1 \end{cases} \tag{B.1}$$

where $A = 0.003782125$ if $k = [W/cm\ K]$ and ρ_R is the reduced density $\rho_R = \rho/\rho_c$. The function P is a polynomial in ρ_R:

$$P(\rho_R) = c_0 + c_1 x + c_2 x^2 + c_3 x^3 + c_4 x^4$$

where $x = \log_{10} \rho_R$ and:

$$\begin{aligned} c_0 &= -6.82428539 \\ c_1 &= +1.26994786 \\ c_2 &= +1.88960889 \\ c_3 &= +4.30610645 \\ c_4 &= +2.70581484 \end{aligned}$$

The rarefied-gas thermal conductivity k^* for para-hydrogen can be represented as:

$$k^* = \begin{cases} k_A & \text{if} \quad T < 150K \\ x\, k_B + (1-x)\, k_A & \text{if} \quad 150K \leq T \leq 250K \\ k_B & \text{if} \quad T > 250K \end{cases}$$

where $x = 0.01(T - 150)$ and:

$$\begin{aligned} k_A &= 10^{-4}\, k_{roder} \cdot \exp\left[C_1 B \rho + \left(C_2 + \frac{C_3}{T-9}\right)\rho^2\right] \\ k_B &= 4.184\,(k - k^*) + 3.3383 \cdot 10^{-5}\, T^{0.72872} \end{aligned}$$

where:

$$\begin{aligned} C_1 &= 0.988531118 \\ C_2 &= 32.088694 \\ C_3 &= -910.140989 \\ B &= = 39.6 - 2\sqrt{248 - \left(\frac{T}{10} - 17\right)^2} \end{aligned}$$

and k_{roder} is a linear interpolation of tabulated values, by Roder [19], dependent on T alone:

$$
\begin{aligned}
k_{roder}\,(13.000\ K) &= 1.193034427 \\
k_{roder}\,(17.020\ K) &= 1.377540965 \\
k_{roder}\,(19.587\ K) &= 1.509985427 \\
k_{roder}\,(25.100\ K) &= 1.950137728 \\
k_{roder}\,(30.010\ K) &= 2.337542117 \\
k_{roder}\,(33.063\ K) &= 2.550526989 \\
k_{roder}\,(40.145\ K) &= 3.050483187 \\
k_{roder}\,(59.187\ K) &= 4.384607008 \\
k_{roder}\,(79.845\ K) &= 5.986458489 \\
k_{roder}\,(99.852\ K) &= 7.970123593 \\
k_{roder}\,(122.909\ K) &= 10.33669308 \\
k_{roder}\,(153.000\ K) &= 12.74322809
\end{aligned}
$$

To evaluate anomalous thermal conductivity for para-hydrogen the parameter β must be introduced:

$$\beta = \frac{|1 - T_R|^{0.35}}{|1 - \rho_R|}$$

where $T_R = T/T_c$.

Within the region $0.4 \leq \rho_R \leq 1.6$ the anomalous thermal conductivity, which must be added to the thermal conductivity expressed by Eq.(B.1), can be computed by using the following formulas:

$$
k_{anom} = \begin{cases}
\dfrac{3.05 \cdot 10^{-5}\sqrt{\rho_R}}{|1 - \rho_R|^{1.71}} & \text{if} \quad \beta < 0.4 \\
\left[1 + \dfrac{0.9}{\beta^{1/0.35}}\right]^{0.6} \dfrac{3.05 \cdot 10^{-5}}{|1 - T_R|^{0.6}\sqrt{\rho_R}} & \text{if} \quad 0.4 \leq \beta \leq 3 \\
\dfrac{3.05 \cdot 10^{-5}}{|1 - T_R|^{0.6}\sqrt{\rho_R}} & \text{if} \quad \beta > 3
\end{cases}
$$

Outside this region, $k_{anom} = 0$

Appendix C

Methane thermodynamic properties

C.1 Methane equation of state

A 32-term modified Benedict-Webb-Rubin (MBWR) equation of state is used to represent the pressure-volume-temperature surface of methane:

$$p(\rho,T)=\sum_{i=1}^{9}A_i(T)\cdot\rho^i+\sum_{j=1}^{6}B_j(T)\cdot\rho^{2j+1}\cdot e^{-\gamma\rho^2}$$

The terms $A_i(T)$ and $B_j(T)$ are polynomials in T, $1/T$, and $\sqrt{T}$ and γ is a constant related to the fluid critical density ρ_c:

$$\begin{aligned}
A_1(T) &= \Re T \\
A_2(T) &= n_1T+n_2\sqrt{T}+n_3+\frac{n_4}{T}+\frac{n_5}{T^2} \\
A_3(T) &= n_6T+n_7+\frac{n_8}{T}+\frac{n_9}{T^2} \\
A_4(T) &= n_{10}T+n_{11}+\frac{n_{12}}{T} \\
A_5(T) &= n_{13} \\
A_6(T) &= \frac{n_{14}}{T}+\frac{n_{15}}{T^2} \\
A_7(T) &= \frac{n_{16}}{T}
\end{aligned}$$

$$
\begin{aligned}
A_8(T) &= \frac{n_{17}}{T} + \frac{n_{18}}{T^2} \\
A_9(T) &= \frac{n_{19}}{T^2} \\
B_1(T) &= \frac{n_{20}}{T^2} + \frac{n_{21}}{T^3} \\
B_2(T) &= \frac{n_{22}}{T^2} + \frac{n_{23}}{T^4} \\
B_3(T) &= \frac{n_{24}}{T^2} + \frac{n_{25}}{T^3} \\
B_4(T) &= \frac{n_{26}}{T^2} + \frac{n_{27}}{T^4} \\
B_5(T) &= \frac{n_{28}}{T^2} + \frac{n_{29}}{T^3} \\
B_6(T) &= \frac{n_{30}}{T^2} + \frac{n_{31}}{T^3} + \frac{n_{32}}{T^4} \\
\gamma &= \frac{1}{\rho_c^2}
\end{aligned}
$$

where $\Re$ is the universal perfect gas constant: $\Re = 0.831434\,10^{-2}\ kJ/K\ mol$. If p is in $[MPa]$, T in $[K]$ and ρ in $[mol/l]$, the coefficients for methane are:

$$
\begin{aligned}
n_1 &= +0.9898937956 \cdot 10^{-5} \\
n_2 &= +0.2199608275 \cdot 10^{-1} \\
n_3 &= -0.5322788000 \\
n_4 &= +0.2021657962 \cdot 10^{+2} \\
n_5 &= -0.2234398926 \cdot 10^{+4} \\
n_6 &= +0.1067940280 \cdot 10^{-4} \\
n_7 &= +0.1457922469 \cdot 10^{-3} \\
n_8 &= -0.9265816666 \\
n_9 &= +0.2915364732 \cdot 10^{+3} \\
n_{10} &= +0.2313546209 \cdot 10^{-6} \\
n_{11} &= +0.1387214274 \cdot 10^{-3} \\
n_{12} &= +0.4780467451 \cdot 10^{-2} \\
n_{13} &= +0.1176103833 \cdot 10^{-4} \\
n_{14} &= -0.1982096730 \cdot 10^{-3} \\
n_{15} &= -0.2512887756 \cdot 10^{-1} \\
n_{16} &= +0.9748899826 \cdot 10^{-5}
\end{aligned}
$$

$$
\begin{aligned}
n_{17} &= -0.1202192137 \cdot 10^{-6} \\
n_{18} &= +0.4128353939 \cdot 10^{-4} \\
n_{19} &= -0.7215842918 \cdot 10^{-6} \\
n_{20} &= +0.5081738255 \cdot 10^{+3} \\
n_{21} &= -0.9198903192 \cdot 10^{+5} \\
n_{22} &= -0.2732264677 \cdot 10^{+1} \\
n_{23} &= +0.7499024351 \cdot 10^{+5} \\
n_{24} &= +0.1114060908 \cdot 10^{-2} \\
n_{25} &= +0.1083955159 \cdot 10^{+1} \\
n_{26} &= -0.4490960312 \cdot 10^{-4} \\
n_{27} &= -0.1380337847 \cdot 10^{+1} \\
n_{28} &= -0.2371902232 \cdot 10^{-7} \\
n_{29} &= +0.3761652197 \cdot 10^{-4} \\
n_{30} &= -0.2375166954 \cdot 10^{-9} \\
n_{31} &= -0.1237640790 \cdot 10^{-7} \\
n_{32} &= +0.6766926453 \cdot 10^{-6}
\end{aligned}
$$

The reference temperature, pressure, enthalpy and entropy are, for methane: $T_0 = 298.15\ K, p_0 = 0.101325\ MPa, h_0 = 10018\ J/mol$ and $s_0 = 186.266\ J/K\ mol$.

The methane rarefied-gas specific heat at constant pressure is:

$$
\frac{c_p^0}{\Re} = \sum_{i=1}^{7} m_i\ T^{i-4} + m_8\ \frac{m_9^2\ \mathrm{e}^{m_9/T}}{T^2\ \left(\mathrm{e}^{m_9/T} - 1\right)^2}
$$

where, if $c_p^0 = [J/K\ mol]$:

$$
\begin{aligned}
m_1 &= -1.8044750507 \cdot 10^{+6} \\
m_2 &= +7.7426666393 \cdot 10^{+4} \\
m_3 &= -1.3241658754 \cdot 10^{+3} \\
m_4 &= +1.5438149595 \cdot 10^{+1} \\
m_5 &= -5.1479005257 \cdot 10^{-2} \\
m_6 &= +1.0809172196 \cdot 10^{-4} \\
m_7 &= -6.5501783437 \cdot 10^{-8} \\
m_8 &= -6.7490056171 \\
m_9 &= +3.0000000000 \cdot 10^{+3}
\end{aligned}
$$

The critical parameters for methane are:

$$
\begin{aligned}
T_c &= 190.53K \\
p_c &= 4.59797Mpa \\
\rho_c &= 10.150\frac{mol}{l}
\end{aligned}
$$

C.2 Methane transport properties

The functional form for the viscosity is:

$$\mu(\rho, T) = \mu_0(T) + \mu_1(T)\rho + \mu_2(\rho, T) \tag{C.1}$$

The first term of the expansion is the rarefied-gas term which is, according to the molecular theory of gases:

$$\mu_0(T) = \frac{5}{16}\,\frac{1}{\sigma^2\Omega}\,\sqrt{\frac{W\kappa T}{1000\pi N_a}}$$

where μ_0 is measured in $[Pa\ s]$, $W = 16.043\ g/mol$ is the methane molecular weight, $\kappa = 1.38054{\cdot}10^{-23}\ J/K$ is the Boltzmann's constant, T is the temperature in $[K]$, $N_a = 6.0221415{\cdot}10^{23}\ 1/mol$ is the Avogadro's number, $\sigma = 3.68{\cdot}10^{-10}\ m$ is the methane collision diameter and Ω is the dimensionless collision integral. Its value can be computed by:

$$\Omega(T_*) = \frac{1}{\sum_{i=1}^{9} c_i\ {T_*}^{(4-n)/3}}$$

where $T_* = T/T_{min}$ is the dimensionless temperature, and T_{min} is the temperature at which the molecule potential energy function reaches a minimum. In case of methane $T_{min} = 168.1\ K$ and the coefficients c_i are:

$$\begin{aligned}
c_1 &= -3.0328138281 \\
c_2 &= +16.918880086 \\
c_3 &= -37.189364917 \\
c_4 &= +41.288861858 \\
c_5 &= -24.615921140 \\
c_6 &= +8.9488430960 \\
c_7 &= -1.8739245042 \\
c_8 &= +0.2096610140 \\
c_9 &= -0.0096570440
\end{aligned}$$

The second term of Eq. (C.1) represents the contribution of the moderately dense fluid, that is:

$$\mu_1(T) = f_1 + f_2\left[f_3 - \ln\left(\frac{T}{f_4}\right)\right]^2$$

where the coefficients f_i are:

$$\begin{aligned} f_1 &= +0.16969859271 \\ f_2 &= -0.13337234608 \cdot 10^{-1} \\ f_3 &= +0.14000000000 \cdot 10^{+1} \\ f_4 &= +0.16800000000 \cdot 10^{+3} \end{aligned}$$

The third term of Eq. (C.1) represents the contribution of the dense fluid, that is:

$$\mu_2(\rho, T) = \mathrm{e}^{F(\rho,T)} - \mathrm{e}^{G(T)}$$

where:

$$\begin{cases} F(\rho,T) &= G(T) + \left(e_3 + e_4 T^{-3/2}\right) \rho^{0.1} + H(\rho) \sum_{i=5}^{i=7} e_i T^{-i+5} \\ G(T) &= e_1 + \dfrac{e_2}{T} \\ H(\rho) &= \sqrt{\rho}\, \dfrac{\rho - \rho_c}{\rho_c} \end{cases}$$

The coefficients e_i are:

$$\begin{aligned} e_1 &= -0.1620427429 \cdot 10^{+2} \\ e_2 &= +0.4270589027 \cdot 10^{+3} \\ e_3 &= +0.1402596278 \cdot 10^{+2} \\ e_4 &= -0.3916837745 \cdot 10^{+4} \\ e_5 &= -0.3477099090 \cdot 10^{-1} \\ e_6 &= +0.2136542674 \cdot 10^{+2} \\ e_7 &= +0.1436802482 \cdot 10^{+4} \end{aligned}$$

The functional form of the thermal conductivity is:

$$k(\rho, T) = k_0(T) + k_1(\rho, T) + \Delta k_c \tag{C.2}$$

where the rarefied-gas thermal conductivity, according to the molecular theory of gases, is given by:

$$k_0(T) = \frac{\mu_0}{W}\left[\left(c_p^0 - \frac{5}{2}\Re\right)\left(g_1 + \frac{g_2}{T_*}\right) + \frac{15}{4}\Re\right]$$

where k_0 is measured in $[W/m\ K]$, μ_0 in $[\mu Pa\ s]$ and the rarefied-gas specific heat c_p^0 and the universal gas constant are measured in $kJ/K\ mol$. The coefficients g_i are:

$$\begin{aligned} g_1 &= +0.1346953698 \cdot 10^{+1} \\ g_2 &= -0.3254677753 \end{aligned}$$

The second term of Eq. (C.2) represents the contribution of the dense fluid, that is:

$$k_1(\rho, T) = \frac{(F_0(T) + F_1(T)\rho)\,\rho}{1 + F_2(T)\rho}$$

where:

$$\begin{cases} F_0(T) &= \displaystyle\sum_{i=1}^{3} d_i\, T^{1-n} \\ F_1(T) &= \displaystyle\sum_{i=4}^{6} d_i\, T^{4-n} \\ F_2(T) &= \displaystyle\sum_{i=7}^{8} d_i\, T^{7-n} \end{cases}$$

The coefficients d_i are:

$$\begin{aligned} d_1 &= +0.2325800819 \cdot 10^{-2} \\ d_2 &= -0.2477927999 \\ d_3 &= +0.3880593713 \cdot 10^{+2} \\ d_4 &= -0.1579519146 \cdot 10^{-6} \\ d_5 &= +0.3717991328 \cdot 10^{-2} \\ d_6 &= -0.9616989434 \\ d_7 &= -0.3017352774 \cdot 10^{-1} \\ d_8 &= +0.4298153386 \end{aligned}$$

The third term of Eq. (C.2) represents the critical enhancement contribution to the thermal conductivity, and it can be modeled as:

$$\Delta k_c = \frac{h_1}{h_2 + |\Delta T_c|}\, \mathrm{e}^{-(h_3 \Delta\rho_c)^2}$$

where $\Delta T_c = \dfrac{T}{T_c} - 1$, $\Delta\rho_c = \dfrac{\rho}{\rho_c} - 1$ and the coefficients h_i are:

$$\begin{aligned} h_1 &= +6.626 \cdot 10^{-4} \\ h_2 &= +2.295 \cdot 10^{-3} \\ h_3 &= +5.075 \end{aligned}$$

Bibliography

[1] http://www.snecma.com/.

[2] http://webbook.nist.gov/chemistry/fluid/.

[3] http://www.grc.nasa.gov/WWW/CEAWeb/.

[4] B. S. Baldwin and H. Lomax. Thin layer approximation and algebraic model for separated turbulent flows. AIAA Paper 78-257, 1978.

[5] D. R. Bartz. An approximate solution of compressible turbulent boundary-layer development and convective heat transfer in convergent-divergent nozzles. (77 (8)):1235–1245, 1955.

[6] D. R. Bartz. A simple equation for rapid estimation of rocket nozzle convective heat transfer coefficients. *Jet Propulsion*, 27(1):49–51, 1957.

[7] D. R. Bartz. Heat transfer from rapidly accelerating flow of rocket combustion cases and from heated air. In J. P. Hartnett and J. T. F. Irvine, editors, *Advances in Heat Transfer*, volume 2. New York: Academic Pres, 1965.

[8] M. Benedict, G. B. Webb, and L. C. Rubin. An empirical equation for thermodynamic properties of light hydrocarbons and their mixtures. *Journal of Chemical Physics*, 8(4):334–345, 1940.

[9] M. S. Bhatti and R. K. Shah. Turbulent and transition flow convective heat transfer in ducts. In *Handbook of Single-Phase Convective Heat Transfer*. Wiley, New York, 1987.

[10] J. A. Carlile and R. J. Quentmeyer. An experimental investigation of high-aspect-ratio cooling passages. AIAA Paper 92-3154, 1992.

[11] C. F. Colebrook. Turbulent flow in pipes with particular reference to the transition region between the smooth and rough pipe flow. *J. Inst. Civ. Eng.*, (11):133–156, 1938.

[12] F. W. Dittus and L. K. M. Boelter. Heat transfer in automobile radiatord of the tubular type. *Publications in Engineering*, 2:443–461, 1930.

[13] E. R. G. Eckert and R. M. Drake. *Analysis of Heat and Mass Transfer*. McGraw-Hill Book Company, 1972.

[14] A. Frohlich, M. Popp, G. Schmidt, and D. Thelemann. Heat transfer characteristic of h2/o2 - combustion chambers. (1993-1826), 1993.

[15] T. Gallouet, J. Herard, and N. Seguin. Some recent finite volume schemes to compute euler equations using real gas eos. (00:1-6), 2000.

[16] M. Geron. *Simulazioni Numeriche e Fenomenologie di Flussi Tridimensionali in un Aerospike Lineare*. PhD thesis, Department of Mechanics and Aeronautics, 2005.

[17] S. K. Godunov. A difference scheme for numerical solution of discontinuos solution of hydrodynamic equations. (47):271–306, 1959. translated US Joint Publ. Res. Service, JPRS 7226, 1969.

[18] D. P. HarryIII. Formulation and digital coding of approximate hydrogen properties for application to heat-transfer and fluid-flow computations. Technical Report NASA TN D-1664, 1963.

[19] R. C. Hendricks, A. K. Peller, and I. C. Peller. Gasp - a computer code for calculating the thermodynamic and transport properties for ten fluids: Parahydrogen, helium, neon, methane, nitrogen, carbon monoxide, oxygen, fluorine, argon, and carcon dioxide. Technical Report NASA TN D-7808, 1975.

[20] H. L. Hess and H. R. Kunz. A study of forced convection heat transfer to supercritical hydrogen. Journal of Heat Transfer 87, 1965. Trans. ASME.

[21] D. K. Huzel and D. H. Huang. *Modern Engineering for Design of Liquid-Propellant Rocket Engines*. AIAA, United States, 1992.

[22] N. Ierardo, F. Cuoco, and A. Accettura. Lox-methane systems for high thrust lre. Dec. 2002. 4th International Conference on Launcher Technology "Space Launcher Liquid Propulsion".

[23] F. P. Incropera and D. P. DeWitt. *Fundamentals of Heat and Mass Transfer*. John Wiley and Sons, 2002.

[24] K. J. Kacynski. Thermal stratification potential in rocket engine coolant channels. May 1992.

[25] O. Knab, A. Frohlich, D. Wennerberg, and W. Haslinger. Advanced cooling circuit layout for the vinci expander cycle thrust chamber. AIAA Paper 2002-4005, July 2002. 38th AIAA/ASME/SAE/ASEE Joint Propulsion Conference & Exhibit.

[26] O. E. Lancaster. *Jet Propulsion Engines*. Princeton University Press, New Jersey, 1959.

[27] B. E. Launder and D. B. Spalding. Mathematical models of turbulence. *journal of sound and vibration*, 25(4):651–651, Dec. 1972.

[28] F. LeBail and M. Popp. Numerical analysis of high aspect ratio cooling passage flow and heat transfer. (1993-1829), June 1993. 29th AIAA/ASME/SAE/ASEE Joint Propulsion Conference.

[29] J. H. Lienhard and J. H. Lienhard. *A Heat Transfer Textbook*. Phlogiston Press, 2005.

[30] B. J. McBride and S. Gordon. Computer program for calculation of complex chemical equilibrium compositions and applications, i. analysis. NASA Reference Publication 1311, Oct. 1994.

[31] B. J. McBride and S. Gordon. Computer program for calculation of complex chemical equilibrium compositions and applications, ii. user's manual and program description. NASA Reference Publication 1311, Oct. 1994.

[32] R. D. McCarty. Hydrogen technological survey: Thermophysical properties. Technical Report NASA SP-3089, 1975.

[33] M. Niino, A. Kumakawa, N. Yatsuyanagi, and A. Suzuki. Heat trasfer characteristics of liquid hydrogen as a coolant for the l02/lh2 rocket thrust chamber with the channel wall construction. (1982-1107), June 1982. 18th SAE/ASME Joint Propulsion Conference.

[34] D. K. Parris and D. B. Landrum. Effect of tube geometry on regenerative cooling performance. AIAA Paper 2005-4301, July 2005. 41st AIAA/ASME/SAE/ASEE Joint Propulsion Conference.

[35] B. S. Petukhov. Heat transfer and friction in turbulent pipe flow with variable physical properties. *Advances in Heat Transfer*, 6, 1970.

[36] M. Pizzarelli, F. Nasuti, and M. Onofri. A simplified model for the analysis of thermal stratification in cooling channels. July 2007. 2nd European Conference for Aerospace Sciences.

[37] M. Pizzarelli, F. Nasuti, R. Paciorri, and M. Onofri. A numerical model for supercritical flow in rocket engines applications. (2007-5501), July 2007. 42nd AIAA/ASME/SAE/ASEE Joint Propulsion Conference.

[38] D. Preclik, G. Hagemann, O. Knab, C. Mading, D. Haeseler, O. Haidn, A. Woschnak, and M. DeRosa. Lox/hydrocarbon preparatory thrust chamber technology activities in germany. (2005-4555), July 2005. 41st AIAA/ASME/SAE/ASEE Joint Propulsion Conference & Exhibit.

[39] R. C. Reid, J. M. Prausnitz, and B. E. Poiling. *The Properties of Gases & Liquids*. McGraw-Hill Book Company, Inc., New York, 1987.

[40] P. J. Roache. *Verification and Validation in Computational Sciences and Engineering*. Hermosa Publishers, Albuqurerque, NM, 1998.

[41] H. M. Roder, R. D. McCarty, and W. J. Hall. Computer programs for thermodynamic and transport properties of hydrogen. Technical Report NBS-9288, 1967.

[42] S. I. Sandler. *Chemical and Engineering Thermodynamics*. John Wiley and Sons, New York, 1989.

[43] H. Schlichting. *Boundary Layer Theory*. McGraw-Hill Book Company, Inc., New York, 1955.

[44] R. Schuff, M. Mayer, O. Sindiy, C. Ulrich, and S. Fugger. Integrated modeling and analysis for a lox/methane expander cycle engine: Focusing on regenerative cooling jacket design. (2006-4534), July 2006. 42nd AIAA/ASME/SAE/ASEE Joint Propulsion Conference.

[45] C. W. Shu and S. Osher. Efficient implementation of essentially non-oscillatory shock-capturing schemes. *Journal of Computational Physics*, 77:439–471, 1988.

[46] P. R. Spalart and S. R. Allmaras. A one-equation turbulence model for aerodynamic flow. *La Recherche Aerospatiale*, 1:5–21, 1994.

[47] G. P. Sutton and O. Biblarz. *Rocket Propulsion Elements*. John Wiley & Sons, New York, 2001.

[48] E. F. Toro. *Riemann Solvers and Numerical Methods for Fluid Dynamics*. Springer-Verlag, Berlin, Germany, 1999.

[49] J. C. Wennerberg, W. E. Anderson, P. A. Haberlen, H. Jung, and C. L. Merkle. Supercritical flows in high aspect ratio cooling channels. (2005-4302), July 2005. 41st AIAA/ASME/SAE/ASEE Joint Propulsion Conference.

[50] J. C. Wennerberg, H. Jung, R. Schuff, W. E. Anderson, and C. L. Merkle. Study of simulated fuel flows in high aspect ratio cooling channels. AIAA Paper 2006-4708, July 2006. 42nd AIAA/ASME/SAE/ASEE Joint Propulsion Conference & Exhibit.

[51] D. C. Wilcox. *Turbulence Modeling for CFD*. D C W Industries, Inc., 1993.

[52] D. C. Wilcox and I. E. Alber. A turbulence model for high speed flows. In *Proc. of the 1972 Heat Transf. & Fluid Mech. Inst.* Stanford Univ. Pres, 1972.

[53] A. Woschnak and M. Oschwald. Thermo and fluidmechanical analysis of high aspect ratio cooling channels. (2001-3404), July 2001. 37th AIAA/ASME/SAE/ASEE Joint Propulsion Conference.

[54] J. A. Yagley, J. Feng, and C. L. Merkle. The effect of aspect ratio on the effectiveness of combustor coolant passages. (1993-3153), July 1992. 28th AIAA/ASME/SAE/ASEE Joint Propulsion Conference.

[55] J. A. Yagley, J. Feng, and C. L. Merkle. Cfd analyses of coolant channel flowfields. (1993-1830), June 1993. 29th AIAA/ASME/SAE/ASEE Joint Propulsion Conference.

[56] B. A. Younglove and J. F. Ely. Thermophysical properties of fluids. ii. methane, ethane, propane, isobutane, and normal butane. *journal of Physical and Chemical Reference Data*, 16(4), June 1987.

[57] M. J. Zucrow. *Principles of Jet Propulsion and Gas Turbines*. John Wiley & Sons, New York, 1948.